Land-ocean contrasts under climate change

by

Michael P. Byrne

B.A., University of Dublin, Trinity College (2008)
M.Sc., University of Oxford (2009)

Submitted to the Department of Earth, Atmospheric and Planetary Sciences
in partial fulfillment of the requirements for the degree of

Doctor of Philosophy in Climate Physics and Chemistry

at the

MASSACHUSETTS INSTITUTE OF TECHNOLOGY

February 2015

© Massachusetts Institute of Technology 2015. All rights reserved.

Author . . . .
Department of Earth, Atmospheric and Planetary Sciences
September 30, 2014

Certified by . . . .
Paul A. O'Gorman
Associate Professor of Atmospheric Science
Thesis Supervisor

Accepted by . . . .
Robert van der Hilst
Schlumberger Professor of Earth and Planetary Sciences
Head of Department of Earth, Atmospheric, and Planetary Sciences

Land-ocean contrasts under climate change

by

Michael P. Byrne

Submitted to the Department of Earth, Atmospheric and Planetary Sciences
on September 30, 2014, in partial fulfillment of the
requirements for the degree of
Doctor of Philosophy in Climate Physics and Chemistry

Abstract

Observations and climate models show a pronounced land-ocean contrast in the responses of surface temperature and the hydrological cycle to global warming: Land temperatures increase more than ocean temperatures, low-level relative humidity increases over ocean but decreases over land, and the water cycle has a muted response over land in comparison to ocean regions at similar latitudes. A comprehensive physical understanding of these land-ocean contrasts has not been established, despite the robustness of the features and their importance for the regional and societal impacts of climate change.

Here we investigate land-ocean contrasts in temperature, relative humidity, and precipitation minus evaporation ($P - E$) under climate change using both idealized and full-complexity models. As in previous studies, we find enhanced surface warming over land relative to the ocean at almost all latitudes. In the tropics and subtropics, the warming contrast is explained using a convective quasi-equilibrium (CQE) theory which assumes equal changes in equivalent potential temperature over land and ocean. As the CQE theory highlights, the warming contrast depends strongly on changes in relative humidity, particularly over land. The decreases in land relative humidity under warming can be understood using a conceptual model of moisture transport between the land and ocean boundary layers and the free troposphere.

Changes in $P - E$ over ocean are closely tied to the local surface-air temperature changes via a simple thermodynamic scaling; the so-called "rich-get-richer" mechanism. Over land, however, we show that the response has a smaller magnitude and deviates substantially from the thermodynamic scaling. We examine the reasons for this land-ocean contrast in the response of $P - E$ by analyzing the atmospheric moisture budget. Horizontal gradients of surface temperature and relative humidity changes are found to be important over land, with changes in atmospheric circulation playing a secondary role outside the tropics. An extended thermodynamic scaling is introduced and is shown to capture the multimodel-mean response of $P - E$ over land, and the physical mechanisms behind the extended scaling are discussed.

Thesis Supervisor: Paul A. O'Gorman

Title: Associate Professor of Atmospheric Science

Acknowledgments

Had my advisor, Paul O'Gorman, not taken a punt on me back in early 2009, I never would have come to MIT and this thesis would not have happened. I would like to sincerely thank Paul for all his advice and good humo(u)r over the last five years. He has an endless supply of ideas and has taught me a huge amount about both climate science and the scientific process. I will miss the weekly meetings and our occasional lapses into nostalgic chats about Trinity and Ireland.

I would like to thank Bill Boos, Kerry Emanuel, and Alan Plumb for serving on my thesis committee. The opportunity to discuss my work over the last couple of years with such eminent and thoughtful scientists has been invaluable. Brian Rose, Yohai Kaspi, Isaac Held, and Bjorn Stevens offered technical and conceptual advice at different times for which I am also grateful.

In their never-ending pursuit of knowledge, scientists need support and I would like to thank Kristen Barilaro, Jen Sell, Carol Sprague, Jacqui Taylor, and Linda Meinke for their administrative assistance and kindness over the years.

Pursuing a PhD at EAPS/PAOC has been special and, of course, my fellow students have enhanced the experience hugely. Colleagues became mates very quickly. In particular, thanks to Alli Wing, Marty Singh, Tim Cronin, Dan Chavas, Neil Zimmerman, Mike Sori, Malte Jansen, Morgan O'Neill, Seb Marcq, Andy Miller, Anita Ganesan, Diane Ivy, Dave Forney, and Chris Follett for the camaraderie and the banter. Now I've got friends in scattered places.

For keeping me fit and entertained during my studies, I would like to thank John Gaffney, Frank O'Sullivan, and the other fine gentlemen of the MIT Rugby Football Club. *Mens sana in corpore sano.*

A special thanks to my girlfriend, Gemma, who has put up with having a grad student as a boyfriend for long enough! Having you here for the last two years has made me a very happy man. Looking forward to our adventures in Peru, Bolivia, Zürich, and wherever life takes us.

My journey to MIT started a long time ago and I was encouraged at every juncture by my parents, Patricia and Mick, and my brother Breon. Their strong work ethic and deep belief in education inspire me daily, and the prospect of brotherly competition on the Christmas Day run keeps me in shape! Without their wit (Dad!), calm advice, and sense of perspective, I would not have gotten to this point. Gemma and I are very much looking forward to having you in Cambridge for the thesis defense and to moving closer to home in a few short months.

Many thanks to my diligent team of thesis proof-readers, you know who you are!

Finally to matters financial. My thesis work was largely supported by the federal, industrial, and foundation sponsors of the MIT Joint Program on the Science and Policy of Global Change and by National Science Foundation grant AGS-1148594. I have also been supported by a Presidential Fellowship and by a Thomas Frank Science Fellowship at various points during my studies at MIT. The Houghton Fund has provided generous support for academic travel and other research activities. The substantial assistance from all of these bodies is much appreciated.

Contents

1 Introduction **27**

2 Warming contrast: Idealized GCM **31**

2.1 Introduction 31

2.2 Theory 35

2.3 Idealized GCM 41

2.3.1 Land configurations 41

2.3.2 Model and simulations 41

2.3.3 Zonal-mean climatology (subtropical zonal land band) 44

2.4 Subtropical warming contrast 46

2.4.1 Subtropical zonal land band 46

2.4.2 Subtropical continent 50

2.4.3 The effect of aridity 51

2.5 Higher-latitude warming contrast 53

2.5.1 Midlatitude zonal land band 53

2.5.2 Midlatitude theory 54

2.5.3 Meridional land band 55

2.5.4 Polar amplification 56

2.6 Land-ocean radiative contrasts 57

2.6.1 Water vapor radiative feedbacks 57

2.6.2 Albedo contrast 59

2.7 Surface air versus surface skin temperature 60

2.8 Conclusions 62

3 Warming contrast: CMIP5 simulations and observations 67

3.1 Introduction 67

3.2 Land-ocean contrasts in CMIP5 simulations 69

3.3 Application of theory 72

3.3.1 Estimate of amplification factor 74

3.3.2 Contributions to the tropical amplification factor 76

3.3.3 Trends in the historical simulations 77

3.3.4 Sensitivity to the diurnal cycle 79

3.3.5 Implications for changes in heat stress 80

3.4 Warming contrast in observations 81

3.5 Conclusions 86

4 Response of land relative humidity to global warming 89

4.1 Introduction 89

4.2 Conceptual model 93

4.2.1 Theory 93

4.2.2 Idealized GCM simulations 95

4.2.3 CMIP5 simulations 97

4.3 Extended model: Influence of evapotranspiration 101

4.3.1 Derivation 102

4.3.2 Application to simulations 103

4.4 Feedback between temperature and relative humidity changes 107

4.5 Conclusions 108

5 The terrestrial water cycle under global warming 111

5.1 Introduction 111

5.1.1 The "rich-get-richer" paradigm 114

5.1.2 Outline of chapter 117

5.2 Data and Methods 118

5.3 Contributions to $\delta(P - E)$: A moisture budget decomposition 120

5.3.1 Ocean components 120

5.3.2 Land components 124

5.4 An extended scaling for $\delta(P-E)$ over land 127

5.4.1 Derivation 127

5.4.2 Application of extended scaling 129

5.4.3 Physical interpretation 131

5.4.4 Specific humidity formulation 137

5.5 Modifications to the extended scaling 140

5.5.1 Column water vapor analysis 140

5.5.2 Diffusive moisture transport by transient eddies 142

5.6 Conclusions 144

6 Concluding remarks **147**

6.1 Summary of key points 147

6.2 Outlook 150

List of Figures

2-1 Schematic diagram of potential temperature vs. height for moist adiabats over land and ocean and equal temperatures at upper levels. A land-ocean surface air temperature contrast is implied by different LCLs over land and ocean. 35

2-2 Theoretical values of (a) the land-ocean surface air temperature difference $T_{\mathrm{L}} - T_{\mathrm{O}}$ (contour interval 5 K) and (b) the amplification factor $A^T = \partial T_{\mathrm{L}}/\partial T_{\mathrm{O}}$ (contour interval 0.1) at constant relative humidities for a range of surface relative humidities over land and temperatures over ocean. Surface relative humidity over ocean is fixed at 80%. The temperature differences and amplification factors are calculated by numerically solving the equal equivalent potential temperature equation (2.1). 37

2-3 Theoretical values for the partial derivatives of land surface air temperature with respect to (a) surface relative humidity over land, $\partial T_{\mathrm{L}}/\partial \mathcal{H}_{\mathrm{L}}$, and (b) surface relative humidity over ocean, $\partial T_{\mathrm{L}}/\partial \mathcal{H}_{\mathrm{O}}$, as a function of land relative humidity and ocean temperature [contour interval 0.2K $\%^{-1}$ in (a) and 0.1K $\%^{-1}$ in (b)]. Surface relative humidity over ocean is fixed at 80%. The partial derivatives are calculated by numerically solving the equal equivalent potential temperature equation (2.1). 38

2-4 Simulations are performed using a variety of land configurations: (a) and (b) indicate zonal bands from 20°N to 40°N and from 45°N to 65°N, respectively, (c) is a continent spanning 20°N to 40°N and 0°E to 120°E, and (d) is a meridional band from 0°E to 60°E. 41

2-5 The zonal and time mean potential temperature (left, contour interval 15 K), Eulerian-mean streamfunction (center, contour interval $20 \times 10^9\,\mathrm{kg\,s^{-1}}$, with negative values given by dashed contours), and relative humidity (right, contour interval 10%) for a zonal land band from 20°N to 40°N in (a) a cold simulation ($\alpha = 0.4$), (b) the reference simulation ($\alpha = 1$), and (c) the warmest simulation ($\alpha = 6$). The heavy black bars indicate the position of the subtropical zonal land band (20°N to 40°N). 43

2-6 Surface air temperature over ocean (solid line with circles) and land (dashed line with circles) vs. ocean surface air temperature for a subtropical zonal land band from 20°N to 40°N. Filled circles denote the reference simulation ($\alpha = 1$) here and in subsequent figures. The dashed-dotted line is the estimate of surface air temperature over land from theory. 46

2-7 The amplification factor vs. ocean surface air temperature in simulations with a subtropical land band from 20°N to 40°N (solid line with circles), from theory (dashed line), and from theory neglecting changes in relative humidity (dashed-dotted line). The amplification factor is calculated based on temperature differences between pairs of nearest-neighbor simulations and is plotted against the mid-point ocean temperature for each pair. The amplification factor from theory is obtained in the same way, but using the theoretical estimates of the land temperature based on mean surface relative humidities (dashed-dotted line in Fig. 2-6). The amplification factor from theory neglecting changes in relative humidities [corresponding to A^T in (3.2)], is evaluated using the mean surface relative humidity from the colder of the pair of simulations when estimating the land temperature in the warmer simulation. 47

2-8 Vertical profiles of potential temperature averaged in time and over land (dashed) and the corresponding ocean region (solid) for cold, reference, and warm simulations ($\alpha = 0.4$, 1, and 2, respectively) with a subtropical zonal land band from 20°N to 40°N. 49

2-9 Vertical profiles of lapse rates averaged in time and over (a) ocean and (b) land for a warm simulation ($\alpha = 2$ and a global-mean surface air temperature of 302 K) with a subtropical zonal land band from 20°N to 40°N. The solid lines show the simulated lapse rates, the dashed lines correspond to moist adiabats calculated using the mean surface air temperatures and mean surface relative humidities, and the dashed-dotted lines correspond to averages of moist adiabats weighted according to the PDFs of surface relative humidity following (2.3). Note that the theory only requires that the lapse rates be moist adiabatic up to the level at which the temperature profiles converge, approximately $\sigma = 0.6$ for this simulation (Fig. 2-8). 50

2-10 Surface air temperature over ocean (solid line with circles) and land (dashed line with circles) vs. ocean surface air temperature for a land continent spanning 20°N to 40°N and 0°E and 120°E. The dashed-dotted line is the estimate of the land temperature from theory. . . . 51

2-11 Surface air temperature over ocean (solid line with circles) and land (dashed line with circles) vs. evaporative fraction β for (a) a subtropical zonal land band from 20°N to 40°N and (b) a midlatitude zonal land band from 45°N to 65°N. The dashed-dotted lines are the estimates of land temperature from theory, and the dotted line is an estimate of the midlatitude land temperature using a midlatitude version of the theory in which the predicted warming contrast is 0.6 times the contrast estimated from the original theory [following O'Gorman (2011)]. The longwave absorber parameter α has its reference value of unity in all simulations. 52

2-12 The amplification factor vs. latitude for warming between two simulations ($\alpha = 1$ and $\alpha = 1.5$) with a meridional land band from 0°E to 60°E (solid line). The dashed line is the estimate of the amplification factor from theory, and the dashed-dotted line is the estimate from theory neglecting changes in relative humidity. Interhemispheric asymmetry is indicative of sampling error. 57

2-13 The amplification factor vs. ocean surface air temperature in land-ocean albedo contrast simulations with a subtropical zonal land band from 20°N to 40°N (solid line), and from theory (dashed line). The ocean albedo is 0.20 and the land albedo has the default value of 0.38. The amplification factors are calculated as in Fig. 2-7. 60

2-14 Surface air temperature over ocean (solid line with circles) and land (dashed line with circles), along with surface skin temperature of the ocean (solid line) and land (dashed line) vs. ocean surface air temperature for simulations with a subtropical zonal land band from 20°N to 40°N. The same spatial and temporal averaging is used for the skin temperatures as for the surface air temperatures. 61

3-1 Multimodel-median changes in surface air (a) temperature, (b) relative humidity, and (c) equivalent potential temperature between the historical (1975-2004) and RCP8.5 (2070-2099) simulations. Panel (d) shows the multimodel-median surface air relative humidity in the historical simulation (1975-2004). Each field is linearly interpolated to a common grid prior to calculation of the multimodel median. Absolute rather than fractional changes in relative humidity are shown in (b). . 68

3-2 The land-ocean amplification factor, $A = \Delta T_{\mathrm{L}}/\Delta T_{\mathrm{O}}$, vs latitude in the multimodel median (solid line), its interquartile range (gray shading), and the corresponding estimate from theory (dashed line). 70

3-3 As in Fig. 3-2 but the gray shading shows different quantities instead of the interquartile range of the models. In (a), the gray shading shows the full model range. In (b), the gray shading shows a measure of the effect of internal variability on the multimodel median at each latitude. The internal variability in the simulated amplification factor is estimated by first dividing the 30-year averaging periods in the historical and RCP8.5 simulations into three decades each, i.e. for the historical simulation the averaging periods are 1975-84, 1985-94, and 1995-2004 (similarly for RCP8.5). The land and ocean temperature changes between the historical and RCP8.5 simulations for every combination of decades (nine combinations in total) are then used to recalculate the amplification factor. The upper bound of the gray shading denotes the multimodel median of the maximum amplification factor obtained from this analysis at each latitude, and the lower bound is the multimodel median of the minimum values. 71

3-4 (a) Simulated tropical amplification factors (A_{sim}) vs their theoretical estimates (A_{theory}) for different climate models. The solid line is the one-to-one line. (b) Boxplots showing the tropical amplification factors, their estimates from theory, and the contributions to these estimates as defined by (3.2). The whiskers show the full model range, the boxes show the 1st and 3rd quartiles, and the central line shows the median. All amplification factors and contributions in this figure have been averaged between 20°S and 20°N. 72

3-5 The multimodel-median difference between surface air equivalent potential temperatures over land and ocean vs latitude for the historical (1975-2004) and RCP8.5 (2070-2099) simulations. The equivalent potential temperatures are evaluated based on zonal- and time-mean temperatures and relative humidities to be consistent with how the theory is evaluated. 73

3-6 As in Fig. 3-4a but averaged over different latitude bands. The tropics (black symbols) are 20°S to 20°N. The subtropics (red symbols) are 20° to 40° in both hemispheres. The mid-latitudes (green symbols) are 40° to 60° in both hemispheres. The high-latitudes (blue symbols) are 60° to 90° in the Northern Hemisphere only because the amplification factors are noisy at these latitudes in the Southern Hemisphere for some of the models. 75

3-7 As in Fig. 3-2 but for trends (1950-2004) in the historical simulations rather than changes under RCP8.5. Here, ΔT_{L} and ΔT_{O} denote land and ocean temperature trends, respectively. 77

3-8 As in Fig. 3-4 but for trends (1950-2004) in the historical simulations rather than for changes under RCP8.5. The red, blue, green, and black dashed lines in (a) denote the amplification factors calculated using land and ocean temperature trends (1950-2004) from the HadCRUT3, MLOST, GISTEMP, and BEST surface temperature datasets, respectively. The observational temperature trends are calculated by first averaging over all available land and ocean data between 20°S and 20°N, with area weighting, and then computing the trends using linear least squares regressions. Due to the sparsity of gridded humidity observations over tropical land, for instance in the HadCRUH dataset (Willett et al., 2008), we do not estimate the amplification factor for observations. 78

3-9 As in Fig. 3-2 but using (a) daily-maximum surface air temperatures and daily-minimum surface relative humidities in the subset of models for which the data were available and (b) daily-mean temperatures and relative humidities for the same subset of models as in (a). The subset of models used in this figure is listed in Section 3.3.4. 79

3-10 Changes in tropical-mean (20°S to 20°N) surface air equivalent potential temperature over land vs ocean (filled circles). The equivalent potential temperatures are calculated using the time-mean temperatures and relative humidites at each grid point prior to averaging over the tropics. The unfilled circles show the same quantities but with land relative humidity held fixed under climate change. The solid line corresponds to equal changes over land and ocean. 80

3-11 Time series (1910-2005) of land and ocean surface temperatures from HadCRUT3 (Brohan et al., 2006) averaged from 40°S to 40°N with area weighting. A 3-year moving average filter has been applied to the data. Due to sparse observational data and the highly variable temperature responses amongst the various climate models at high latitudes, and also because the convective quasi-equilibrium theory for the warming contrast is more valid closer to the equator, we restrict our analysis of the warming contrast in observations to lower latitudes (40°S to 40°N). 81

3-12 Histograms of amplification factors, averaged from 40°S to 40°N, for the historical CMIP5 simulations (a) over 1910-50 and (b) over 1965-2005. Circles denote the observed amplification factors over the same periods in three surface temperature datasets (HadCRUT3, MLOST, GISTEMP, and BEST plotted as red, blue, green, and black circles respectively). The black square is the amplification factor from the NOAA 20th-Century Reanalysis. For (c) and (d), the CMIP5 models and the NOAA 20th-Century Reanalysis have been subsampled to the HadCRUT3 observations at each month. Note that the horizontal axes and the box widths are in log scale. 83

3-13 Time series of the normalized area of data coverage over land and ocean globally, respectively, in the HadCRUT3 surface temperature dataset (with area weighting). We have normalized by the areas of land and ocean covered by the dataset in the last month of the time period (i.e., December, 2005). We note that the land coverage peaked in approximately 1970 and has since been declining, while the ocean coverage has been relatively constant since 1980. 84

3-14 Time series (1910-50) of land and ocean surface temperatures from the NOAA 20th-Century Reanalysis (Compo et al., 2011) averaged from 40°S to 40°N with area weighting (light lines) along with the least-squares trends (heavy lines) (a) without data subsampling and (b) after subsampling to the HadCRUT3 observations. A 3-year moving average filter has been applied to the data. 87

4-1 Multimodel-mean changes in surface-air relative humidity between the historical (1976-2005) and RCP8.5 (2070-2099) simulations, normalized by the global-mean surface-air temperature changes [(a) and (b)]. For (b), the blue and red lines represent zonal averages over ocean and land regions, respectively. All quantities are expressed in units of %/K. 91

4-2 Schematic diagram of the conceptual box model for changes in land humidity, summarized by (4.4). The height of the boundary layer is h, L is a horizontal length scale, q_O and q_L are the ocean and land boundary-layer specific humidities, respectively, and q_{FT} is the free tropospheric specific humidity. Horizontal and vertical mixing velocities are denoted by v_1 and v_2, respectively. 94

4-3 The idealized GCM simulations analyzed in this chapter have a subtropical continent covering 20°N to 40°N and 0°E to 120°E, with a slab ocean elsewhere. 95

4-4 Changes in (a) surface-air land specific humidity and (b) surface-air land relative humidity (normalized by the land surface-air temperature change) between pairs of idealized GCM simulations with a subtropical continent. Solid lines denote the simulated changes and the dashed lines represent the estimated changes using the conceptual model (4.4). 96

4-5 Multimodel-mean changes in zonally-averaged (a) surface-air land specific humidity and (b) surface-air land relative humidity (normalized by the global-mean surface-air temperature change) between the historical and RCP8.5 CMIP5 simulations. Solid lines denote the simulated changes (for the relative humidity changes, the solid line denotes the "pseudo-relative humidity" changes), and dashed lines represent the estimated changes using the conceptual model (4.4). For (b), the dotted line is the simulated relative humidity outputted by the models (named *hurs* in the CMIP5 archive). 99

4-6 Simulated changes in surface-air land pseudo-relative humidity versus the estimates from the conceptual model (4.4) for each of the 19 CMIP5 models analyzed. Both quantities have been averaged over all land from 90°S to 90°N. The blue line is the one-to-one line and the correlation coefficient is $r = 0.66$. 100

4-7 As in Figure 4-2, though now including land evapotranspiration, E_L, from the surface to the surface-air layer. 102

4-8 As in Figure 4-4, but here estimating the surface-air humidity changes using the extended model (4.7). The components of the estimated specific humidity changes due to ocean humidity changes ($\gamma\delta q_O$, blue dashed) and land evapotranspiration changes ($\epsilon\delta E_L$, green dashed) are also shown. 104

4-9 As in Figure 4-5a, but here estimating the multimodel-mean surface-air land specific humidity changes using the extended model (4.7). The components of the estimated specific humidity changes due to ocean humidity changes ($\gamma\delta q_O$, blue dashed) and land evapotranspiration changes ($\epsilon\delta E_L$, green dashed) are also shown. By construction, the simulated and estimated changes are exactly equal (solid red line). Unlike in Figure 4-5b, the changes in land relative humidity are not plotted as there is no straightforward way to partition the changes into ocean humidity and evapotranspiration components. 106

4-10 As in Figure 4-6, but here with simulated changes in surface-air land pseudo-relative humidity versus the estimates from the extended model (4.7). The correlation coefficient is $r = 0.67$. 107

4-11 Schematic diagram describing the feedback between changes in temperature and relative humidity over land and ocean. 108

5-1 [(a) and (b)] Multimodel-mean precipitation minus evaporation ($P-E$) in the historical (1976-2005) simulations, and [(c) and (d)] multimodel-mean changes in $P-E$ between the historical (1976-2005) and RCP8.5 (2070-2099) simulations. For (b) and (d), the blue and red lines represent zonal averages over ocean and land regions, respectively. All quantities are expressed in units of millimeters per day. 112

5-2 Multimodel-mean changes in zonal-mean $P-E$ averaged (a) globally, (b) over oceans, and (c) over land. Solid lines show the simulated changes and dashed lines are the estimates from the Held and Soden scaling (5.1). Here and in subsequent figures, “simulated” means $P-E$ changes calculated using the time-mean atmospheric moisture budget [see Eqn. (5.7)]. 114

5-3 Multimodel-mean simulated changes in zonal-mean $P-E$ averaged (a) over oceans and (b) over land (solid lines), along with $P-E$ changes as estimated from the atmospheric moisture budget [dashed lines, see Eqn. (5.7)]. 116

5-4 Contributions to changes in ocean $P-E$ from (a) the mean thermodynamic component, (b) the mean dynamic component, (c) the transient eddy component, and (d) the nonlinear component [the various terms are defined by Eqn. (5.7)]. Solid lines denote the simulated changes, dashed lines are the estimates from the Held and Soden scaling [Eqns. (5.1) and (5.9)], and the dashed-dotted line is the "slowdown scaling" as defined by (5.8). 121

5-5 As in Figure 5-4, but for the land components. 125

5-6 As in Figure 5-2, but including the estimates of changes in $P-E$ using the extended scaling (5.11) (black solid lines). 126

5-7 Simulated changes in global-mean land $P-E$ (i.e., mean runoff changes) versus the estimates from the Held and Soden scaling (black squares) and from the extended scaling (red circles). The blue line is the one-to-one line. The correlation coefficient for the simulated changes and the Held and Soden scaling is -0.31, and is 0.02 for the simulated changes and the extended scaling. 128

5-8 (a) Multimodel-mean simulated changes in $P-E$ between the historical and RCP8.5 simulations and the changes estimated using (b) the Held and Soden scaling and (c) the extended scaling. Only the changes over land are shown. The units are millimeters per day, and each plot has been smoothed using a low-pass 1-2-1 filter. 131

5-9 As in Figure 5-8, but here showing only the changes over ocean regions. 132

5-10 The various terms in the extended scaling for $P-E$ over land, defined by (5.11). In each case the multimodel mean is plotted. 133

5-11 As in Figure 5-10, but for ocean regions. 134

5-12 The multimodel-mean zonal (red) and meridional (black) components of the (a) temperature and (b) relative humidity gradient terms in the extended scaling (5.11). 135

5-13 Schematic diagrams of the two mechanisms by which changes in horizontal temperature gradients can dry the land. The heavy black arrows represent a climatological zonal atmospheric moisture flux and the curves are idealized profiles of surface-air temperature changes versus longitude. 136

5-14 The contributions to the zonal (a) temperature and (b) relative humidity gradient terms due to east-west asymmetries in surface-air temperature and relative humidity changes, respectively (black), as calculated from (5.12). Red lines show the full zonal temperature and relative humidity gradient terms. 137

5-15 The contributions to the specific humidity formulation of the extended scaling for $P - E$ over land, defined by (5.13). In each case the multimodel mean is plotted. 138

5-16 (a) Multimodel-mean fractional changes in surface-air specific humidity, $\delta q_S/q_S$, between the historical (1976-2005) and RCP8.5 (2070-2099) simulations, and (b) the multimodel-mean zonal (red) and meridional (black) components of the specific humidity gradient term in the scaling (5.13). 139

5-17 Comparison of the multimodel-mean simulated (blue and red solid lines) changes in the [(a) and (c)] mean thermodynamic and [(b) and (d)] transient eddy components of $P - E$ with the extended scaling estimates (blue and red dashed lines) and with estimates from the column water vapor scaling (black solid lines), over [(a) and (c)] ocean and [(b) and (d)] land. The extended and column water vapor scalings are defined by (5.11) and (5.15), respectively. 142

5-18 Multimodel-mean simulated (blue and red solid lines) transient eddy component of $P - E$ changes along with the extended scaling estimates (dashed lines) and the estimates from the diffusive scaling (black solid lines), over (a) ocean and (b) land. The extended and diffusive scalings are defined by (5.11) and (5.18), respectively. 144

List of Tables

3.1 Amplification factors for the CMIP5 models, the NOAA 20th-Century Reanalysis, and three observational datasets, computed for two periods (1910-1950 and 1965-2005) and averaged from 40°S to 40°N with area weighting. Results are displayed for two cases: (i) Where the models and reanalysis are not subsampled, and (ii) where the models and reanalysis are subsampled to the available HadCRUT3 observations at each month. For the models, the multimodel-median value is shown in each case. 85

Chapter 1

Introduction

The Earth's climate is determined by a huge variety of competing processes, including electromagnetic radiation, biogeochemical cycles, ice dynamics, plate tectonics, atmospheric and oceanic heat transport, and many others. Climate-relevant timescales range from minutes (atmospheric convection) to thousands of years (deep ocean mixing) and longer. Spatial scales span more than ten orders of magnitude, from nanometers (absorption and emission of radiation) and micrometers (transpiration through plant stomata) to the planetary scale (stationary atmospheric waves). Due to the vast range of scales involved, experimentally testing hypotheses of how the climate system works using a physical laboratory or Earth observing systems is often infeasible. For this reason, we increasingly turn to computer simulations of varying complexity in order to improve our understanding of the dynamics of climate. However, once again because of the myriad time and space scales involved and partially owing to finite computational resources, simulating the climate and validating the simulations versus observations is also challenging.

One specific question in climate science that has received much attention, from both scientists and computer simulations, is how the climate will respond to increasing greenhouse gases concentrations. Our current understanding of future climate change is summarized in the most recent report from the Intergovernmental Panel on Climate Change (Stocker et al., 2013) and is based largely on complex climate model simulations. However, despite their complexity and the variety of physical, chemical, and biological processes represented, climate models are imperfect simulators of the Earth system. This imperfection results largely from (i) the coarse spatial resolution of climate models, which necessitates the parameterization of important small-scale phenomena such as atmospheric convection, and (ii) from our limited understanding of the physics of various climate processes, including clouds and sea ice dynamics. These modeling difficulties contribute to uncertainty in the climate change response. The uncertainty is manifested by discrepancies between the projections of the various climate models, both on the global scale (e.g., climate sensitivity) and on regional scales (e.g., local precipitation changes) (Stevens and Bony, 2013).

Despite these challenges, there are robust features of the climate change signal upon which all the models qualitatively agree. Such features include polar-amplified warming, enhanced warming in the upper troposphere relative to the surface, and larger surface temperature increases over land than over ocean. These temperature responses were noted in some of the earliest, most primitive general circulation model simulations (e.g., Manabe et al., 1991) and persist to this day in the most sophisticated models. The robustness of these signals suggests that fundamental mechanisms are involved. Indeed polar amplification and enhanced upper tropospheric warming have been investigated extensively and can be understood, at least to first-order, in terms of basic physical principles (Holland and Bitz, 2003; Santer et al., 2005).

The land-ocean warming contrast, however, has been studied comparatively little, despite its societal importance (most of us live on land!). It has long been recognized that the warming contrast is not primarily a thermal inertia effect (ocean has a much larger effective heat capacity than land) but rather is related to land aridity. However, a quantitative theory to explain the magnitude of the land-ocean warming contrast has yet to emerge, highlighting a lack of understanding of this seemingly simple response to global warming.

One of the key tasks for climate science is to improve regional-scale climate change projections. An essential step towards this goal is to understand the robust, large-scale features of climate change simulations, such as the land-ocean warming contrast. The purpose of this thesis is to derive and test quantitative theories for not only the warming contrast, but also for changes in land relative humidity, which we will show to be closely linked to the warming contrast, and for changes in the terrestrial water cycle. All climate models project relative humidity increases over ocean and decreases over land as the climate warms, yet the expected land decreases are poorly understood, as is the response of the terrestrial water cycle to climate change (the ocean response, in contrast, is well-captured by a simple thermodynamic scaling). As we will demonstrate, this water cycle response over land is strongly influenced by the land-ocean warming contrast and by relative humidity changes.

Quantifying land-ocean contrasts under climate change is essential but simulating and understanding the climate over land is difficult. The ocean surface is relatively homogeneous and has a constant, inexhaustible water supply for evaporation. Conversely, land surfaces are massively diverse, with spatially-varying soil moisture, vegetation, albedo, and surface elevation. The complexity of land surfaces is difficult to simulate and this is reflected in the large uncertainties in model projections of future soil moisture levels, for example.

To address this complexity, we use a hierarchy of models to understand land-ocean contrasts under climate change. The first step on our model hierarchy is the development of simple theories for the response of land temperature, relative humidity, and the water cycle (specifically the time-mean precipitation minus evaporation) to changes in climate. The simple theories for the warming contrast and land relative humidity are first applied to idealized simulations over a wide range of climates with various land configurations and a simplified land surface hydrology. These reduced-complexity simulations allow us to systematically investigate how, for example, the warming contrast is controlled by continental geometry or the soil moisture level. The physical insights gained from these idealized simulations enable us to better understand the land-ocean contrasts in full complexity simulations from the Coupled Model Intercomparison Project 5 (CMIP5), the top of our model hierarchy.

We begin by developing a theory for the land-ocean warming contrast and applying it to idealized and CMIP5 simulations (Chapters 2 and 3). Decreases in land relative humidity under warming are then investigated using a simple conceptual model and a variety of simulations (Chapter 4). Finally, we introduce an extended thermodynamic scaling to understand changes in the terrestrial water cycle in CMIP5 simulations (Chapter 5), before summarizing our findings and pointing towards future work (Chapter 6). Discussions of the literature and the current state of understanding of each topic are presented in the individual chapters.

Chapter 2

Warming contrast: Idealized GCM

©American Meteorological Society 2013[1]

2.1 Introduction

A robust feature of simulations and observations of global warming is that land surface temperatures increase to a greater extent than ocean surface temperatures (e.g., Manabe et al., 1991; Sutton et al., 2007). This land-ocean surface warming contrast is not predominantly a transient effect due to the different thermal inertias of the land and ocean regions; rather it appears to be a fundamental response of the climate system to global warming that persists in the equilibrium response of the system. In addition to the importance of the land-ocean warming contrast for societal impacts of climate change, it may also be expected to play a dynamical role by influencing features of the general circulation such as stationary waves.

Several previous studies have investigated the land-ocean warming contrast in fully-coupled general circulation model (GCM) simulations (e.g., Sutton et al., 2007; Lambert and Chiang, 2007; Fasullo, 2010; Boer, 2011). The contrast is often characterized in terms of an amplification factor $A \equiv \delta T_\mathrm{L}/\delta T_\mathrm{O}$, where δ indicates a change between two climates and T_L and T_O are the surface air temperatures over land and ocean, respectively. Using twenty models from the World Climate Research Programme's Coupled Model Intercomparison Project phase 3 archive (WCRP CMIP3; Meehl et al., 2007), Sutton et al. (2007) found that the amplification factor based on global-mean surface air temperature varies from 1.36 to 1.84 depending on the model, with a multimodel mean of 1.55. The amplification factor also varies with latitude, with a minimum of $\sim$1.2 in the tropics and a maximum of $\sim$1.6 in the subtropics in the multimodel mean. The amplification factor remains approximately constant as the radiative forcing increases but is somewhat smaller in equilibrium simulations with a "slab" ocean (multimodel mean of 1.33) compared with transient simulations with a coupled atmosphere-ocean model (multimodel mean of 1.55).

---

[1] This chapter is a partial reproduction of Byrne and O'Gorman (2013a). We have slightly expanded the discussion of the midlatitude theory in Section 2.5.2 and have included estimates of the midlatitude warming contrast using this theory in Figure 2-11b.

The land-ocean surface warming contrast is also evident in the observational record of recent decades (Sutton et al., 2007; Lambert and Chiang, 2007; Drost et al., 2012). The amplification factors derived from observations and models have similar latitudinal structures and comparable low-latitude (40°S to 40°N) magnitudes (Sutton et al., 2007). However, agreement between observations and models, and indeed between the models themselves, is poor in the middle to high latitudes of the Northern Hemisphere, which may be partly related to the disparate ice and land-surface parameterizations and aerosol forcings employed by the various models.

Differences in the surface energy budget over land and ocean have been invoked to account for the existence of an equilibrium warming contrast (e.g., Manabe et al., 1991; Sutton et al., 2007; Izumi et al., 2014). Assume, for example, that a surface radiative forcing is applied with equal magnitude over land and ocean. Because of less surface moisture availability over land, cooling by dry-sensible and longwave-radiative fluxes represent a greater portion of the increase in surface cooling required to balance the energy budget, implying a land-ocean contrast in changes in surface air temperature and air-surface temperature disequilibrium (the difference between surface air and surface skin temperature). This simple argument suggests that the land-ocean warming contrast should be larger for drier land regions, as is found to some extent in simulations and observations, although changes in aridity and low cloud cover are also important, even in moist regions (Joshi et al., 2008; Doutriaux-Boucher et al., 2009; Fasullo, 2010). Lambert and Chiang (2007) extend the surface energy approach by including a land-ocean heat flux which helps to maintain the relatively constant amplification factor that is a feature of observations and simulations (Huntingford and Cox, 2000; Sutton et al., 2007). Although these arguments provide an intuitive understanding of why one might expect a land-ocean warming contrast to exist, the surface energy budget alone is not sufficient to give a quantitative estimate of the warming contrast: even if changes in surface relative humidity, soil moisture, and downwelling radiative fluxes are taken as given, the surface energy budget still depends on changes in air-surface temperature disequilibrium in addition to the changes in surface air temperature that we wish to estimate.

Other authors have focused on the role of the ocean in controlling the land-ocean warming contrast. Analysis of a variety of coupled and uncoupled GCM simulations shows that the land-ocean warming contrast is present in interannual variability and suggests that the interaction between ocean and land is asymmetric, causing the land surface temperature to be more sensitive to the ocean surface temperature than the ocean surface temperature is to the land surface temperature (Compo and Sardeshmukh, 2008; Dommenget, 2009) [although the degree of asymmetry is not generally agreed upon (Lambert et al., 2011)]. It is further argued that the majority of land warming in response to anthropogenic forcing is actually forced indirectly by the warming ocean and not by local radiative forcing (Dommenget, 2009).

Rather than attempting to relate land-ocean temperature differences to local energy budgets, Joshi et al. (2008) argue that atmospheric processes provide a strong constraint on the land-ocean warming contrast. Tropospheric lapse rates behave differently over land and ocean because of limited moisture availability over land. If a level exists in the atmosphere at which there is no warming contrast (or no temperature contrast in our version of the theory), then different changes in lapse rates over land and ocean imply different changes in surface air temperature. Furthermore, the constraint from atmospheric processes may apply over a range of timescales and local radiative forcing over land is not required to obtain an amplification factor greater than unity. This approach is attractive in that it does not involve surface energy fluxes explicitly (which depend on several factors in addition to surface temperature), but it does require an understanding of tropospheric lapse rates in different regimes.

Our study differs from previous studies by investigating the land-ocean warming contrast over a wide range of climates, and by comparing theory with simulations from an idealized GCM using a variety of land configurations. The land configurations chosen provide control, ocean-only, hemispheres which facilitate a straightforward comparison of land and ocean temperatures (with the exception of simulations with a meridional land band in which induced stationary waves make interpretations more difficult). Our idealized simulations permit a systematic evaluation of the response of land-ocean temperature contrasts to radiative forcing; such a systematic evaluation is more difficult to accomplish with a full-complexity GCM in which ocean circulations, topography, ice and snow coverage, fixed continents, and other factors make interpretations more troublesome.

We begin by developing a simple theory to estimate the magnitude of the warming contrast (Section 2). The theory is based on the hypothesis of Joshi et al. (2008) that it arises from different lapse rates over land and ocean owing to differences in moisture availability, although we make somewhat different assumptions from Joshi et al. (2008) regarding how the lapse rates are set. We then explore how the warming contrast varies with latitude and with land configuration in a range of simulations with the idealized GCM (Section 3). Climate is varied in the idealized GCM by prescribing changes in longwave absorber as a representation of changes in greenhouse gas concentrations, or by prescribing different evaporative fractions to directly test the effects of land aridity. Results from the simulations are presented for subtropical (Section 4) and higher-latitude (Section 5) land surfaces. Extensions of the theory to account for the the effect of eddies on the extratropical stratification are discussed (Section 5b). The sensitivities of the land-ocean warming contrast to water vapor radiative feedbacks and land-ocean albedo contrasts are assessed with additional sets of simulations (Section 6). In all cases, the simulation results are compared to the simple theory. Differences between warming contrasts as measured by surface air temperatures and surface skin temperatures are also described (Section 7). The paper

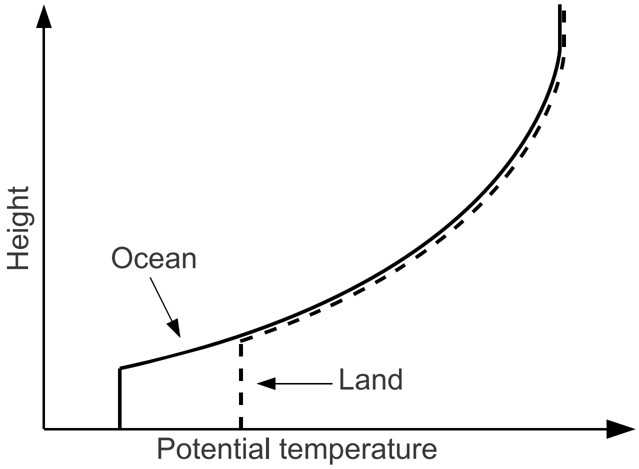

Figure 2-1: Schematic diagram of potential temperature vs. height for moist adiabats over land and ocean and equal temperatures at upper levels. A land-ocean surface air temperature contrast is implied by different LCLs over land and ocean.

concludes with a summary and a brief discussion of outstanding questions (Section 8).

2.2 Theory

We introduce a simple theory that allows for the estimation of the land-ocean surface air temperature difference and warming contrast based on the ocean surface air temperature, T_{O}, and the surface relative humidities over ocean and land, $\mathcal{H}_{\mathrm{O}}$ and $\mathcal{H}_{\mathrm{L}}$, respectively. We are motivated by the hypothesis of Joshi et al. (2008) that the land-ocean contrast is constrained by different changes in lapse rates over land and ocean caused by differences in surface moisture availability.

Joshi et al. (2008) make the assumption that the land-ocean warming contrast vanishes sufficiently high in the atmosphere (i.e., temperature changes over land and ocean are equal at such heights). We make the stronger assumption that the land and ocean temperatures in a given climate are equal high in the atmosphere. This assumption simplifies the analysis and should be approximately valid in the tropics because of weak temperature gradients in the tropical free troposphere (e.g., Sobel and Bretherton, 2000). Idealized GCM simulations discussed later suggest that the assumption of equal land and ocean temperatures aloft may also be adequate in some cases in the extratropics.

Our second assumption is that lapse rates are moist adiabatic in the mean over land and ocean. By moist adiabatic lapse rates we mean dry adiabatic lapse rates below the lifted condensation level (LCL) and saturated moist adiabatic lapse rates above it, such that a parcel lifted from near the surface is neutrally buoyant with respect to the mean state of the atmosphere.[2] This assumption implies that our theory is appropriate to the tropics and falls into the class of theories based on convective quasi-equilibrium (e.g., Arakawa and Schubert, 1974; Emanuel, 2007). In our application of convective quasi-equilbrium, convection is assumed to be sufficiently active so as to maintain moist adiabatic lapse rates in the mean despite large-scale dynamical and radiative forcing.

With these two assumptions, the lapse rates over land and ocean only differ in the vertical range between the LCL over ocean and the LCL over land (Fig. 2-1). The LCL is higher over land because of lower surface moisture availability. In the vertical range between the LCLs a saturated moist adiabatic lapse rate, Γ_m^*, occurs over ocean and a dry adiabat, Γ_d, occurs over land. Warming results in a reduction in Γ_m^* but leaves Γ_d unchanged. Combined with the assumption of equal temperatures above the LCLs, this implies a greater surface warming over land than ocean. Changes in surface relative humidity affect the LCLs and may also modify the warming contrast. Note that the higher LCL over land implies not only a land-ocean warming contrast, but also a higher surface temperature over land than ocean in the current climate, all else being equal.

Our assumptions allow for the prediction of the land surface air temperature from the ocean surface air temperature and the surface relative humidities over land and ocean. For example, using the air temperature and relative humidity at the ocean surface, we can integrate upwards along the moist adiabatic lapse rate from the surface

---

[2] Joshi et al. (2008) do not assume that mean lapse rates are moist adiabatic over land and ocean in this sense, but instead give an illustrative example in which the lower-tropospheric lapse rate is a weighted average of dry and saturated moist adiabatic lapse rates, with weightings depending on relative humidity.

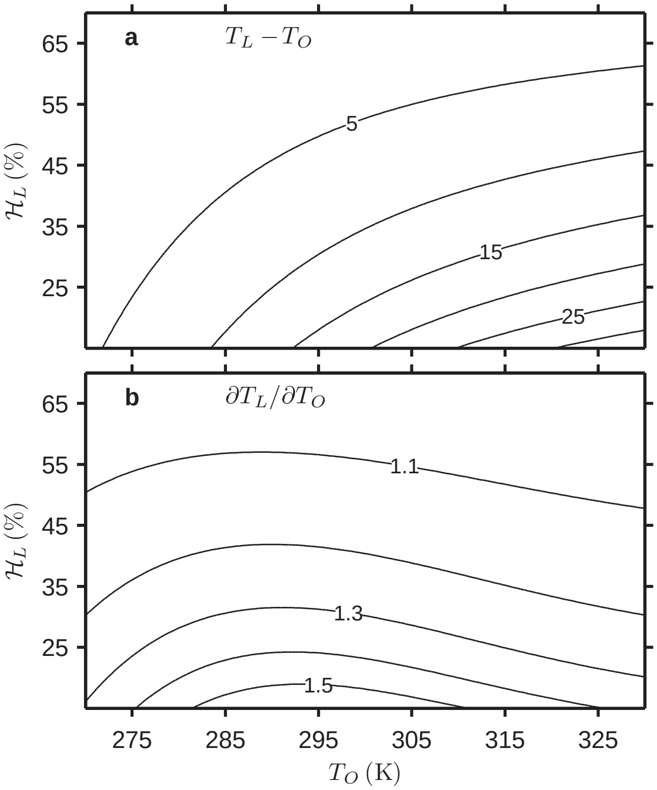

Figure 2-2: Theoretical values of (a) the land-ocean surface air temperature difference $T_\mathrm{L} - T_\mathrm{O}$ (contour interval 5 K) and (b) the amplification factor $A^T = \partial T_\mathrm{L}/\partial T_\mathrm{O}$ (contour interval 0.1) at constant relative humidities for a range of surface relative humidities over land and temperatures over ocean. Surface relative humidity over ocean is fixed at 80%. The temperature differences and amplification factors are calculated by numerically solving the equal equivalent potential temperature equation (2.1).

to the level at which the temperature becomes equal over land and ocean. Using this temperature aloft and the surface relative humidity over land, we can then solve iteratively for the surface air temperature over land (again assuming moist adiabatic lapse rates). In practice, it is simpler to use the equivalent potential temperature, θ_e, which we take to be conserved for dry and pseudoadiabatic displacements. The theory amounts to assuming equal surface air θ_e over land and ocean:

$$\theta_e(T_L, \mathcal{H}_L) = \theta_e(T_O, \mathcal{H}_O). \tag{2.1}$$

Figure 2-2a shows temperature contrasts for solutions to equation (2.1) for a fixed

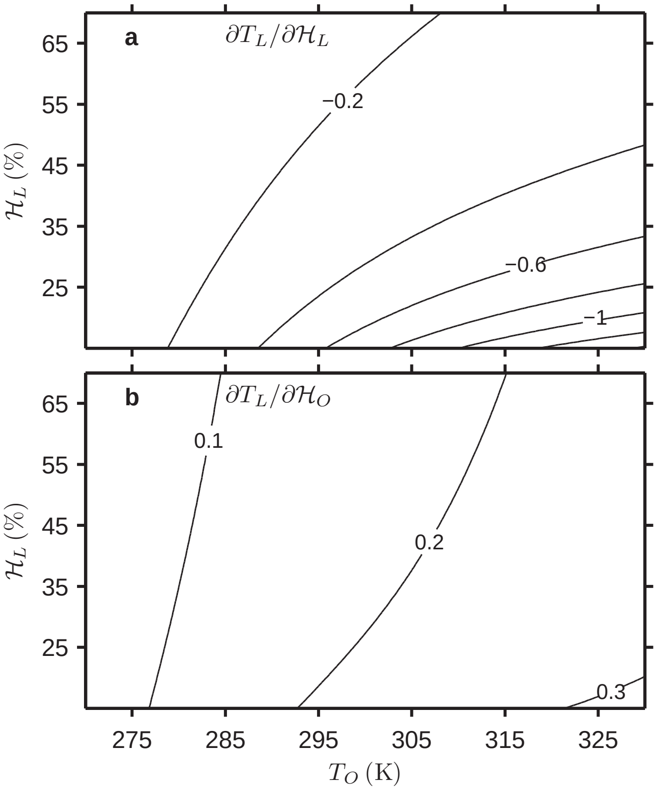

Figure 2-3: Theoretical values for the partial derivatives of land surface air temperature with respect to (a) surface relative humidity over land, $\partial T_{\mathrm{L}}/\partial \mathcal{H}_{\mathrm{L}}$, and (b) surface relative humidity over ocean, $\partial T_{\mathrm{L}}/\partial \mathcal{H}_{\mathrm{O}}$, as a function of land relative humidity and ocean temperature [contour interval $0.2\mathrm{K}\,\%^{-1}$ in (a) and $0.1\mathrm{K}\,\%^{-1}$ in (b)]. Surface relative humidity over ocean is fixed at 80%. The partial derivatives are calculated by numerically solving the equal equivalent potential temperature equation (2.1).

ocean surface relative humidity of 80% and a range of values of ocean surface air temperature and land surface relative humidity.[3] The temperature contrast is an increasing function of temperature and a decreasing function of surface relative humidity over land; it reaches a value of 25K for an ocean temperature of 320K and a land surface relative humidity of 20%.

---

[3] We calculate θ_e using Eq. (9.40) from Holton (2004), with the temperature at the LCL evaluated using Eq. (22) from Bolton (1980). It will later be important that the θ_e used is consistent with the convection scheme in the idealized GCM. We tested this by calculating the land-ocean surface air temperature contrast, $T_{\mathrm{L}} - T_{\mathrm{O}}$, implied by (2.1) using two different means of calculating θ_e: firstly using the θ_e formula mentioned above, and secondly by lifting a surface air parcel pseudoadiabatically to the top pressure level of the GCM (at which essentially all water has been removed from the parcel) using the saturated moist adiabatic lapse rate that is incorporated in the GCM (Appendix D.2 Holton, 2004) and then returning to the surface along a dry adiabat. For example, based on a land surface relative humidity of 40%, an ocean surface relative humidity of 80%, and an ocean surface air temperature of 290 K, the land-ocean temperature contrast was approximately 6 K and the difference between the two estimates described above was 0.25 K. Thus, we conclude that the formula used for θ_e is adequate for our study.

In the limit of an infinitesimal change in climate, the amplification factor may be written as

$$\begin{aligned} A = \frac{dT_\mathrm{L}}{dT_\mathrm{O}} &= \frac{\partial T_\mathrm{L}}{\partial T_\mathrm{O}} + \frac{\partial T_\mathrm{L}}{\partial \mathcal{H}_\mathrm{L}}\frac{d\mathcal{H}_\mathrm{L}}{dT_\mathrm{O}} + \frac{\partial T_\mathrm{L}}{\partial \mathcal{H}_\mathrm{O}}\frac{d\mathcal{H}_\mathrm{O}}{dT_\mathrm{O}} \\ &= A^T + A^\mathcal{H}_\mathrm{L} + A^\mathcal{H}_\mathrm{O}, \end{aligned} \tag{2.2}$$

where $A^T = \partial T_\mathrm{L}/\partial T_\mathrm{O}$ is the component of the amplification factor arising from changes in temperature at fixed relative humidity, while $A^\mathcal{H}_\mathrm{L} = (\partial T_\mathrm{L}/\partial \mathcal{H}_\mathrm{L})(d\mathcal{H}_\mathrm{L}/dT_\mathrm{O})$ and $A^\mathcal{H}_\mathrm{O} = (\partial T_\mathrm{L}/\partial \mathcal{H}_\mathrm{O})(d\mathcal{H}_\mathrm{O}/dT_\mathrm{O})$ are the contributions to A due to changes in land and ocean surface relative humidities, respectively. All partial derivatives are calculated assuming equal equivalent potential temperatures over land and ocean according to (2.1). The amplification factor at constant relative humidity, A^T, increases monotonically with decreasing relative humidity over land (Fig. 2-2b). However, the amplification factor varies non-monotonically with temperature and has a maximum at an ocean surface air temperature of roughly 293 K. This non-monotonic behavior arises because although the saturated moist adiabatic lapse rate is a monotonically decreasing function of temperature, it has an inflection point with respect to temperature at approximately 273K (calculated at 900hPa) which gives rise to the peak in the amplification factor. The amplification factor depends on the lapse rates in the layer between the LCLs over land and ocean (cf. Fig. 2-1), and the temperature of this layer is lower than that of the surface. As a result, the maximum in Fig. 2-2b occurs at a surface air temperature of 293K that is higher than the inflection-point temperature of 273K.

Changes in surface relative humidity under global warming must also be taken into account; decreases of up to $2\%\,\mathrm{K}^{-1}$ over land were found by O'Gorman and Muller (2010) for a multimodel mean of CMIP3 simulations. The change in land surface air temperature for a given change in land surface relative humidity at constant ocean surface air temperature, $\partial T_\mathrm{L}/\partial \mathcal{H}_\mathrm{L}$, is plotted in Figure 2-3a. For an ocean surface air temperature of 295 K and land and ocean surface relative humidities of 50% and 80%, respectively, $\partial T_{\mathrm{L}}/\partial \mathcal{H}_{\mathrm{L}} \approx -0.2\,\mathrm{K}\,\%^{-1}$, and taking $d\mathcal{H}_{\mathrm{L}}/dT_{\mathrm{O}} \approx -2\%\,\mathrm{K}^{-1}$, we find that $A_{\mathrm{L}}^{\mathcal{H}} \approx 0.4$. This demonstrates that changes in land relative humidity may contribute significantly to the amplification factor according to the theory.

Changes in ocean surface relative humidity in simulations of climate change are generally smaller than changes over land (O'Gorman and Muller, 2010) and are thought to be energetically constrained (Schneider et al., 2010). For a typical increase in ocean surface relative humidity of $0.5\%\,\mathrm{K}^{-1}$, and again taking an ocean surface air temperature of 295 K and land and ocean surface relative humidities of 50% and 80%, respectively, we find that $\partial T_{\mathrm{L}}/\partial \mathcal{H}_{\mathrm{O}} \approx 0.15\,\mathrm{K}\,\%^{-1}$ (Fig. 2-3b) and $A_{\mathrm{O}}^{\mathcal{H}} \approx 0.08$, which is considerably smaller than the contribution from land relative humidity variations (calculated above as $A_{\mathrm{L}}^{\mathcal{H}} \approx 0.4$).

Given that the theory relies on lapse rates being close to moist adiabatic in the mean, as follows from convective quasi-equilibrium in the convecting regions of the tropics, we refer to it as a convective quasi-equilibrium theory of the surface warming contrast. In the presence of other stabilizing influences on the stratification in addition to convection (such as large-scale eddies in the extratropics), the theory is not strictly applicable although it may still be a useful guide. The extension of the theory to include the effects of large-scale eddies on the extratropical thermal stratification is discussed in Section 2.5.

A simple generalization of the theory is possible, also consistent with the concept of convective quasi-equilibrium, in which lapse rates are not assumed to be exactly moist adiabatic, but rather the departures of lapse rates from moist adiabatic are assumed to remain constant as climate changes. This generalized theory may be formulated by assuming that the surface air equivalent potential temperatures are not necessarily equal over land and ocean, but that their changes are. The land-ocean warming contrast will be higher than for the standard theory if the surface air equivalent potential temperature is higher over ocean than land. The temperature at which the theoretical maximum amplification factor occurs is not strongly affected. The generalized theory does not give more accurate predictions for the idealized

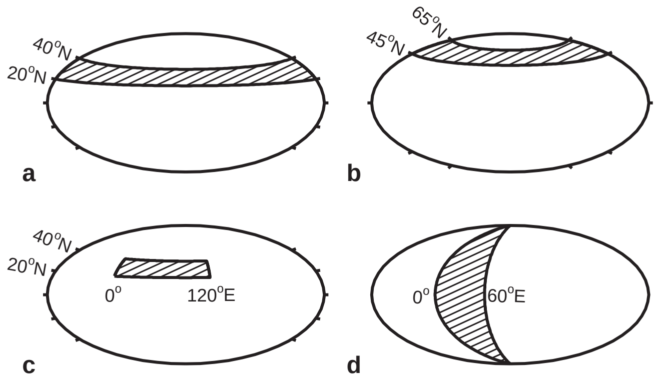

Figure 2-4: Simulations are performed using a variety of land configurations: (a) and (b) indicate zonal bands from 20°N to 40°N and from 45°N to 65°N, respectively, (c) is a continent spanning 20°N to 40°N and 0°E to 120°E, and (d) is a meridional band from 0°E to 60°E.

simulations presented here, but it may be useful for more realistic simulations or observations. We discuss this generalized theory in more detail in the next chapter.

2.3 Idealized GCM

2.3.1 Land configurations

The idealized GCM has a lower boundary consisting of various configurations of land and a mixed-layer ocean (Fig. 2-4). Simulations are performed with zonal land bands in the subtropics (20°N to 40°N) and extratropics (45°N to 65°N), a continent of finite zonal extent (20°N to 40°N, 0°E to 120°E), and a meridional land band (0°E to 60°E).

2.3.2 Model and simulations

We use a moist idealized GCM similar to that of Frierson et al. (2006) and Frierson (2007), with the specific details documented by O'Gorman and Schneider (2008b) except for the introduction of land hydrology (described later in this section) and an alternative radiation scheme that allows for water vapor radiative feedback (described in Section2.6.1). The model is based on a version of the Geophysical Fluid

Dynamics Laboratory (GFDL) dynamical core and solves the hydrostatic primitive equations spectrally at T42 resolution with 30 vertical sigma levels. Moist convection is parameterized using a simplified version of the Betts-Miller scheme (Frierson, 2007) in which temperatures are relaxed to a moist adiabat and humidities are relaxed to a reference profile with a relative humidity of 70%. A large-scale condensation scheme prevents gridbox supersaturation. Re-evaporation of precipitation is not permitted, and only the vapor-liquid phase change of water is considered. The top-of-atmosphere insolation is a representation of an annual-mean profile and there is no diurnal cycle.

Longwave radiative fluxes are calculated using a two-stream gray radiation scheme, and shortwave heating is specified as a function of pressure and latitude. A range of climates is simulated by varying the longwave optical thickness as a representation of the radiative effects of changes in water vapor and other greenhouse gases. In the default radiation scheme, the longwave optical thickness is specified and does not depend explicitly on the water vapor field, excluding all radiative feedbacks of water vapor or clouds. Both longwave and shortwave cloud radiative effects are excluded in the model. The longwave optical thickness is specified by $\tau = \alpha\tau_{\mathrm{ref}}$, where τ_{ref} is a function of latitude and pressure, and the parameter α is varied[4] over the range $0.2 \leq \alpha \leq 6$. The reference value of $\alpha = 1$ corresponds to an Earth-like climate with a global-mean surface air temperature of 288 K for the simulation with a subtropical land band.

The land and ocean surfaces have the same albedo (0.38) and heat capacity (corresponding to a layer of liquid water of depth 1 m and specific heat capacity $3989\,\mathrm{J\,kg^{-1}\,K^{-1}}$). The effect of a land-ocean albedo contrast on the warming contrast is explored in Section 2.6.2. Horizontal heat transport is not permitted below either surface. Surface fluxes are calculated using bulk aerodynamic formulae and Monin-Obukhov similarity theory, with roughness lengths of 5×10^{-3} m for momentum and 10^{-5} m for moisture and sensible heat over both land and ocean. A k-profile scheme is used to parameterize boundary layer turbulence (Troen and Mahrt, 1986).

---

[4] There are 9 simulations for each of the subtropical and midlatitude zonal land bands and the subtropical continent (α values of 0.2,0.4,0.7,1.0,1.5,2.0,3.0,4.0,6.0).

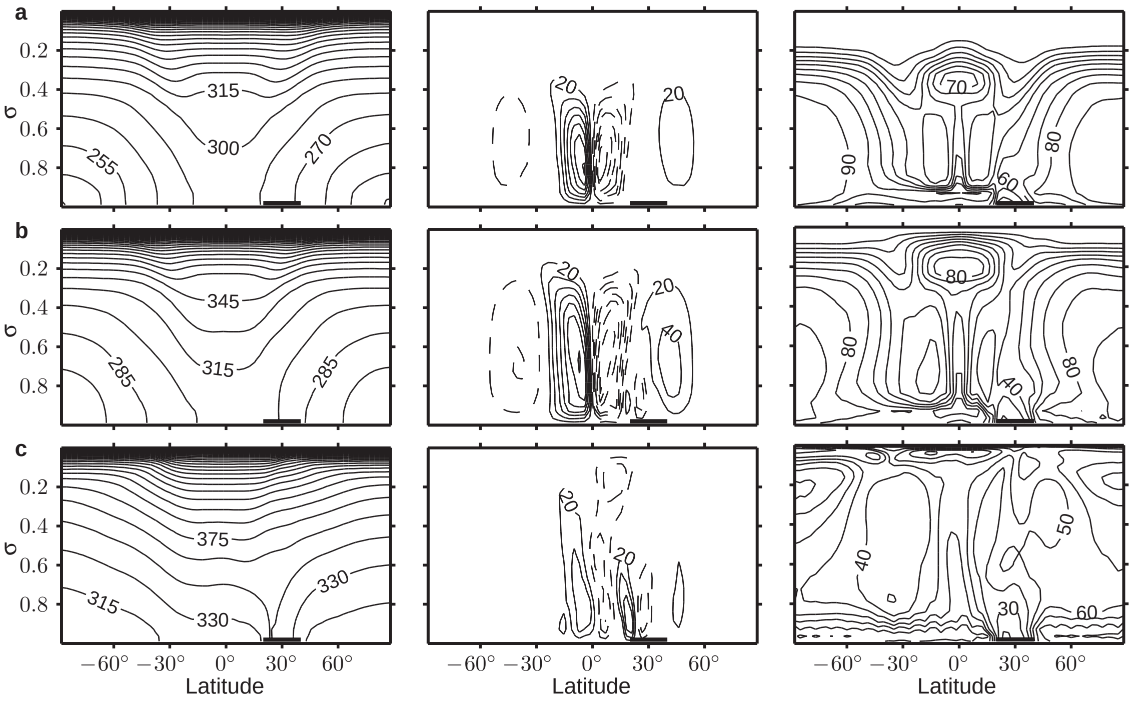

Figure 2-5: The zonal and time mean potential temperature (left, contour interval 15 K), Eulerian-mean streamfunction (center, contour interval $20 \times 10^9\,\mathrm{kg\,s^{-1}}$, with negative values given by dashed contours), and relative humidity (right, contour interval 10%) for a zonal land band from 20°N to 40°N in (a) a cold simulation ($\alpha = 0.4$), (b) the reference simulation ($\alpha = 1$), and (c) the warmest simulation ($\alpha = 6$). The heavy black bars indicate the position of the subtropical zonal land band (20°N to 40°N).

The simple bucket model of Manabe (1969) is used to simulate the land surface hydrology. The field capacity, S_{FC}, in the bucket model is the maximum amount of water that can be held per unit area of land surface and has dimensions of depth. Field capacity generally depends on soil type, vegetation, and other factors, but we set $S_{\mathrm{FC}} = 0.15\,\mathrm{m}$ for simplicity [as in Manabe (1969)]. Soil moisture, S, also has dimensions of depth and evolves according to

$$\frac{dS}{dt} = \begin{cases} P - E & \text{if } S < S_{\mathrm{FC}} \text{ or } P \leq E \\ 0 & \text{if } S = S_{\mathrm{FC}} \text{ and } P > E, \end{cases}$$

where P and E are the precipitation and evaporation rates, respectively. Accordingly, soil moisture accumulates when precipitation exceeds evaporation until the field capacity is reached, at which point any subsequent excess of precipitation over evaporation is assumed to run off. Evaporation over land is given by $E_{\mathrm{L}} = \beta E_0$, where β is the evaporative fraction and E_0 is the potential evaporation rate (the evaporation rate obtained over a saturated land surface using bulk aerodynamic formulae). The evaporative fraction β is specified as a linear function of soil moisture up to an upper bound of 1,

$$\beta = \begin{cases} 1 & \text{if } S \geq \gamma S_{\mathrm{FC}} \\ S/(\gamma S_{\mathrm{FC}}) & \text{if } S < \gamma S_{\mathrm{FC}}, \end{cases}$$

where $\gamma = 0.75$. This definition ensures that the soil moisture cannot become negative and that the potential evaporation rate is reached before soil moisture reaches the field capacity. Although the bucket model ignores complexities such as canopy cover and stomatal effects [see Seneviratne et al. (2010) for a review of soil moisture–climate interactions], it is adequate for the purposes of exploring the effect of limited surface moisture availability on the response of surface air temperatures and atmospheric lapse rates to changes in radiative forcing.

Simulations are spun up for either 3000 days (for $\alpha < 1$ and meridional band simulations), 1500 days (midlatitude zonal band, fixed evaporative fraction simulations), or 1000 days ($\alpha \geq 1$) from an isothermal rest state. Longer spinup times are required in colder climates because specific humidities and water vapor fluxes are smaller in magnitude, with the result that soil moisture values take longer to reach statistical equilibrium. Time averages are taken over the 500 day period after spinup (or over the 1000 days after spinup in the case of the midlatitude zonal band, fixed evaporative fraction simulations). Similar results are found using a 200-day average. For example, differences between the land-ocean temperature contrast for the 200-day and 500-day averages are less than 0.3K for the subtropical land band simulations.

2.3.3 Zonal-mean climatology (subtropical zonal land band)

Figure 2-5 shows the mean potential temperature, meridional streamfunction, and relative humidity for three simulations ($\alpha = 0.4$, 1 and 6) with a subtropical zonal land band from 20°N to 40°N. In the cold simulation ($\alpha = 0.4$), the land does not have a strong influence on the atmospheric state beyond a moderate decrease in the low-level relative humidity over the land band. The reduction in relative humidity is greater in the reference simulation ($\alpha = 1$), and it is a dominant feature in the warm simulation ($\alpha = 6$) in which it extends upwards from the surface to $\sigma \simeq 0.5$, where σ is pressure normalized by surface pressure. The enhanced warming over land affects the near-surface temperature structure by weakening the meridional temperature gradient equatorward of the land band and strengthening the gradient on the poleward side in the reference simulation; it causes a reversed temperature gradient on the equatorward side of the land band in the warmest simulation. Shallow monsoon circulations are evident in both the reference and warmest simulations. The quasi-equilibrium theory of monsoons associates the upward branch of direct thermal circulations with local boundary-layer maxima in either equivalent potential temperature or potential temperature (Emanuel, 1995). An observational analysis of the various regional monsoons on Earth by Nie et al. (2010) shows that two distinct circulation types exist: one is a deep and moist circulation (with upward branch near the boundary-layer maximum of equivalent potential temperature), and the other is a mixed circulation composed of a shallow dry cell (with upward branch near the boundary-layer maximum in potential temperature) superimposed on the deep moist cell. The monsoon circulations in our simulations show some similarities to the mixed circulations observed by Nie et al. (2010); the addition of a seasonal cycle to our GCM might lead to a closer resemblance by shifting the boundary-layer maximum in equivalent potential temperature poleward in summer. A more detailed study of the changing strength and character of these monsoonal circulations as the climate is varied is left to future work.

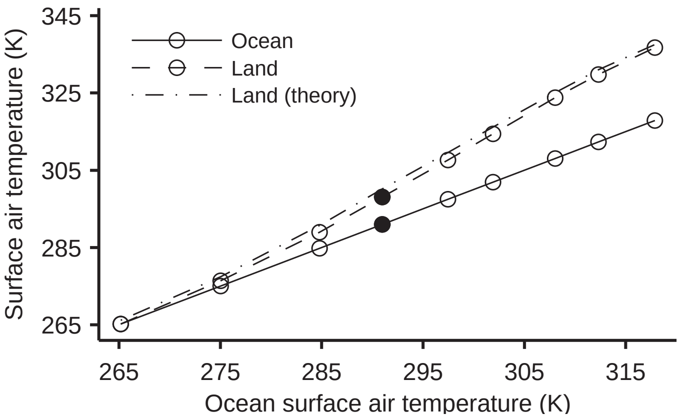

Figure 2-6: Surface air temperature over ocean (solid line with circles) and land (dashed line with circles) vs. ocean surface air temperature for a subtropical zonal land band from 20°N to 40°N. Filled circles denote the reference simulation ($\alpha = 1$) here and in subsequent figures. The dashed-dotted line is the estimate of surface air temperature over land from theory.

2.4 Subtropical warming contrast

2.4.1 Subtropical zonal land band

We consider the simulations with a subtropical zonal land band from 20°N to 40°N. The land surface air temperature for a given simulation, T_{L}, is defined as the temperature of the lowest atmospheric level ($\sigma = 0.989$) averaged in time and over all land gridpoints (with area weighting). To make meaningful comparisons of land and ocean regions, we define the ocean surface air temperature to be the average of the lowest-level temperatures over the corresponding region in the other hemisphere. For example, in the case of the zonal land band from 20°N to 40°N, the ocean surface air temperature, T_{O}, is calculated by averaging over 20°S to 40°S.

The land-ocean contrast in temperature is close to zero in the coldest climate and increases in magnitude as the climate warms, reaching 19K in the warmest simulation (Fig. 2-6). The land-ocean amplification factor has a mean value of 1.4 over all simulations and varies non-monotonically with ocean temperature (Fig. 2-7). The mean value is of similar magnitude to the Sutton et al. (2007) low-latitude (40°S to 40°N) estimates of 1.51 and 1.54 for climate-model simulations and observations, respectively, although close agreement with our simulations is not necessarily expected

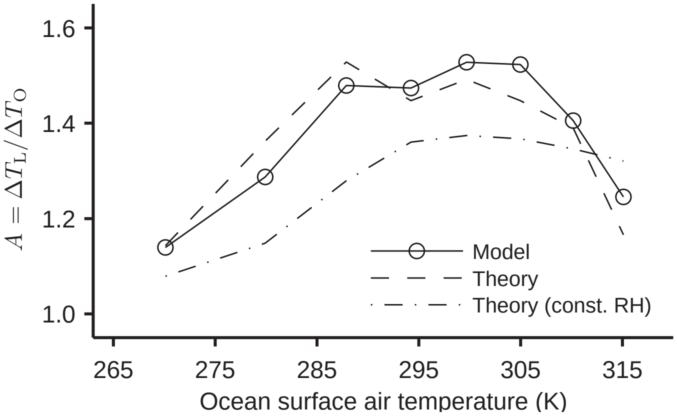

Figure 2-7: The amplification factor vs. ocean surface air temperature in simulations with a subtropical land band from 20°N to 40°N (solid line with circles), from theory (dashed line), and from theory neglecting changes in relative humidity (dashed-dotted line). The amplification factor is calculated based on temperature differences between pairs of nearest-neighbor simulations and is plotted against the mid-point ocean temperature for each pair. The amplification factor from theory is obtained in the same way, but using the theoretical estimates of the land temperature based on mean surface relative humidities (dashed-dotted line in Fig. 2-6). The amplification factor from theory neglecting changes in relative humidities [corresponding to A^T in (3.2)], is evaluated using the mean surface relative humidity from the colder of the pair of simulations when estimating the land temperature in the warmer simulation.

given the differences in continental configuration, surface aridity and heat capacity, and radiative forcing.

The estimate of T_{L} based on theory matches the simulated land temperatures well over the full range of simulations, with an overestimation of T_{L} of order 1K in each simulation (dashed-dotted line in Fig. 2-6). For the theory, the equivalent potential temperatures in equation (2.1) are evaluated using T_{O} and the mean surface relative humidities (evaluated at the lowest model level) averaged in time and over land or the corresponding region over ocean. The estimates of the amplification factor from theory are also accurate (dashed line in Fig. 2-7). There is a maximum in the simulated amplification factor at $T_{\mathrm{O}} \simeq 300\,\mathrm{K}$, which is higher than the temperature at which the theoretical maximum occurs for constant relative humidities (cf. Fig. 2-2b), but these should not be directly compared because of changes in the relative humidities in the simulations. In the coldest simulation ($\alpha = 0.2$), the surface relative humidities over land and ocean are 51% and 74%, respectively. Ocean relative humidity remains approximately constant over the full range of climates, but land relative humidity decreases with warming to 24% in the reference simulation ($\alpha = 1$), and remains roughly unchanged over the warmer simulations (not shown). The impact of changes in relative humidity is illustrated by comparison with the theoretical amplification factors assuming unchanged relative humidities (dashed-dotted line in Fig. 2-7). Not accounting for changes in relative humidity results in a substantial underestimation of the amplification factor for all but the warmest two simulations (between which the land relative humidity increases slightly), indicating that the land-ocean surface warming contrast is tightly coupled to changes in low-level relative humidity.

We next examine the accuracy of each of the assumptions made in the simple theory. A central assumption of the theory is that there is some level at which the land-ocean temperature difference vanishes, and this is found to hold in our simulations (Fig. 2-8). The fact that this level rises as the climate warms is not an issue since the theory only requires that such a level exists. The assumption of moist adiabatic lapse rates below this level is accurate over ocean, but it is not very accurate over land (Fig. 2-9), which may be related to moist convection occurring less frequently over the relatively dry land (cf. Fig. 2-5c). The vertical temperature profile over land in the GCM simulations is generally more stable than moist adiabatic and this is consistent with the slight overestimation of the land-ocean surface air temperature contrast using the convective quasi-equilibrium theory (Fig. 2-6).

The deviation of the mean thermal stratification from moist adiabatic over land is not as great as might be inferred from comparison with a moist adiabat based on mean surface relative humidity (dashed lines in Fig. 2-9). We make a second comparison that allows for variability in low-level relative humidity by using estimated probability density functions (PDFs) of surface relative humidity when calculating the moist adiabats. The PDF-weighted moist adiabatic lapse rate $\Gamma_m^{\mathrm{pdf}}(\sigma)$ at a given level σ is computed as

$$\Gamma_m^{\mathrm{pdf}}(\sigma) = \int_0^{100\%} f(\mathcal{H})\Gamma_m(T, \mathcal{H}, \sigma)d\mathcal{H}, \tag{2.3}$$

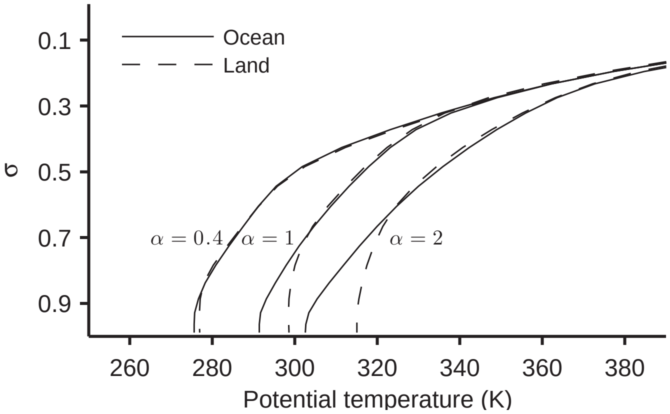

Figure 2-8: Vertical profiles of potential temperature averaged in time and over land (dashed) and the corresponding ocean region (solid) for cold, reference, and warm simulations ($\alpha = 0.4$, 1, and 2, respectively) with a subtropical zonal land band from 20°N to 40°N.

where $f(\mathcal{H})$ is the PDF of surface relative humidity and $\Gamma_m(T, \mathcal{H}, \sigma)$ is the lapse rate at σ for a moist adiabat calculated using a surface air temperature of T and a surface relative humidity of $\mathcal{H}$. Fig. 2-9 shows that Γ_m^{pdf} is a somewhat better approximation to the simulated lapse rates over land compared with lapse rates based on moist adiabats calculated using mean surface relative humidities. We make a corresponding estimate of T_{L} using the PDFs of surface relative humidity over land and ocean rather than the mean values. (We calculate the temperature at the level at which the land-ocean contrast vanishes by integrating Γ_m^{pdf} over ocean from the surface to that level, and we then solve iteratively for T_{L} using Γ_m^{pdf} over land.) The resulting estimates of T_{L} are almost indistinguishable from the estimates using mean surface relative humidities (not shown). These results suggest that although variability in surface relative humidity over land results in variability in the LCL and effectively smooths the time-mean lapse rates in the vertical (Fig. 2-9b), use of mean surface relative humidities is still adequate when applying the equal equivalent potential temperature equation (2.1) to estimate land temperatures.

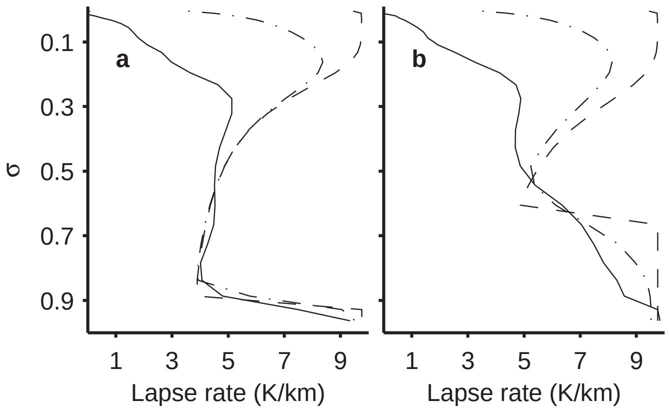

Figure 2-9: Vertical profiles of lapse rates averaged in time and over (a) ocean and (b) land for a warm simulation ($\alpha = 2$ and a global-mean surface air temperature of 302 K) with a subtropical zonal land band from 20°N to 40°N. The solid lines show the simulated lapse rates, the dashed lines correspond to moist adiabats calculated using the mean surface air temperatures and mean surface relative humidities, and the dashed-dotted lines correspond to averages of moist adiabats weighted according to the PDFs of surface relative humidity following (2.3). Note that the theory only requires that the lapse rates be moist adiabatic up to the level at which the temperature profiles converge, approximately $\sigma = 0.6$ for this simulation (Fig. 2-8).

2.4.2 Subtropical continent

The subtropical warming contrast is further investigated using a continent that extends from 20°N to 40°N and 0°E to 120°E (Fig. 2-4c). The ocean temperatures are averaged over 20°S to 40°S and 0°E to 120°E. The land-ocean temperature difference for the continent is smaller than for the corresponding subtropical land band simulations in all but the coldest climate (e.g., it is approximately 2K smaller for $\alpha = 1.5$ and an ocean temperature of 297K). The theoretical estimates match the continental land-ocean temperature contrasts, although the land temperatures are slightly overestimated as for the subtropical band simulations (Fig. 2-10). The reduced warming contrast compared to the zonal land band is consistent with higher surface relative humidity over the continent (28% over the continent vs. 23% over the subtropical band for $\alpha = 1.5$). Higher relative humidity is to be expected over a continent of finite zonal extent because of zonal moisture fluxes from surrounding oceanic regions.

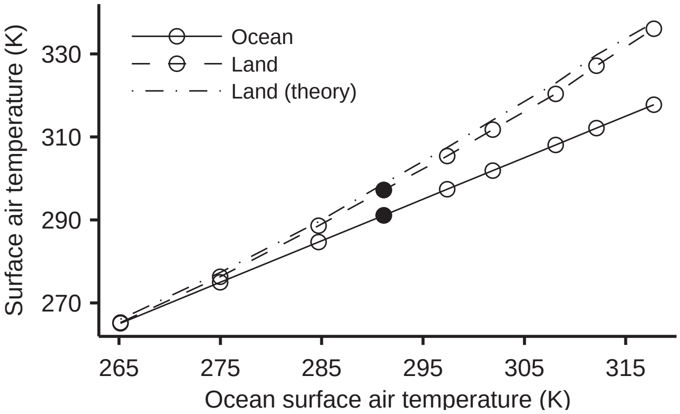

Figure 2-10: Surface air temperature over ocean (solid line with circles) and land (dashed line with circles) vs. ocean surface air temperature for a land continent spanning 20°N to 40°N and 0°E and 120°E. The dashed-dotted line is the estimate of the land temperature from theory.

2.4.3 The effect of aridity

The results above illustrate that limited moisture availability can generate a land-ocean temperature contrast, and that this contrast increases as the climate warms in response to radiative forcing. For the simulations discussed so far, the soil moisture and the evaporative fraction have been dynamic quantities that vary in response to changes in the local balance of evaporation and precipitation as the climate warms. To isolate the effect of aridity on the land-ocean temperature contrast, we perform a series of simulations with fixed longwave optical thickness ($\alpha = 1$) and a range of specified values of the evaporative fraction,[5] β, over a zonal land band from 20°N to 40°N. Reducing the evaporative fraction is a simple means of systematically drying out the land surface; it may also be taken as an analog for decreased soil moisture levels in a warmer climate or reduced stomatal conductance and evaporation in elevated CO_2 environments (e.g., Joshi and Gregory, 2008).

For $\beta = 1$, land and ocean are identical in the idealized GCM. Reducing β from unity inhibits evaporation from the land surface, and the surface relative humidity over land decreases. According to our theory (Fig. 2-2), a reduction in relative humidity over land, along with roughly constant relative humidity and temperature over

---

[5] Simulations with β values of 0.1,0.2,0.3,0.5,0.7,0.8, and 0.9 are performed for both subtropical (20°N to 40°N) and mid-latitude (45°N to 65°N) zonal land bands.

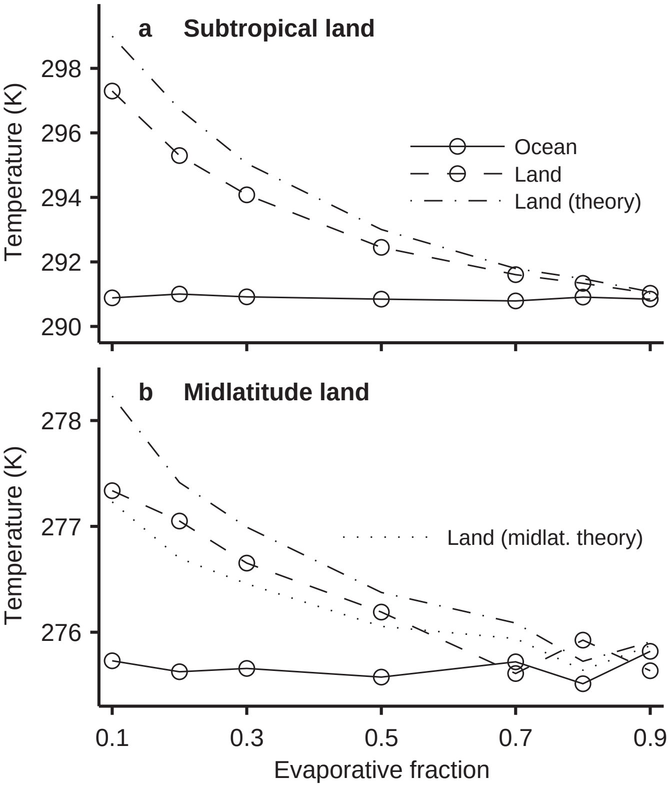

Figure 2-11: Surface air temperature over ocean (solid line with circles) and land (dashed line with circles) vs. evaporative fraction β for (a) a subtropical zonal land band from 20°N to 40°N and (b) a midlatitude zonal land band from 45°N to 65°N. The dashed-dotted lines are the estimates of land temperature from theory, and the dotted line is an estimate of the midlatitude land temperature using a midlatitude version of the theory in which the predicted warming contrast is 0.6 times the contrast estimated from the original theory [following O'Gorman (2011)]. The longwave absorber parameter α has its reference value of unity in all simulations.

ocean, implies an increase in temperature over land so as to maintain equal equivalent potential temperatures over land and ocean. This behavior is found in our idealized model simulations, with the land-ocean temperature contrast increasing strongly as β is lowered, and doing so roughly in accordance with the theory (Fig. 2-11a). However, as the land surface relative humidities decrease, the lapse rates depart to a greater degree from moist adiabats, and surface air equivalent potential temperatures over land and ocean diverge, leading to less precise land temperature estimates from theory. The effect of varying β at midlatitudes is discussed in Section 2.5.1.

2.5 Higher-latitude warming contrast

By considering a zonal land band at midlatitudes and a meridional land band at all latitudes, we next investigate how the land-ocean warming contrast depends on latitude and whether the theory can account for the magnitude of extratropical warming contrasts.

2.5.1 Midlatitude zonal land band

For the midlatitude zonal land band (45°N to 65°N), there is effectively no land-ocean warming contrast when climate change is forced by varying the longwave absorber over the range $0.2 \leq \alpha \leq 6$ (not shown). Moisture flux convergence is sufficient at these latitudes to maintain soil moisture levels close to, or at, field capacity, and land and ocean surfaces behave similarly.

The lack of a land-ocean warming contrast at midlatitudes is robust and easily understood in the case of our idealized GCM, but simulations with comprehensive GCMs suggest that the land-ocean warming contrast is not confined to the lower latitudes (e.g., Sutton et al., 2007). Land surfaces and moisture convergence regimes in Earth's extratropics are more diverse than in our idealized GCM, and relatively arid regions occur there regionally and seasonally [for example, mean surface relative humidity in summer over Mongolia and neighboring parts of Russia is substantially lower than over ocean regions at similar latitudes (Dai, 2006)]. Also, midlatitude soil drying under global warming may occur because of decreased and earlier snowmelts (Rowell and Jones, 2006), and such behavior is not found in our idealized GCM which has no seasonal cycle or snow or ice. Land-ocean contrasts in heat capacity may also be important for the warming contrast at midlatitudes where the seasonal cycle is strong, though we leave this as a topic for future work.

To examine the effect of limited moisture availability at higher latitudes in the idealized GCM, we prescribe different evaporative fractions in a series of simulations while holding the longwave absorber parameter fixed at $\alpha = 1$ (as for the simulations over a subtropical zonal land band discussed in Section 2.4.3). A temperature contrast does indeed develop as the evaporative fraction β is reduced, with $T_\mathrm{L} - T_\mathrm{O} \simeq 1.5\,\mathrm{K}$ for $\beta = 0.1$ (Fig. 2-11b), although this is substantially smaller than the 6 K difference for the subtropical land band at the same value of β. The theory roughly predicts the magnitude of the temperature contrast (Fig. 2-11b) and is approximately as accurate, in a fractional sense, as for the subtropical land band simulations (cf. Fig. 2-11a). The reduced temperature contrast relative to lower latitudes is due to both lower temperatures and higher relative humidities further poleward (cf. Fig. 2-2). According to the theory, these effects are of similar importance in contributing to the reduced land-ocean temperature contrast at higher latitudes.

2.5.2 Midlatitude theory

One of the assumptions used in the theory, that the land-ocean temperature contrast vanishes aloft, is found to be adequate in the simulations with a midlatitude land band. But the extratropical lapse rates are made more stable than moist adiabatic by large-scale eddies, and so it is somewhat surprising that the theory based on moist adiabatic lapse rates gives a reasonable estimate of the magnitude of the warming contrast at midlatitudes. The fact that land-ocean temperature contrasts are sensitive to lower-tropospheric lapse rates (cf. Fig. 2-1) may be a contributing factor, since simulated extratropical lapse rates are closest to moist adiabatic in the lower troposphere (Schneider and O'Gorman, 2008).

There are theories of the extratropical static stability that take account of moisture and large-scale eddies (Juckes, 2000; Frierson, 2008; Schneider and O'Gorman, 2008; O'Gorman, 2011). The results of O'Gorman (2011) suggest that the dry static stability may be written as the sum of an effective static stability and a contribution from moisture that is a fraction (roughly 0.6) of the dry static stability along a moist adiabat. If this contribution from moisture is the primary difference in the dry static stability over land and ocean, then the surface warming contrast theory is easily modified for the extratropics by multiplying the predicted warming contrast by roughly a factor of 0.6 (Fig. 2-11b, dotted line).

Alternatively, the theory of Juckes (2000) suggests that the vertical gradient in equivalent potential temperature is proportional to the meridional temperature gradient. If this relationship is taken to hold separately over land and ocean, then the predicted surface warming contrast should be unchanged by extratropical eddies if meridional temperature gradients are the same over land and ocean [and similarly for the formulation of Frierson (2008) and Frierson and Davis (2011) but with meridional equivalent potential temperature gradients].

The midlatitude temperature contrasts shown in Figure 2-11b are consistent with a modification to the predicted surface warming contrast by an order one factor, and the effective static stability version of the theory gives reasonable agreement with the simulations, but clearly further work is needed to evaluate these theories for the extratropical surface warming contrast.

2.5.3 Meridional land band

We examine the land-ocean warming contrast over all latitudes simultaneously using two simulations ($\alpha = 1$ and $\alpha = 1.5$) with a meridional land band from 0° to 60°E in longitude (cf. Fig. 2-4d). Land temperatures at each latitude are obtained by averaging in time and zonally from 0° to 60°E, while ocean temperatures are averaged in time and zonally from 180°E to 240°E. Local minima occur near the equator in both the land-ocean temperature difference (not shown) and the amplification factor (Fig. 2-12). These equatorial minima coincide with deep convection, moisture flux convergence, and relatively high levels of soil moisture. Maxima in the amplification factor occur at ∼15° north and south, coincident with the descending branches of the Hadley cells. The land-ocean warming contrast decreases sharply in midlatitudes; according to the theory, this reflects both the poleward increase in relative humidity over land and the poleward decrease in temperature (Fig. 2-5). The land and ocean temperatures are almost equal poleward of 50° latitude. By comparison, mean precipitation exceeds mean evaporation over ocean poleward of approximately 38° latitude.

The theoretical amplification factor is less accurate for the meridional band simulations than for the subtropical zonal land band or continent, particularly at subtropical latitudes (Fig. 2-12). The reduced accuracy is partly due to the inadequacy of the approximation of moist adiabatic lapse rates, but it may also relate to stationary waves excited by the land band and the lack of an ocean-only Southern Hemisphere to compare with. The amplification factor calculated from theory at constant surface relative humidities seems to be reasonably accurate at all latitudes (Fig. 2-12) but this results from a compensation of the effects of neglecting changes in relative humidity and the inaccuracy of the assumption of moist adiabatic lapse rates over land. The results from the meridional land band simulations suggest that further work is needed to better quantify the factors affecting the accuracy of the theory, and to determine how best to compare land and ocean temperatures in the same hemisphere.

2.5.4 Polar amplification

Given the abundance of land at northern high latitudes, it is difficult to cleanly distinguish in observations or comprehensive climate model simulations between polar amplification of temperature changes and land-ocean warming contrast. A number of processes contribute to polar amplification, including ice-albedo feedback, changes in ocean circulation, polar cloud cover, and atmospheric heat transport (Holland and Bitz, 2003; Hall, 2004; Bony et al., 2006). Although the idealized GCM does not include many of these processes, it still shows a polar amplification effect under climate change (O'Gorman and Schneider, 2008a) [see also Alexeev et al. (2005)]. The meridional land band simulations presented here show only a negligible land-ocean warming contrast beyond 50° latitude (Fig. 2-12), which implies that the processes involved in establishing a land-ocean temperature contrast at low to midlatitudes are distinct from those responsible for polar amplification in this GCM. We do note, however, that other work suggests radiative feedbacks associated with changing water vapor concentrations may be an important component of both polar amplification and of land-ocean contrasts (Dommenget and Flöter, 2011), and land-ocean radiative contrasts are discussed in the next section.

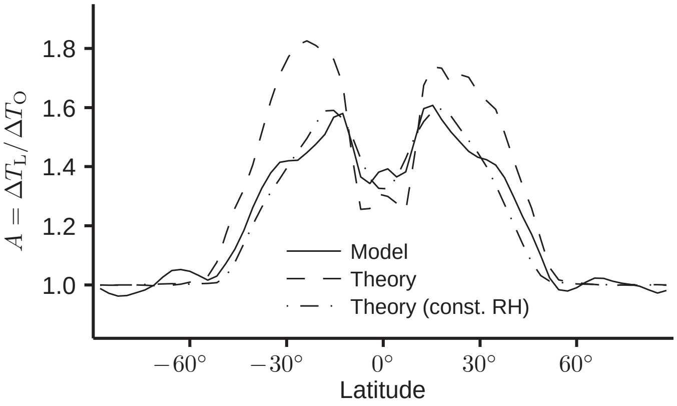

Figure 2-12: The amplification factor vs. latitude for warming between two simulations ($\alpha = 1$ and $\alpha = 1.5$) with a meridional land band from 0°E to 60°E (solid line). The dashed line is the estimate of the amplification factor from theory, and the dashed-dotted line is the estimate from theory neglecting changes in relative humidity. Interhemispheric asymmetry is indicative of sampling error.

2.6 Land-ocean radiative contrasts

The simulations so far have included only a land-ocean contrast in surface hydrology. Albedo contrasts or radiative feedbacks from the contrast in humidity could also affect the land-ocean warming contrast, potentially in a manner that is not captured by the theory presented earlier. For instance, decreases in the longwave optical thickness in response to lower evaporative fraction could tend to lower the surface temperature over land (e.g., Molnar and Emanuel, 1999) and reduce the land-ocean temperature contrast.

2.6.1 Water vapor radiative feedbacks

To assess the effect of longwave radiative feedbacks on the land-ocean temperature contrast, an alternative radiation scheme is used in which the longwave optical thickness depends on humidity according to

$$\frac{d\tau}{d\sigma} = a\mu + bq, \tag{2.4}$$

where τ is the longwave optical thickness (set to zero at the top of the atmosphere), $a = 0.8678$ and $b = 1997.9$ are non-dimensional constants, and q is the specific humidity [this formulation is similar to that of Merlis and Schneider (2010) except that the longwave optical thickness in their study depends on column water vapor rather than specific humidity]. To facilitate comparison between simulations with the different radiation schemes, the values of a and b were chosen by fitting (2.4) with $\mu = 1$ to the longwave optical thickness averaged from 20°N to 40°N for a reference ($\alpha = 1$) aquaplanet simulation with the default radiation scheme. With this choice of parameters, water vapor is the dominant longwave absorber at all latitudes for the reference value of $\mu = 1$. Atmospheric shortwave heating is prescribed as in the default radiation scheme. Feedbacks associated with shortwave absorption by water vapor are not considered here and may also influence the land-ocean temperature contrast.

For the subtropical zonal land band (20°N to 40°N), we vary the radiative parameter μ over the range $0.4 \leq \mu \leq 2$ as a representation of the longwave-radiative effect of changes in greenhouse gases other than water vapor[6]. We also consider simulations with specified evaporative fraction β over the range $0.1 \leq \beta \leq 0.9$ and with $\mu = 1$. The results from both sets of simulations are qualitatively similar to those performed using the default radiation scheme (not shown). The land-ocean temperature contrast is slightly higher than for the default radiation scheme (by approximately 2 K for $\alpha = 4$ in the dynamic soil moisture simulations, and by approximately 0.5K at $\beta = 0.5$ in the prescribed evaporative fraction simulations). For the midlatitude zonal land band (45°N to 65°N), we consider simulations with prescribed evaporative fractions over the same parameter range as for the subtropical land band. The land-ocean temperature contrast is roughly equal to the contrast in the default radiation scheme, and is relatively small compared with lower latitudes. For both subtropical and midlatitude land simulations, the theoretical estimates are of a similar or better accuracy when compared with the estimates for the simulations with the default radiation scheme.

---

[6] Simulations are performed with μ values of 0.4,0.7,1,1.5, and 2.

There are only modest land-ocean temperature differences associated with water vapor radiative contrasts in our simulations. However, the study of Dommenget and Flöter (2011), using a globally-resolved energy balance model, suggests a greater role for water vapor radiative feedbacks in setting the land-ocean warming contrast than is found here. The idealized nature of the gray radiation scheme used here precludes us from making any definitive conclusions on this issue based on our simulations.

2.6.2 Albedo contrast

The importance of land-ocean albedo contrast in determining the land-ocean warming contrast is assessed using a series of simulations in which the ocean surface albedo is set to a smaller value of 0.20 and the land surface albedo remains at 0.38 (the albedo is 0.38 over both land and ocean in our other simulations). Note that cloud, snow, and ice albedo effects are not included in the idealized GCM, and the surface albedo values used are not intended to be realistic. The simulations are with a subtropical zonal land band (20°N to 40°N) and use the default radiation scheme in which the longwave absorber is varied over the range $0.2 \leq \alpha \leq 6$.

The simulated climates are warmer than those presented in Section 2.4 because of the reduced ocean albedo. The land-ocean temperature contrasts are also affected by the albedo contrast, and the land is colder than the ocean for the $\alpha = 0.2$ and $\alpha = 0.4$ simulations, despite the lower surface air relative humidity over land. The theory consistently overestimates land temperatures in the simulations with an albedo contrast (e.g., by $\sim$7K at $\alpha = 1$), although it still performs reasonably well in estimating the amplification factors (Fig. 2-13) because the error in estimating the land temperature does not vary strongly with climate. The amplification factors in the albedo contrast simulations are larger compared to the simulations presented in Section 2.4, e.g. by approximately 0.2 at an ocean surface air temperature of 305K (cf. Fig. 3.2).

The overestimation of land temperatures in the simulations with an albedo contrast is primarily related to temperatures over land and ocean not converging aloft. (As a result, the generalized theory discussed at the end of Section 2.2 in which lapse rates can deviate from moist adiabatic is not helpful; the surface air equivalent

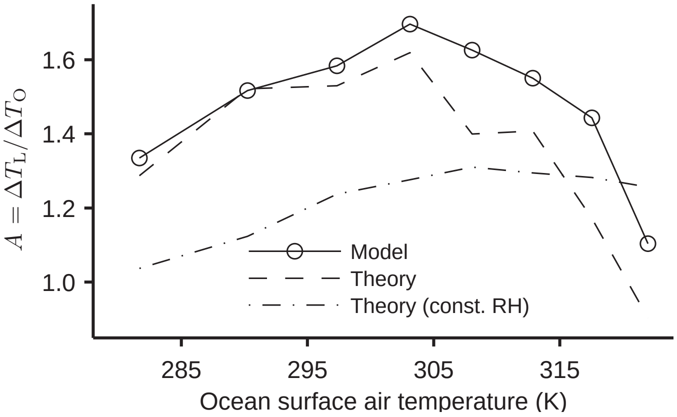

Figure 2-13: The amplification factor vs. ocean surface air temperature in land-ocean albedo contrast simulations with a subtropical zonal land band from 20°N to 40°N (solid line), and from theory (dashed line). The ocean albedo is 0.20 and the land albedo has the default value of 0.38. The amplification factors are calculated as in Fig. 2-7.

potential temperature is higher over ocean than land, with the difference increasing from 12K in the coldest simulation to 44K in the warmest simulation.) The assumption made by Joshi et al. (2008) of a fixed land-ocean temperature difference at a certain upper level may be more appropriate here, but modifying the theory to use it would require additional assumptions regarding the choice of upper level. Given that the amplification factors from the theory are reasonably accurate, the simplest approach seems to be to use the theory to estimate the amplification factors, with the understanding that the land temperatures (as opposed to their changes) may be overestimated because of albedo contrast.

2.7 Surface air versus surface skin temperature

The results discussed so far are for surface air temperatures, but surface skin temperatures may not respond in the same way to climate change. Figure 2-14 shows that surface skin temperatures are generally larger than surface air temperatures in the subtropical zonal land band simulations (with the default radiation scheme and albedo values). The amplification factors for the surface air and surface skin temperatures are similar, but with somewhat larger amplification factors for surface skin

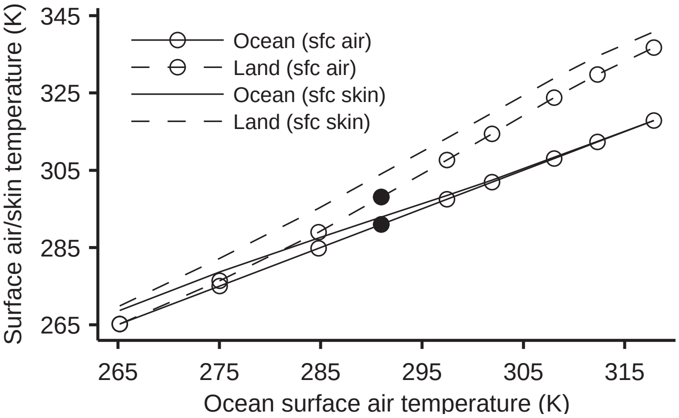

Figure 2-14: Surface air temperature over ocean (solid line with circles) and land (dashed line with circles), along with surface skin temperature of the ocean (solid line) and land (dashed line) vs. ocean surface air temperature for simulations with a subtropical zonal land band from 20°N to 40°N. The same spatial and temporal averaging is used for the skin temperatures as for the surface air temperatures.

temperatures below $\simeq 305\,\mathrm{K}$, as may be inferred from Figure 2-14. For example, for an ocean surface air temperature of 285K, the amplification factors based on surface skin and surface air temperatures are 1.67 and 1.48, respectively.

The air-surface temperature disequilibrium (the difference between the surface air and surface skin temperatures) decreases as the climate warms and does so more strongly over ocean than over land (Fig. 2-14). Changes in the air-surface temperature disequilibrium may be understood in terms of the surface energy budget, since the surface energy fluxes (particularly the dry sensible heat flux) are strongly coupled to it. As the climate warms, evaporative cooling of the surface generally increases due to the dependence of the saturation vapor pressure on temperature. The increased evaporative cooling is partially balanced by a reduction in dry sensible cooling, as reflected in the decrease in air-surface temperature disequilibrium, in order to maintain the surface energy balance. Increases in evaporative cooling are smaller over land than ocean and are inhibited by the land becoming increasingly arid, explaining why the air-surface temperature disequilibrium does not decrease to the same extent over land, and why amplification factors are somewhat larger for surface skin temperatures.

The air-surface temperature disequilibrium may be large for very arid land regions in a given climate (e.g., Pierrehumbert, 1995), but this does not mean it will necessarily change greatly in these regions as the climate changes (as compared to the land-ocean surface warming contrast). For example, the amplification factors based on surface air and surface skin temperatures are similar in our warm simulations in which the land is very arid. Rather, we may expect these amplification factors to differ most in regions with substantial changes in aridity of the land surface as the climate changes.

As discussed in the introduction, it is difficult to build a theory of the surface warming contrast based solely on the surface energy budget because changes in both the surface temperature and air-surface temperature disequilibrium may play an important role in the adjustment of the surface energy budget over land and ocean. The theory presented in Section 2.2 based on convective quasi-equilibrium gives an independent estimate of the land-ocean warming contrast in surface air temperatures, which may be combined with the constraint of the surface energy budget. As a result, we argue that surface skin warming contrasts may be best understood based on the theory for the surface air warming contrasts and an understanding of changes in the surface energy budget.

Global observational datasets often provide skin temperatures over ocean (sea surface temperatures) and surface air temperatures over land. For our simulations, the amplification factors using land surface air temperatures and ocean surface skin temperatures are similar to those calculated solely from surface skin temperatures (and larger than those calculated solely from surface air temperatures). Since our theory is most appropriate for surface air temperatures, it may understimate amplification factors calculated from temperature anomalies in these mixed observational datasets.

2.8 Conclusions

Based on the idea that differential changes in lapse rates over land and ocean constrain the surface warming contrast (Joshi et al., 2008), we have developed a simple theory that relates the land surface air temperature and the land-ocean warming contrast to the ocean temperature and the surface relative humidities over land and ocean. The theory amounts to setting the surface air equivalent potential temperature to be equal over land and ocean. For constant relative humidities, the theory implies that the amplification factor has a maximum at ~293 K, a property that follows from the temperature dependence of the saturated moist adiabatic lapse rate. Thus, if two land regions at different latitudes are equally arid, it will be the region whose surface air temperature is closest to 293K that exhibits the largest warming contrast according to the theory. Changes in surface relative humidities also play an important role in determining the magnitude of the warming contrast; the theory yields expressions for the additive contributions to the amplification factor from changes in surface relative humidity over land and ocean.

We have applied the theory to simulations with a wide range of climates and land configurations in an idealized GCM. The warming contrast in the equilibrium response of the GCM is primarily confined to low and middle latitudes. For simulations with a subtropical zonal land band forced by changes in longwave optical thickness, the amplification factor is roughly 1.4, which is comparable to low-latitude amplification factors found in observations and simulations with comprehensive GCMs. For a subtropical continent of finite zonal extent, more analogous to what is found on Earth, the magnitude of the land-ocean contrast is reduced compared with the zonal land band as a result of higher relative humidities over the continent compared with the zonal band.

For the subtropical zonal land band and the subtropical continent, the theory closely matches the simulated temperature contrasts over the full range of simulations. It has a similar level of accuracy in an alternative set of simulations in which land aridity is systematically varied by specifying the evaporative fraction, but it performs less well when applied to simulations with a meridional land band, although the latitudinal dependence of the warming contrast is still captured.

Atmospheric moisture convergence at middle and high latitudes maintains the soil moisture at close to the field capacity, and there is little warming contrast in the simulations at these latitudes. A midlatitude warming contrast may be induced by directly specifying a low evaporative fraction, and the theory gives a rough estimate of its magnitude. According to the theory, the midlatitude warming contrast is relatively small because of higher relative humidities and lower surface temperatures compared to lower latitudes. The midlatitude stratification is generally more stable than moist adiabatic because of large-scale eddies, implying that the theory is not strictly applicable. We have discussed the extension of the theory to the extratropical regime based on theories of the moist extratropical stratification. The extended theories suggest that the magnitude of the implied warming contrast may be changed by only an order one factor from that given by the convective quasi-equilibrium theory. Further work is needed to evaluate these extended theories for the extratropical warming contrast.

The simulated warming contrast is found to be slightly higher for the subtropical zonal land band when a radiation scheme that allows for water vapor radiative feedbacks is used (the midlatitude warming contrast is unchanged), and the theory is still adequate for these simulations. But the theory consistently overestimates the land temperatures when the albedo over ocean is set to be lower than over land. The amplification factor from the theory is still reasonably accurate in the presence of the albedo contrast because the land temperatures are overestimated by roughly the same amount in different climates.

The simple theory is successful in capturing the main features of the land-ocean warming contrast resulting from changes in moisture availability and a proxy for greenhouse gases in the idealized GCM simulations. Our results and those of previous studies also point to some limitations of the theory. In our simulations, deviations of the lapse rates over land from moist adiabatic reduce the accuracy of the theory. This is perhaps not very surprising given that convective quasi-equilibrium should not be expected to hold even at low latitudes when, for example, moist convection is infrequent or in large-scale conditions conducive to the formation of inversion layers. Also, even if the theory is adequate for estimating the amplification factors with an invariant albedo contrast, it is not expected to capture the effect of different changes in albedo over land and ocean. Lastly, previous work indicates that land warming is more sensitive to ocean warming than vice versa (as discussed in the introduction), but to the extent that the response of surface relative humidity is similar, the theory gives the same amplification factor regardless of where the forcing is imposed.

The amplification factors in the simulations are found to be different depending on whether surface air or skin temperatures are considered (or a mixture of the two as in some observational datasets). Given that the difference between surface air and surface skin temperatures is controlled by the surface energy budget, we argue that an understanding of surface skin warming contrasts for a given level of land aridity follows from a combination of the theory for surface air warming contrasts and the additional constraints of the surface energy balances over land and ocean.

The theory and simulations presented here are expected to be useful in analyzing the factors contributing to land-ocean warming contrasts in observations and in simulations with more comprehensive climate models (see next chapter). The theory is likely to be most useful at low latitudes where the effects of moisture availability are strongest and the assumptions underlying the theory are most appropriate. Differences in roughness length, cloud cover, diurnal cycle, and seasonal cycle between land and ocean regions were not accounted for in our idealized simulations. The influence of these factors on the warming contrast could also be examined in an idealized setting. Further work is also needed to examine the sensitivity of our results to the choice of convective parameterization and land surface scheme. Lastly, as discussed in the introduction, the warming contrast in transient simulations is higher than in equilibrium simulations, and it would be interesting to examine how this relates to surface humidity changes in light of the theory presented here.

Chapter 3

Warming contrast: CMIP5 simulations and observations

©American Geophysical Union 2013[1]

3.1 Introduction

As discussed in the previous chapter, the land-ocean warming contrast is a fundamental feature of the climate system which is evident in observed surface warming over the last century (e.g., Lambert and Chiang, 2007) and in simulations of climate change (e.g., Sutton et al., 2007). Observations and a variety of general circulation model (GCM) simulations show global amplification factors[2] of approximately 1.5, with significant variations in latitude (e.g., Sutton et al., 2007; Drost et al., 2012; Joshi et al., 2013). This enhanced land warming relative to the ocean occurs in both transient and equilibrium simulations, showing that the land-ocean warming contrast does not simply result from the different effective heat capacities of land and ocean regions (Sutton et al., 2007).

The land-ocean warming contrast may influence the response of the atmospheric

---

[1] This chapter is a partial reproduction of Byrne and O'Gorman (2013b). We have made minor changes to the text and have included an analysis of the warming contrast in observations (Section 3.4).

[2] As in the previous chapter, the amplification factor is defined as $A = \delta T_{\mathrm{L}}/\delta T_{\mathrm{O}}$, where δT_{L} and δT_{O} are the changes in surface-air temperatures over land and ocean, respectively.

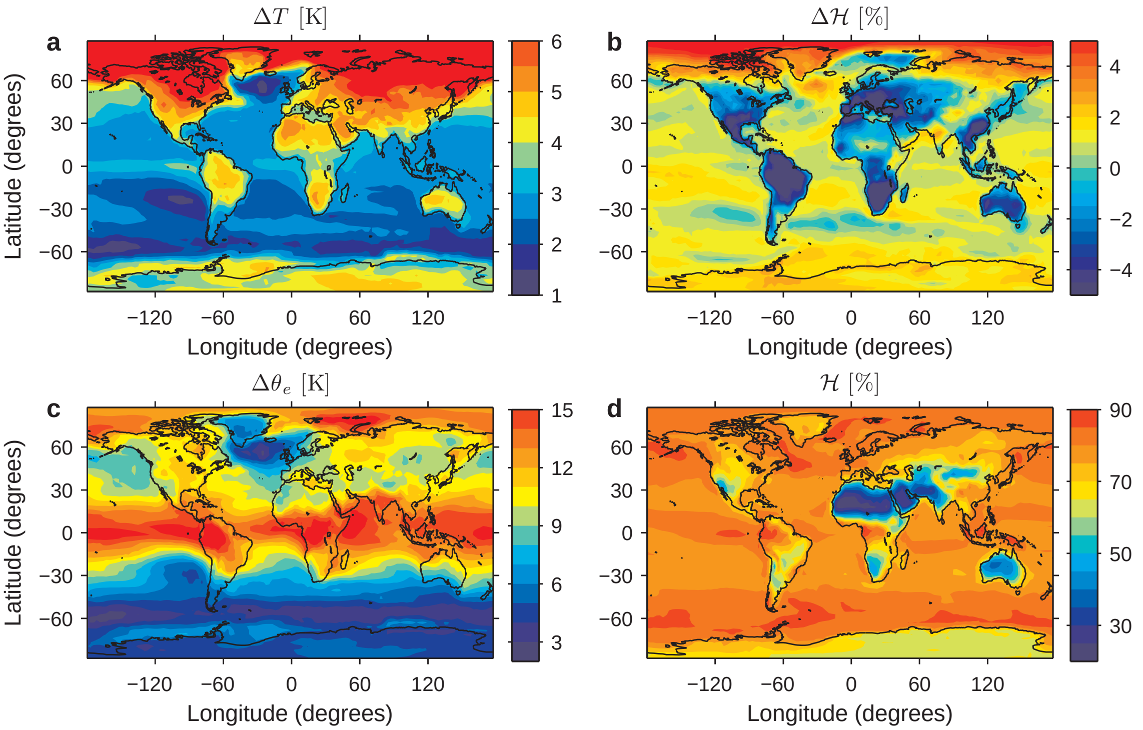

Figure 3-1: Multimodel-median changes in surface air (a) temperature, (b) relative humidity, and (c) equivalent potential temperature between the historical (1975-2004) and RCP8.5 (2070-2099) simulations. Panel (d) shows the multimodel-median surface air relative humidity in the historical simulation (1975-2004). Each field is linearly interpolated to a common grid prior to calculation of the multimodel median. Absolute rather than fractional changes in relative humidity are shown in (b).

general circulation to climate change (Bayr and Dommenget, 2013), and it is also important for regional impacts of climate change. However, the magnitude of the land-ocean warming contrast varies substantially between climate models (e.g., Joshi et al., 2013) and between different periods of the observed temperature record. Furthermore, although heat stress depends on both temperature and humidity, it is not clear to what extent the land-ocean warming contrast is linked to the land-ocean contrast in changes in surface relative humidity that is also found in simulations of climate change (O'Gorman and Muller, 2010).

Building on work by Joshi et al. (2008), Byrne and O'Gorman (2013a) proposed a convective quasi-equilibrium theory for the magnitude of the warming contrast. This theory relates surface air temperatures and relative humidities over land to those over ocean based on assumptions of moist adiabatic lapse rates and equal temperatures sufficiently far aloft over land and ocean [Joshi et al. (2008) made slightly different assumptions of no warming contrast aloft and lapse rates equal to humidity-weighted averages of dry and saturated moist adiabatic lapse rates]. When applied to simulations with an idealized GCM, the theory captured the warming contrast over a wide range of climates and for a range of continental configurations, although its accuracy is diminished by land-ocean contrasts in surface albedo, and its theoretical basis is only valid in the tropics.

Here, we apply a generalized version of the theory to simulations from the Coupled Model Intercomparison Project 5 (CMIP5) and assess the extent to which it links the simulated temperature and humidity changes over land and ocean. We begin by discussing the land-ocean contrasts in changes in temperature and relative humidity in the simulations (Section 3.2). We then apply the theory and use it to characterize the contributions to the land-ocean warming contrast in the tropics, and we discuss possible implications for changes in heat stress over land (Section 3.3). The observed warming contrast is then discussed, and the apparent lack of a warming contrast over the early part of the 20th century is investigated (Section 3.4). Lastly, we briefly summarize our results and their implications (Section 3.5).

3.2 Land-ocean contrasts in CMIP5 simulations

We consider simulations with 27 models from CMIP5[3]. Climate change is defined here as the difference between thirty-year time averages in the historical simulations (1975-2004; referred to as the control climate) and the RCP8.5 simulations (2070-2099) using the r1i1p1 ensemble member in each case (Taylor et al., 2012). We use monthly-mean surface air temperatures and monthly-mean surface air relative humidities. Relative humidities in the CMIP5 archive are reported with respect to

---

[3] The models used are ACCESS1-0, ACCESS1-3, BCC-CSM1-1, BCC-CSM1-1-M, CanESM2, CCSM4, CESM1-BGC, CESM1-CAM5, CNRM-CM5, CSIRO-Mk3-6-0, FGOALS-s2, GFDL-CM3, GFDL-ESM2M, GISS-E2-H, GISS-E2-R, HadGEM2-AO, HadGEM2-CC, HadGEM2-ES, INMCM4, IPSL-CM5A-LR, IPSL-CM5A-MR, IPSL-CM5B-LR, MIROC5, MIROC-ESM, MRI-CGCM3, NorESM1-ME, and NorESM1-M. Other models were excluded because of lack of available data at the time when the analysis was conducted.

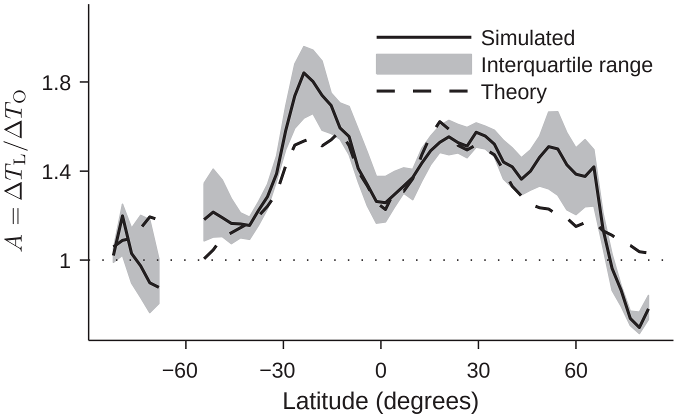

Figure 3-2: The land-ocean amplification factor, $A = \Delta T_{\mathrm{L}}/\Delta T_{\mathrm{O}}$, vs latitude in the multimodel median (solid line), its interquartile range (gray shading), and the corresponding estimate from theory (dashed line).

liquid water for temperatures above 0°C and with respect to ice for temperatures below 0°C. To be consistent with the formulation of equivalent potential temperature we will later use (which does not consider the ice phase of water), we approximately adjust the relative humidities to be always with respect to liquid water using the monthly-mean temperatures.

The CMIP5 simulations show substantially greater warming over land than ocean (Fig. 3-1a). To quantify the dependence of the warming contrast on latitude, we calculate the multimodel-median amplification factor based on zonal- and time-mean temperatures (Fig. 3-2). The amplification factor is above unity at almost all latitudes, but it has a local minimum near the equator, maxima in the subtropics, and a general decrease moving from the subtropics to the poles. This variation of the warming contrast with latitude is qualitatively similar to results from the earlier CMIP3 simulations (Sutton et al., 2007; Boer, 2011) and from idealized GCM simulations with a meridional land band (Byrne and O'Gorman, 2013a, see previous chapter).

Intermodel scatter in the amplification factor is substantial at many latitudes (Fig. 3-2 and Fig. 3-3a). Averaging over the tropics, defined here as 20°S to 20°N, the model amplification factors range from 1.31 to 1.64 (Fig. 3-4a). This represents a large discrepancy between models, especially in the context of the regional and societal impacts of future climate change. By repeating the analysis using different

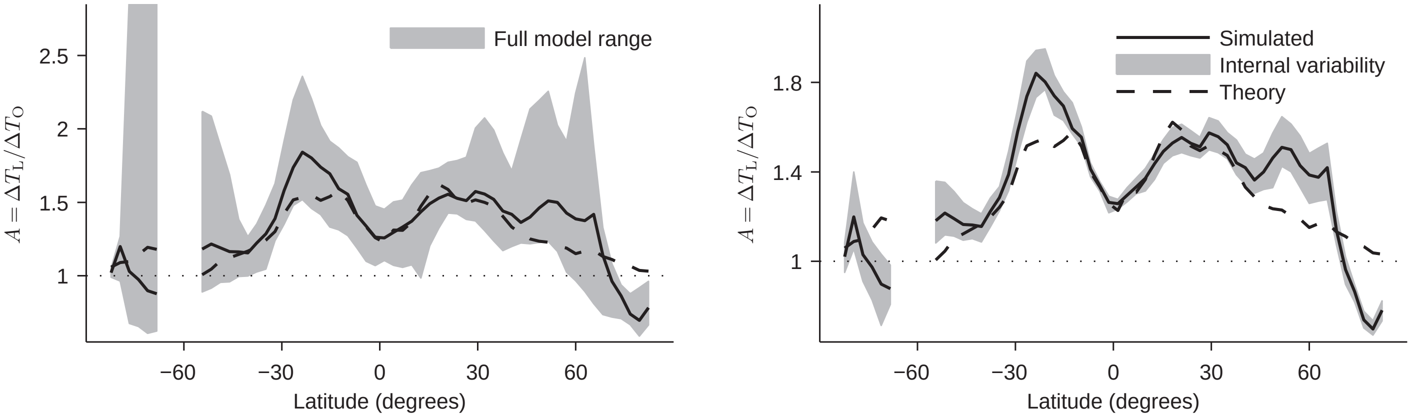

(a) (b)

Figure 3-3: As in Fig. 3-2 but the gray shading shows different quantities instead of the interquartile range of the models. In (a), the gray shading shows the full model range. In (b), the gray shading shows a measure of the effect of internal variability on the multimodel median at each latitude. The internal variability in the simulated amplification factor is estimated by first dividing the 30-year averaging periods in the historical and RCP8.5 simulations into three decades each, i.e. for the historical simulation the averaging periods are 1975-84, 1985-94, and 1995-2004 (similarly for RCP8.5). The land and ocean temperature changes between the historical and RCP8.5 simulations for every combination of decades (nine combinations in total) are then used to recalculate the amplification factor. The upper bound of the gray shading denotes the multimodel median of the maximum amplification factor obtained from this analysis at each latitude, and the lower bound is the multimodel median of the minimum values.

10-year averaging periods, the effect of internal variability is estimated to be small compared to the intermodel scatter, as shown for the multimodel median in Figure 3-3b.

There is also a strong land-ocean contrast in the changes in surface relative humidity (Fig. 3-1b), and a land-ocean contrast in climatological-mean surface relative humidity at low latitudes (Fig. 3-1d). Surface relative humidity shows increases over ocean and stronger decreases over land, as was also found in earlier simulations (O'Gorman and Muller, 2010; Fasullo, 2010; Dommenget and Flöter, 2011). Weak increases in surface relative humidity over ocean are consistent with what is expected from surface energy balance considerations and the dependence of evaporation on surface relative humidity (Held and Soden, 2000; Schneider et al., 2010). However, such arguments do not hold over land where there is limited surface water availability. The

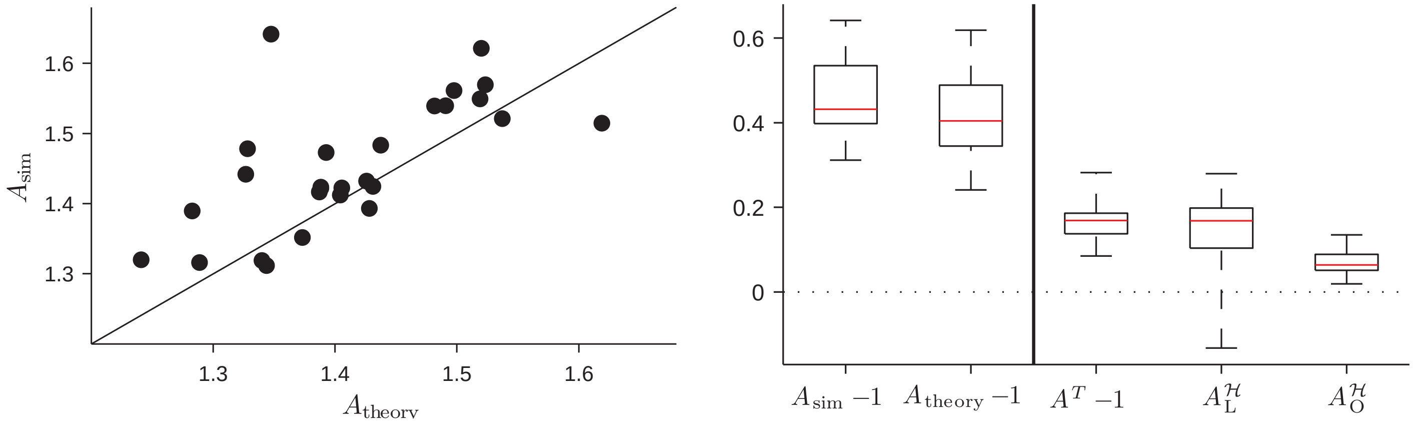

(a)

(b)

Figure 3-4: (a) Simulated tropical amplification factors (A_{sim}) vs their theoretical estimates (A_{theory}) for different climate models. The solid line is the one-to-one line. (b) Boxplots showing the tropical amplification factors, their estimates from theory, and the contributions to these estimates as defined by (3.2). The whiskers show the full model range, the boxes show the 1st and 3rd quartiles, and the central line shows the median. All amplification factors and contributions in this figure have been averaged between 20°S and 20°N.

decrease in land surface relative humidity is partly coupled to the land-ocean warming contrast through the role of the ocean as a source of water vapor transported over land (Rowell and Jones, 2006; O'Gorman and Muller, 2010; Simmons et al., 2010), but it is also related to changes in factors that affect evapotranspiration such as changes in stomatal conductance due to increases in atmospheric CO_2 concentrations (e.g., Dong et al., 2009). The processes controlling land relative humidity will be investigated in Chapter 4.

In the next section, we show how atmospheric dynamical constraints link the tropical land-ocean warming contrast to the surface relative humidities and their changes, both for the multimodel median and for intermodel differences.

3.3 Application of theory

Buliding on the results of Joshi et al. (2008), the theory developed and applied to idealized GCM simulations by Byrne and O'Gorman (2013a) assumes that (a) temperatures in the tropical free troposphere are equal over land and ocean (consistent

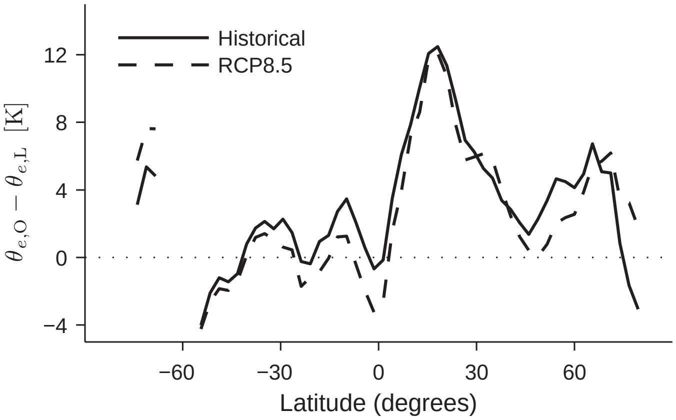

Figure 3-5: The multimodel-median difference between surface air equivalent potential temperatures over land and ocean vs latitude for the historical (1975-2004) and RCP8.5 (2070-2099) simulations. The equivalent potential temperatures are evaluated based on zonal- and time-mean temperatures and relative humidities to be consistent with how the theory is evaluated.

with the weak temperature gradient approximation; Sobel and Bretherton, 2000), and (b) that tropical lapse rates are moist adiabatic in the mean over land and ocean, with the result that surface air equivalent potential temperatures are equal over land and ocean. Byrne and O'Gorman (2013a) briefly discussed a generalized theory, also consistent with convective quasi-equilibrium (e.g., Arakawa and Schubert, 1974; Emanuel, 2007), that relaxes the assumption of moist adiabatic lapse rates and instead assumes that the degrees of departure of the land and ocean lapse rates from moist adiabats remain constant as climate changes. This generalized theory is formulated by assuming that changes in equivalent potential temperature ($\delta\theta_e$), rather than the equivalent potential temperatures themselves, are equal over land and ocean:

$$\delta\theta_{e,\mathrm{L}} = \delta\theta_{e,\mathrm{O}}. \tag{3.1}$$

We use the generalized theory here because it is found to be more accurate when applied to climate change in the CMIP5 simulations; the equivalent potential temperature in the control climate is as much as 12K higher over ocean than land in the zonal and time mean (Fig. 3-5).

We evaluate the equivalent potential temperature based on surface air temperatures and relative humidities (with respect to liquid water) using Eq. 43 from Bolton (1980). As shown in Fig. 3-1c, the changes in equivalent potential temperature are quite zonally uniform and vary on relatively large spatial scales. Consistent with (3.1), there is little land-ocean contrast in the changes in equivalent potential temperature, unlike the changes in temperature (Fig. 3-1a) and relative humidity (Fig. 3-1b), both of which vary sharply near coastlines. Because equivalent potential temperature is a nonlinear function of temperature and humidity, (3.1) provides a link between the changes in temperature and humidity and their values in the control climate.

3.3.1 Estimate of amplification factor

Equation (3.1) is solved numerically at each latitude to estimate the land warming and amplification factor under the RCP8.5 scenario. The primary inputs to the calculation are the control-climate temperatures and relative humidities and the changes in relative humidities and ocean temperature. Zonal- and time-mean temperatures and relative humidities are used, but, to allow for seasonal effects, we estimate the land temperature in each of the 12 calendar months individually prior to taking an annual average. Zonal- and time-mean surface pressures are also used in the calculation of the equivalent potential temperatures.

The theory captures the magnitude and meridional structure of the multimodel-median amplification factor from the equator to approximately 40° latitude north and south, athough there is some underestimation in the southern subtropics (Fig. 3-2). According to the theory, the local minimum near the equator is associated with high land surface relative humidity near the ascending branches of the Hadley cells, and the subtropical maxima are associated with low land relative humidity over the arid subtropical land-masses. The theory accurately estimates the magnitude of the amplification factor averaged with area weighting over the tropics (20°S to 20°N); the multimodel-median value for the simulations is 1.43 compared with the corresponding estimate from theory of 1.40. The theory also captures the tropical amplification factors in individual models (Fig. 3-4a), with a correlation coefficient across models between the simulated and theoretical values of 0.67. The ability of the

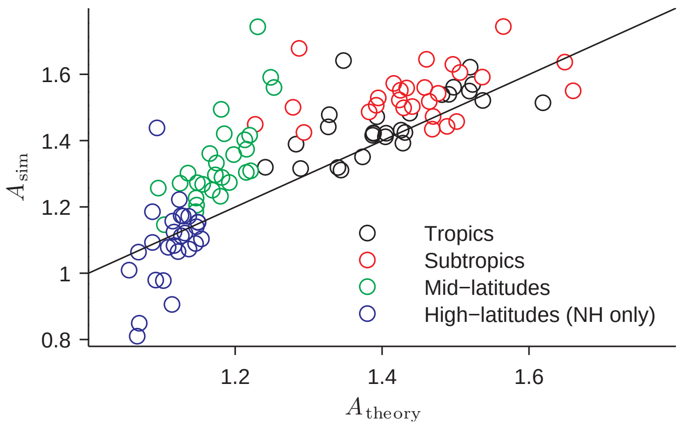

Figure 3-6: As in Fig. 3-4a but averaged over different latitude bands. The tropics (black symbols) are 20°S to 20°N. The subtropics (red symbols) are 20° to 40° in both hemispheres. The mid-latitudes (green symbols) are 40° to 60° in both hemispheres. The high-latitudes (blue symbols) are 60° to 90° in the Northern Hemisphere only because the amplification factors are noisy at these latitudes in the Southern Hemisphere for some of the models.

theory to capture a considerable amount of the intermodel scatter provides further support for its validity in the tropics.

The theory implies that there should be a general decrease in amplification factor moving from the subtropics to the poles associated with both decreasing temperature and increasing surface relative humidity over land (Byrne and O'Gorman, 2013a). However, the theory is not directly applicable to the extratropics because mean extratropical lapse rates are not moist adiabatic and extratropical horizontal temperature gradients aloft need not be weak. Furthermore, changes in surface albedo may be more important than moisture effects for the extratropical land-ocean warming contrast. Consistent with these expectations, greater deviations from the theory are found in the mid- and high-latitudes compared with the tropics (Fig. 3-2 and Fig. 3-6). Possible extensions of the theory to the extratropics are discussed in the previous chapter [e.g., using the effective static stability of O'Gorman (2011)], but here we focus on the tropics where the simplest form of the theory is expected to hold.

3.3.2 Contributions to the tropical amplification factor

We next assess the contributions to the tropical land-ocean warming contrast when changes in relative humidity and ocean temperature are taken as given. Following Byrne and O'Gorman (2013a), the amplification factor from theory is decomposed into different components as

$$\begin{aligned} A_{\text{theory}} &= A^T + A^{\mathcal{H}}_{\text{L}} + A^{\mathcal{H}}_{\text{O}} \\ &= \frac{\partial T_L}{\partial T_O} + \frac{\partial T_L}{\partial \mathcal{H}_L}\frac{d\mathcal{H}_L}{dT_O} + \frac{\partial T_L}{\partial \mathcal{H}_O}\frac{d\mathcal{H}_O}{dT_O}, \end{aligned} \tag{3.2}$$

where A^T is the contribution to the amplification factor that arises from changes in ocean temperature alone (holding land and ocean relative humidities fixed), $A^{\mathcal{H}}_{\text{L}}$ is the contribution that arises from changes in land relative humidity alone, and $A^{\mathcal{H}}_{\text{O}}$ is the contribution that arises from changes in ocean relative humidity alone. The land and ocean surface air relative humidities are $\mathcal{H}_L$ and $\mathcal{H}_O$, respectively. The contribution A^T varies non-monotonically with temperature and has a maximum at an ocean surface air temperature of roughly 290K when the land-ocean contrast in equivalent potential temperature is zero (Byrne and O'Gorman, 2013a). We interpret $A^T - 1$ as the contribution of the land-ocean contrast in the control climate (since it would be zero if temperatures and humidities were equal over land and ocean in the control climate). The magnitudes of the contributions from changes in relative humidity, $A^{\mathcal{H}}_{\text{L}}$ and $A^{\mathcal{H}}_{\text{O}}$, are typically larger for higher temperatures and lower land relative humidities for given changes in relative humidity.

All contributions are evaluated by calculating the land temperature change assuming equal changes in equivalent potential temperature over land and ocean according to (3.1). Non-linear interactions between the different contributions are neglected assuming a small change in climate. Changes in surface pressure are not included when calculating the contributions (these changes do not substantially affect the results). The land-ocean temperature contrast in the control climate and the changes in land relative humidity are the largest contributions to the tropical amplification factor (Fig. 3-4b) with equal magnitudes in the multimodel median ($A^T - 1 = A^{\mathcal{H}}_{\text{L}} = 0.17$).

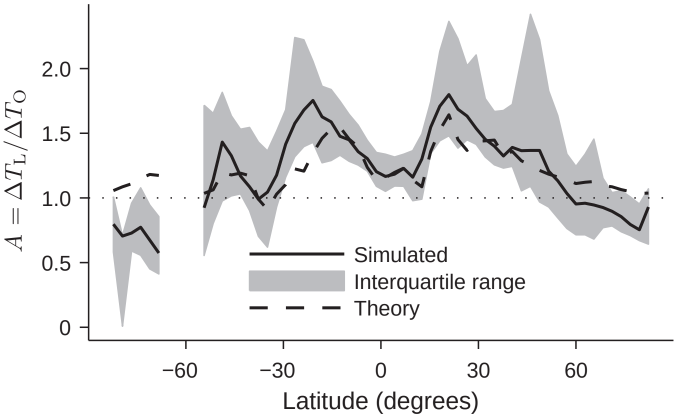

Figure 3-7: As in Fig. 3-2 but for trends (1950-2004) in the historical simulations rather than changes under RCP8.5. Here, ΔT_{L} and ΔT_{O} denote land and ocean temperature trends, respectively.

Changes in ocean relative humidity make a smaller contribution ($A_{\mathrm{O}}^{\mathcal{H}} = 0.06$). Although the changes in land and ocean relative humidity are typically of different signs, both $A_{\mathrm{L}}^{\mathcal{H}}$ and $A_{\mathrm{O}}^{\mathcal{H}}$ contribute positively to the total amplification factor. The contribution from changes in land relative humidity, $A_{\mathrm{L}}^{\mathcal{H}}$, is strongly correlated across models with the simulated amplification factor ($r = 0.77$). It also has a large intermodel range of 0.4, and changes in land relative humidity are the primary contributor to intermodel scatter in the tropical warming contrast. The other contributions, $A^{T} - 1$ and $A_{\mathrm{O}}^{\mathcal{H}}$, have smaller intermodel ranges (0.2 and 0.1, respectively) and they are more weakly correlated with the simulated amplification factor ($r = -0.35$ and 0.28, respectively), with a negative correlation coefficient in the case of $A^{T} - 1$.

In summary, both the land-ocean contrast in the control climate and the land relative humidity change contribute strongly to the warming contrast in the tropics, with a smaller contribution from the ocean relative humidity change that is also positive. Only the land relative humidity change is strongly linked to intermodel differences in the tropical warming contrast.

3.3.3 Trends in the historical simulations

We find qualitatively similar results for temperature and relative humidity trends over the period 1950-2004 in the historical simulations (Figs. 3-7 and 3-8). In applying

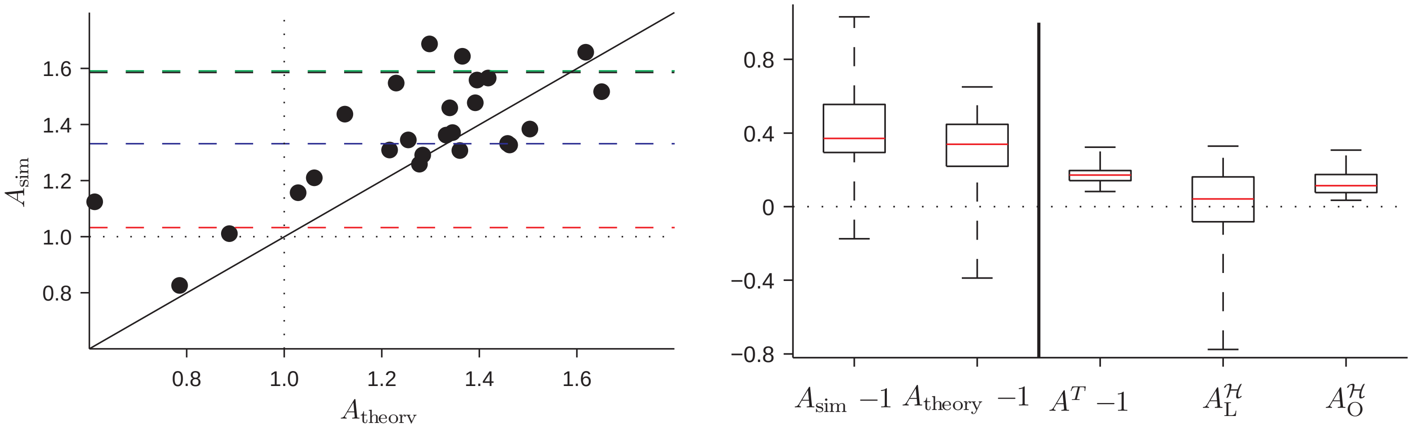

(a) (b)

Figure 3-8: As in Fig. 3-4 but for trends (1950-2004) in the historical simulations rather than for changes under RCP8.5. The red, blue, green, and black dashed lines in (a) denote the amplification factors calculated using land and ocean temperature trends (1950-2004) from the HadCRUT3, MLOST, GISTEMP, and BEST surface temperature datasets, respectively. The observational temperature trends are calculated by first averaging over all available land and ocean data between 20°S and 20°N, with area weighting, and then computing the trends using linear least squares regressions. Due to the sparsity of gridded humidity observations over tropical land, for instance in the HadCRUH dataset (Willett et al., 2008), we do not estimate the amplification factor for observations.

the theory to estimate the historical trends in land temperature, we first calculate the seasonally-varying climatology of the difference in equivalent potential temperature between land and ocean at each latitude. This climatology is used together with the monthly ocean temperatures and land and ocean relative humidities to estimate a time series of land temperature at a given latitude, which is then used to calculate the theoretical amplification factor based on trends. The temperature trends are calculated using linear least squares regressions. The multimodel-median tropical amplification factor is 1.37 for the trends compared with an estimate of 1.34 from the theory, both of which are slightly smaller than the corresponding values for the RCP8.5 scenario. The intermodel spread in the historical amplification factors is reasonably well bounded by three observational datasets (Fig. 3-8a), though the large differences in the amplification factor between these datasets is indicative of sparse data coverage at low latitudes (see Section 3.4).

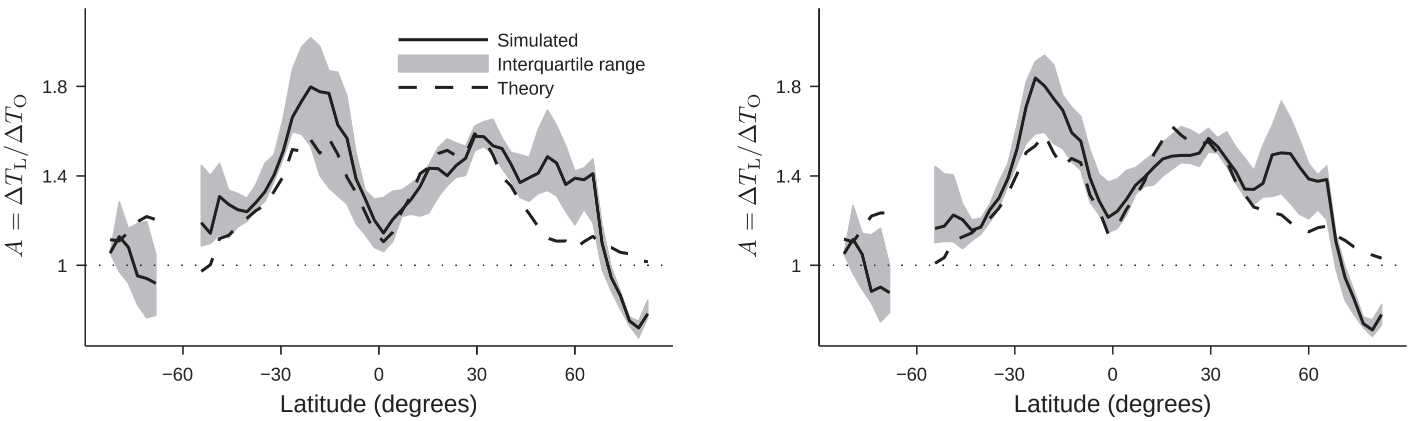

(a) (b)

Figure 3-9: As in Fig. 3-2 but using (a) daily-maximum surface air temperatures and daily-minimum surface relative humidities in the subset of models for which the data were available and (b) daily-mean temperatures and relative humidities for the same subset of models as in (a). The subset of models used in this figure is listed in Section 3.3.4.

3.3.4 Sensitivity to the diurnal cycle

Because of the strong diurnal cycle of convection over land, it could be argued that the theory should be more applicable to daily-maximum temperatures rather than daily-mean temperatures. To test the sensitivity of our results to the diurnal cycle, we repeated the analysis (under the RCP8.5 scenario) using monthly means of the daily-maximum temperatures and daily-minimum relative humidities (mean surface pressures are still used when calculating equivalent potential temperatures as in the standard calculation). Only 11 models[4] in the CMIP5 archive included sufficient data for this analysis. The results for this subset of models show that both the amplification factors and the performance of the theory are similar regardless of whether mean temperatures and relative humidities are used or daily-maximum temperatures and daily-minimum relative humidities are used (Fig. 3-9), which suggests that the land-ocean warming contrast in the models is not strongly sensitive to the diurnal cycle.

---

[4] The subset of models used for the analysis of daily-maximum temperatures and daily-minimum relative humidities are CanESM2, CNRM-CM5, CSIRO-Mk3-6-0, HadGEM2-CC, INMCM4, IPSL-CM5A-LR, IPSL-CM5A-MR, IPSL-CM5B-LR, MIROC5, MIROC-ESM, and MRI-CGCM3. Other models were excluded because of lack of available data at the time when the analysis was conducted.

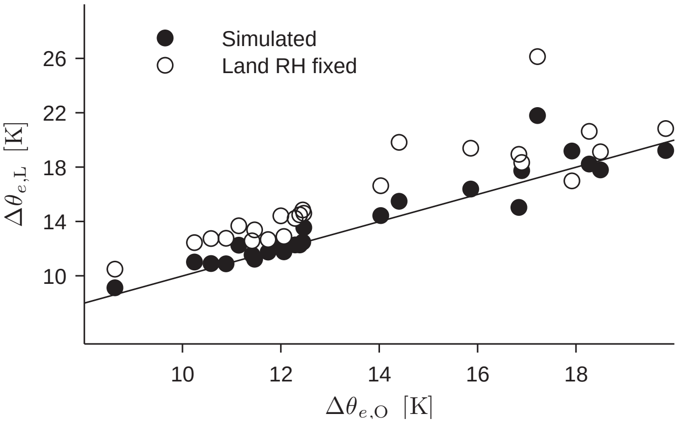

Figure 3-10: Changes in tropical-mean (20°S to 20°N) surface air equivalent potential temperature over land vs ocean (filled circles). The equivalent potential temperatures are calculated using the time-mean temperatures and relative humidites at each grid point prior to averaging over the tropics. The unfilled circles show the same quantities but with land relative humidity held fixed under climate change. The solid line corresponds to equal changes over land and ocean.

3.3.5 Implications for changes in heat stress

Equivalent potential temperature is closely related to wet bulb temperature, and changes in wet bulb temperature are a useful measure of changes in heat stress under climate change (Sherwood and Huber, 2010). As a result, changes in heat stress over tropical land are strongly constrained for a given change in ocean temperature and humidity by the equal changes in equivalent potential temperature over tropical land and ocean (Eq. 3.1 and shown for individual models in Fig. 3-10). For example, a greater decrease in relative humidity over land due to a change in surface conditions must be compensated for by a greater increase in land temperature, such that the change in equivalent potential temperature matches that over ocean. The link between increases in land heat stress and changes over the ocean is considerably weakened if the changes in land relative humidity are neglected (Fig. 3-10). Because of this compensation between land temperature and relative humidity changes [as also pointed out by Fischer and Knutti (2013)], our results imply that changes in tropical heat stress over land may not depend greatly on the details of a particular land surface model, but are instead constrained by the better understood and simulated changes in ocean temperature and humidity. Further work would be needed

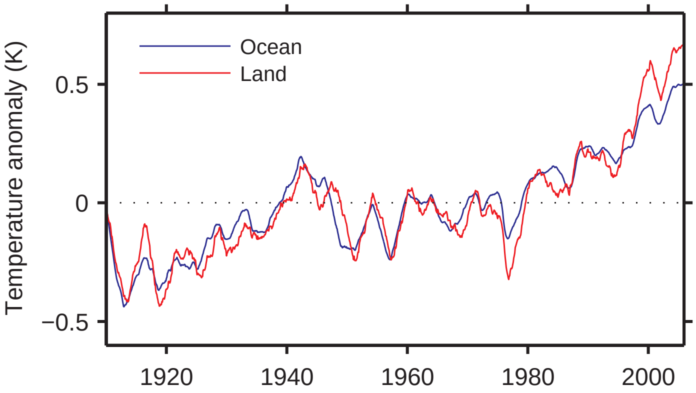

Figure 3-11: Time series (1910-2005) of land and ocean surface temperatures from HadCRUT3 (Brohan et al., 2006) averaged from 40°S to 40°N with area weighting. A 3-year moving average filter has been applied to the data. Due to sparse observational data and the highly variable temperature responses amongst the various climate models at high latitudes, and also because the convective quasi-equilibrium theory for the warming contrast is more valid closer to the equator, we restrict our analysis of the warming contrast in observations to lower latitudes (40°S to 40°N).

to assess whether this constraint on mean quantities is relevant for extremes such as annual maxima in measures of heat stress.

3.4 Warming contrast in observations

We have investigated the land-ocean warming contrast in CMIP5 simulations of both global warming and the historical period, and have shown that the modeled tropical amplification factors are in broad agreement with observations over 1950 to 2004 (Fig. 3-8a). During this period there was enhanced land warming relative to the ocean, as also shown by Lambert and Chiang (2007) and expected from the convective quasi-equilibrium theory discussed above. Studying a timeseries of observed land and ocean surface temperatures (HadCRUT3 data, Fig. 3-11) over the latter part of the 20th century, the warming contrast is apparent, but between 1910 and 1950, say, the land and ocean temperature trends are approximately equal and the warming contrast is small. A convective quasi-equilibrium explanation for the lack of a warming contrast over this period would involve increases in land relative humidity and/or decreases in ocean relative humidity, following (3.1) and (3.2). However, investigating this hypothesis using observations is difficult as both surface temperature and humidity data are required; gridded temperature data is generally sparse over 1910 to 1950, and the commonly used gridded surface humidity dataset covers only 1973-2004 (HadCRUH, Willett et al., 2008). The NOAA 20th-Century Reanalysis (Compo et al., 2011) does span 1910-1950, however using reanalysis data to compute trends is problematic (e.g., Bengtsson et al., 2004) and, furthermore, water cycle variables such as relative humidity can be unreliable (Dessler and Davis, 2010). In light of these issues, we use a comparison of observations, reanalysis, and the historical CMIP5 simulations to understand the lack of a warming contrast in observations between 1910 and 1950.

Over 1910 to 1950 and averaged between 40°S and 40°N, four surface temperature datasets[5] show amplification factors of less than 1, indicating marginally enhanced ocean warming over that period (Fig. 3-12a). The amplification factors in observations are calculated by averaging over all available data in each month (with area weighting) before computing the land and ocean temperature trends using linear least squares regressions. In contrast, all CMIP5 models (and the 20th century reanalysis) exhibit strongly enhanced land warming over the same period, with a multimodel-median amplification factor of 1.7. In a later period, 1965-2005, over which the observations do show a warming contrast (Fig. 3-11), the models and observations are in much better agreement, with observational temperature datasets and the reanalysis fitting within the model spread (Fig. 3-12b).

Why do the models and observations disagree between 1910 and 1950? One possibility is sparse data coverage and/or changes in the data coverage over time. Over both land and ocean for the HadCRUT3 dataset, the area coverage changes substantially with time, including a steady increase in land coverage and sharp changes in ocean coverage over the 1910-50 period (Fig. 3-13). It is plausible that the incomplete and changing data coverage could explain part of the discrepancy between the amplification factors in the models and observations. Indeed coverage biases in

---

[5] The surface temperature datasets analyzed are: HadCRUT3 (Brohan et al., 2006), GISTEMP (Hansen et al., 2010), MLOST (Smith et al., 2008), and BEST (Rohde et al., 2013).

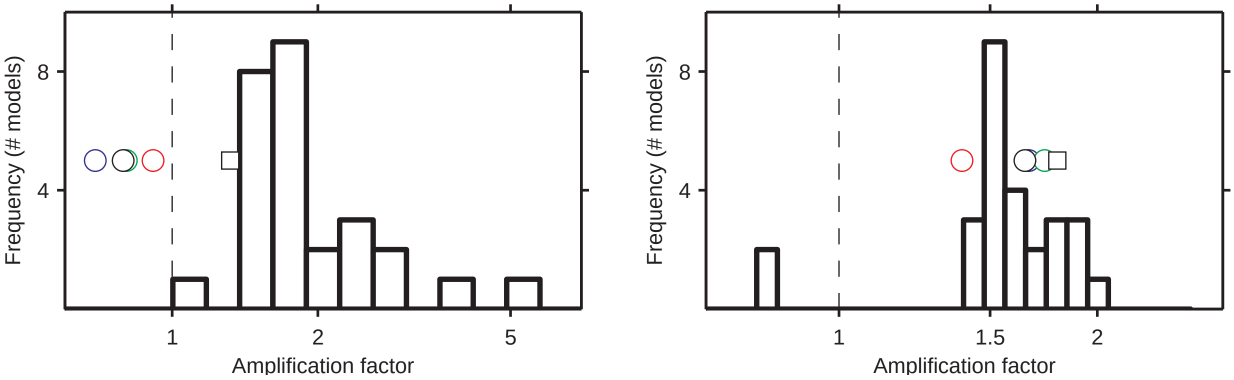

(a) No subsampling: 1910-50 (b) No subsampling: 1965-2005

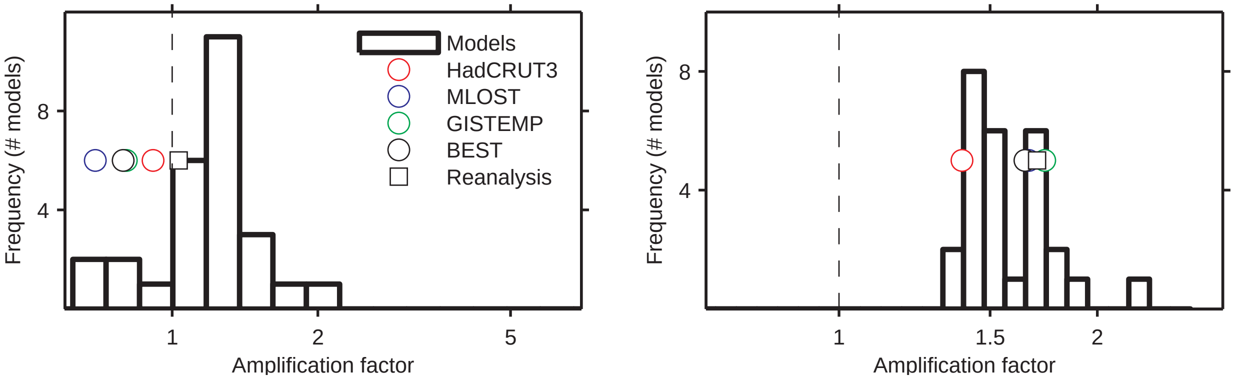

(c) Models subsampled: 1910-1950 (d) Models subsampled: 1965-2005

Figure 3-12: Histograms of amplification factors, averaged from 40°S to 40°N, for the historical CMIP5 simulations (a) over 1910-50 and (b) over 1965-2005. Circles denote the observed amplification factors over the same periods in three surface temperature datasets (HadCRUT3, MLOST, GISTEMP, and BEST plotted as red, blue, green, and black circles respectively). The black square is the amplification factor from the NOAA 20th-Century Reanalysis. For (c) and (d), the CMIP5 models and the NOAA 20th-Century Reanalysis have been subsampled to the HadCRUT3 observations at each month. Note that the horizontal axes and the box widths are in log scale.

temperature observations have recently been invoked in an attempt to explain the reduced global warming trends of the last decade (Cowtan and Way, 2014).

To examine the influence of data coverage on the observed land-ocean warming contrast, we subsample the CMIP5 models and the reanalysis data to the available HadCRUT3 observations at each month, before re-computing the land and ocean temperature trends and the amplification factors for the 1910-50 and 1965-2005 periods (Figs. 3-12c and 3-12d and Table 3.1). For 1965-2005, the CMIP5 amplification factors are reduced marginally when the models are subsampled to the observations (a

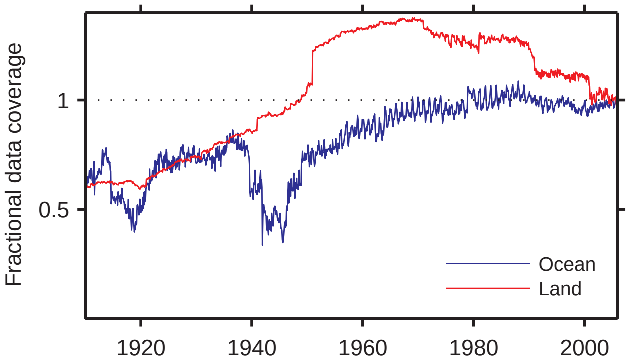

Figure 3-13: Time series of the normalized area of data coverage over land and ocean globally, respectively, in the HadCRUT3 surface temperature dataset (with area weighting). We have normalized by the areas of land and ocean covered by the dataset in the last month of the time period (i.e., December, 2005). We note that the land coverage peaked in approximately 1970 and has since been declining, while the ocean coverage has been relatively constant since 1980.

multimodel-median amplification factor of 1.56 without subsampling versus 1.52 with subsampling) but the observations and the reanalysis remain within the model spread (Fig. 3-12d). For 1910-50, however, subsampling the models reduces the multimodel-median amplification factor more substantially (from 1.74 to 1.22) and the observations and reanalysis now lie within in the model spread, albeit clustered on the lower end (Fig. 3-12c). This suggests that the lack of an observed warming contrast between 1910 and 1950 may not be due to increases in land relative humidity and/or decreases in ocean relative humidity, which would be required according to the CQE theory, but rather may be an artifact of sparse temperature data and changes in the data coverage over time.

This effect is emphasized by plotting timeseries of land and ocean temperatures between 1910 and 1950 using NOAA 20th-Century Reanalysis data (Fig. 3-14). When the reanalysis data are not subsampled to the HadCRUT3 observations (Fig. 3-14a) there is a moderate warming contrast ($A = 1.31$), but when the data are subsampled (Fig. 3-14b) the warming contrast is negligible ($A = 1.03$) and in closer agreement with the observations. Similar results are found when we examine global temperature trends over land and ocean in the reanalysis data.

One way to strengthen confidence in these results would be to subsample the

	Amplification factors			
	1910-1950		1965-2005	
	No subsampling	With subsampling	No subsampling	With subsampling
Models	1.74	1.22	1.56	1.52
Reanalysis	1.32	1.03	1.80	1.70
HadCRUT3	0.91	-	1.39	-
GISTEMP	0.80	-	1.74	-
MLOST	0.69	-	1.66	-
BEST	0.79	-	1.65	-

Table 3.1: Amplification factors for the CMIP5 models, the NOAA 20th-Century Reanalysis, and three observational datasets, computed for two periods (1910-1950 and 1965-2005) and averaged from 40°S to 40°N with area weighting. Results are displayed for two cases: (i) Where the models and reanalysis are not subsampled, and (ii) where the models and reanalysis are subsampled to the available HadCRUT3 observations at each month. For the models, the multimodel-median value is shown in each case.

CMIP5 models to the other observational datasets (MLOST, GISTEMP, and BEST) and check whether similar behavior is found, i.e. agreement between the models and observations when the models are subsampled. However, the spatial coverage in these three additional datasets is almost complete, relative to HadCRUT3, for the periods (1910-50 and 1965-2005) and area (40°S to 40°N) considered here. This enhanced coverage relative to HadCRUT3, despite all the datasets using similar input data, is due to differences in the protocols and methods regarding the extrapolation of observations to regions with limited temperature measurements. For example, GISTEMP uses kernal smoothing for extrapolating to less-observed areas while BEST uses a technique known as kriging. Due to the near-complete spatial coverage in these three datasets, subsampling the CMIP5 models to the observations would not change the amplification factors substantially. This raises two questions: (i) Why the datasets with complete spatial coverage show amplification factors of less than 1 between 1910-50? (ii) Why these datasets disagree with the CMIP5 models? One possibility is that the CMIP5 models are incorrect and indeed there was no land-ocean warming contrast between 1910 and 1950. Another possibility is that the extrapolation techniques used in the MLOST, GISTEMP, and BEST datasets are imperfect and give rise to erroneously small amplification factors. For instance, extrapolating ocean and coastal temperature data to the sparsely-measured continental interiors could plausibly lead to an underestimation of warming trends over land. Our analysis above, in which we subsample the models and reanalysis to the sparse HadCRUT3 observations and find similar amplification factors over 1910-50, suggests that the extrapolation to poorly observed regions might be problematic but further investigation is needed and is left to future work.

3.5 Conclusions

We have investigated the land-ocean warming contrast and its links to surface relative humidities in CMIP5 simulations under the RCP8.5 scenario. While simulated changes in surface temperature and relative humidity show a land-ocean contrast and vary sharply near coastlines, changes in equivalent potential temperature are similar over land and ocean and vary on relatively large scales. A theory based on convective quasi-equilibrium that assumes equal changes in equivalent potential temperature over land and ocean is shown to capture the magnitude and intermodel scatter of the warming contrast in the tropics and much of its meridional variation at low latitudes. According to the theory, the land-ocean contrast in the control climate and the changes in land relative humidity are of equal importance for the tropical warming contrast, with a smaller contribution from changes in ocean relative humidity. Similar results are found for trends in the historical simulations, and the amplification factors and the performance of the theory are found to be insensitive to whether daily-mean or daily-maximum temperatures are considered.

The theory implies a land-ocean warming contrast even in the absence of changes in relative humidity (A^T in Eq. 3.2). As discussed in Section 3.2, this warming contrast leads to a reduction in the land relative humidity (because of the ocean's role as a source for water vapor over land) which then feeds back on the land-ocean warming contrast according to the theory. A more complete theory would take the water vapor budget into account, in addition to the atmospheric dynamical constraints considered here. The extended theory would involve influences on land relative humidity such

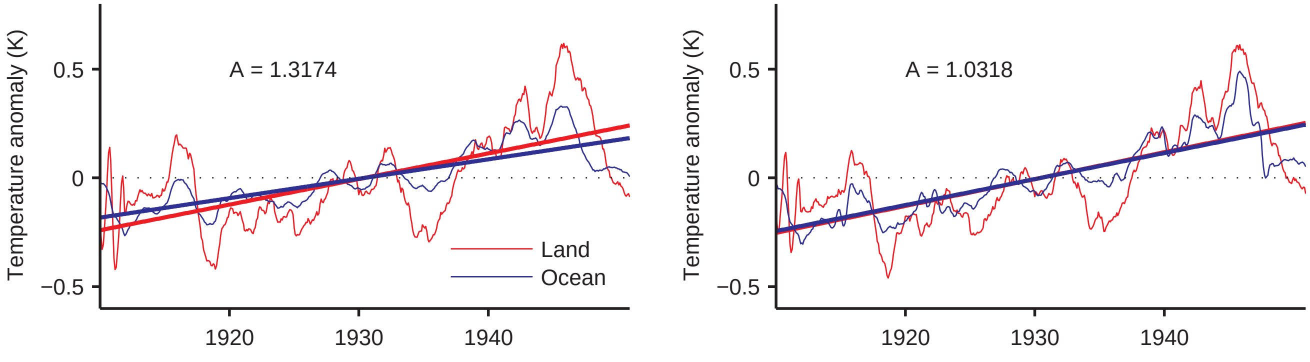

(a) No subsampling (b) With subsampling

Figure 3-14: Time series (1910-50) of land and ocean surface temperatures from the NOAA 20th-Century Reanalysis (Compo et al., 2011) averaged from 40°S to 40°N with area weighting (light lines) along with the least-squares trends (heavy lines) (a) without data subsampling and (b) after subsampling to the HadCRUT3 observations. A 3-year moving average filter has been applied to the data.

as changes in water vapor transport and stomatal closure. Such an approach is not attempted here, but the additional constraint from the water vapor budget should be kept in mind when interpreting the results in this paper.

The importance of changes in land surface relative humidity for the intermodel scatter of the tropical land-ocean warming contrast emphasizes the need to better constrain changes in land relative humidity in model simulations (changes in land relative humidity under warming will be investigated in the next chapter). It also provides motivation to better understand the recent drop in land relative humidity in observations and reanalysis (Simmons et al., 2010). On the other hand, the constraint of equal changes in equivalent potential temperature over tropical land and ocean implies that changes in heat stress over tropical land are strongly constrained by changes in equivalent potential temperature over ocean.

We have focused on the tropics because the assumptions underlying the theory are most applicable there. Further work is needed to better understand the relationship between changes in temperatures and relative humidities at higher latitudes, particularly in the northern mid-latitudes.

A comparison of historical land and ocean temperature trends in observations and models suggests that the lack of an observed warming contrast in the first half of the

20th century may be due to incomplete data coverage. Further work is needed to identify the relative importance of sparse data, changes in data coverage, and data extrapolation techniques in determining the observed warming contrast, and to use observations and improved reanalyses to validate the role of relative humidity changes in land and ocean temperature trends over the historical period.

Finally, understanding the land-ocean warming contrast on interannual timescales (as related to the El Niño-Southern Oscillation, for example) is arguably as important as understanding the response to CO_2-induced global warming. Preliminary analysis suggests that the interannual warming contrast has a multimodel-mean magnitude that is comparable to the global warming contrast but the interannual and global warming contrasts in the various models are not significantly correlated. Additional research is needed to understand the dependence of the warming contrast on the nature and timescale of the forcing, and to investigate the utility of the convective quasi-equilibrium theory in explaining the interannual warming contrast.

Chapter 4

Response of land relative humidity to global warming

4.1 Introduction

Changes in near-surface land and ocean temperatures are closely tied to changes in relative humidity, particularly at low latitudes (Byrne and O'Gorman, 2013a,b). However, the convective quasi-equilibrium theory discussed in the previous chapters constrains only changes in equivalent potential temperature, not the changes in surface-air temperature and relative humidity individually. To estimate the land-ocean warming contrast we were required to take the land and ocean relative humidity changes as given. But what controls the magnitude of these relative humidity changes? In this chapter we will introduce a conceptual box model to estimate changes in land relative humidity and to improve our understanding of the processes controlling land humidity. We will then apply this conceptual model to idealized and Climate Model Intercomparison Project 5 (CMIP5) simulations.

Under global warming, climate model simulations predict small increases in surface-air ocean relative humidity at a rate of less than 1%/K (O'Gorman and Muller, 2010; Laîné et al., 2014; Fu and Feng, 2014) (Fig. 4-1). Over land, however, there is a strongly contrasting response, with relative humidity decreases of up to 2%/K in many regions. Observations also show a sharp decrease in land relative humidity in response to global warming over recent decades (Simmons et al., 2010), but no significant trend over oceans (Dai, 2006). Not only is the response of land relative humidity important for understanding the land-ocean warming contrast, it also modulates changes in the terrestrial water cycle under global warming (to be discussed in Chapter 5), and is a key variable in the surface energy and water budgets. Despite this importance, however, changes in land relative humidity are poorly understood.

Before discussing the conceptual model for changes in land relative humidity, we briefly review the changes over ocean. The modest projected increases in ocean relative humidity under warming can be understood using surface energy balance arguments (Boer, 1993; Held and Soden, 2000; Schneider et al., 2010): Ocean evaporation is largely controlled by the degree of sub-saturation of near-surface air. If we neglect the air-sea temperature disequilibrium, the dependence of evaporation, E, on the surface-air relative humidity, $\mathcal{H}$, is given by $E \propto (1-\mathcal{H})q^*$, where q^* is the surface-air saturation specific humidity (Held, 2014). Assuming no changes in the exchange coefficient, surface winds, or in the temperature disequilibrium, fractional changes in evaporation equal the sum of fractional changes in the degree of sub-saturation and in the saturation specific humidity:

$$\frac{\delta E}{E} \approx \frac{\delta(1-\mathcal{H})}{(1-\mathcal{H})} + \frac{\delta q^*}{q^*}. \tag{4.1}$$

The constraint of atmospheric radiative cooling limits changes in the global-mean evaporation and precipitation rates to approximately 2%/K (e.g., O'Gorman et al., 2012), and the Clausius-Clapeyron relation gives $\delta q^*/q^* \approx 7\%/\mathrm{K}$ (e.g., Hartmann, 1994). Therefore, from (4.1), $\delta(1-\mathcal{H})/(1-\mathcal{H}) \approx -5\%/\mathrm{K}$ which corresponds to an ocean relative humidity increase of roughly 1%/K taking a basic-state relative humidity of 80% (here and throughout this chapter, relative humidity changes are expressed as absolute rather than fractional changes). This is in qualitative agreement with simulated changes (Fig. 4-1) though the estimated increases are generally too large, indicating that effects such as changes in the surface temperature disequilibrium and in surface winds also matter for the ocean relative humidity.

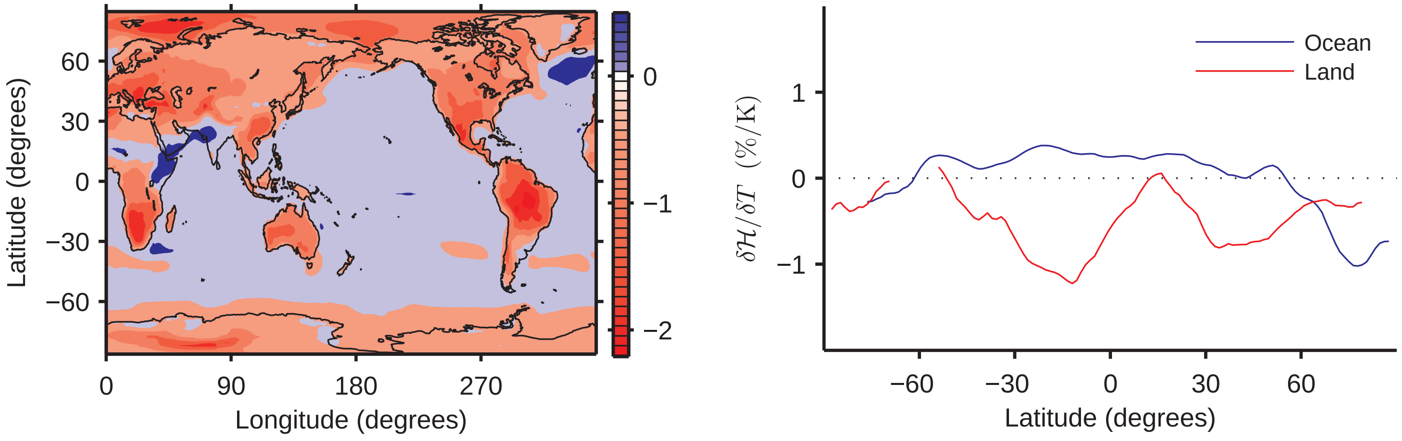

(a)

(b)

Figure 4-1: Multimodel-mean changes in surface-air relative humidity between the historical (1976-2005) and RCP8.5 (2070-2099) simulations, normalized by the global-mean surface-air temperature changes [(a) and (b)]. For (b), the blue and red lines represent zonal averages over ocean and land regions, respectively. All quantities are expressed in units of %/K.

The above explanation for small increases in ocean relative humidity under warming relies on (i) changes in evaporation being approximately 2%/K, following the global-mean constraint, and (ii) these evaporation changes being dominated by changes in the degree of sub-saturation of the surface-air layer. These two conditions are generally not valid over land where the moisture supply for evapotranspiration is limited and varies hugely across regions, for example between deserts and tropical rainforests. Under warming, the spatially inhomogeneous response of soil moisture, in addition to effects such as changes in land use and in stomatal conductance under elevated CO_2 concentrations (e.g., Andrews et al., 2011; Cronin, 2013), leads to land evapotranspiration changes which have substantial spatial structure. For example, evapotranspiration increases in tropical Africa and decreases in the Amazon in simulations of global warming (Laîné et al., 2014). Even if the changes in land evapotranspiration were taken as given, near-surface relative humidity is merely one of the myriad processes influencing those evapotranspiration changes (many of which are not well understood or modeled), and so it is clear that inferring land relative humidity changes using a surface energy balance framework is challenging.

To understand the expected decreases in land relative humidity, we take a different approach following that of Rowell and Jones (2006), O'Gorman and Muller (2010), Sherwood and Fu (2014), and others. These authors reasoned that the land boundary-layer humidity is largely determined by the moisture flux from the ocean. Under global warming, as land warms more rapidly than ocean, the rate of increase of the moisture supply from the oceans to the land cannot keep pace with the faster increase in saturation specific humidity over land, implying a drop in land boundary-layer relative humidity. This explanation is attractive because it relies on robust features of the global warming response, namely (i) an approximately Clausius-Clapeyron increase in specific humidity over ocean and (ii) stronger surface warming over land. Indeed, the most recent Intergovernmental Panel on Climate Change (IPCC) report cites this argument to explain both the observed and projected land relative humidity decreases (Stocker et al., 2013, see Section 12.4.5.1). However, to date, this idea has not been formalized mathematically nor investigated quantitatively using either observations or models. Thus, it not clear to what extent changes in land relative humidity can be understood as a simple consequence of enhanced land warming and increasing moisture transport from ocean to land. Indeed, as demonstrated in Chapters 2 and 3, the land warming itself is closely tied to both relative humidity and its changes; this feedback process is discussed in Section 4.4. It is also plausible, for example, that changes in evapotranspiration resulting from soil moisture decreases or stomatal closure would impact the land relative humidity (e.g., Cao et al., 2010), though such effects are not explicitly considered in the simple argument outlined above.

To test the idea of an oceanic control on land humidity changes, we now derive a conceptual box model for the moisture balance of the atmospheric boundary layer over land before applying the model to idealized and full-complexity simulations of climate change.

4.2 Conceptual model

4.2.1 Theory

We begin by considering the moisture balance of the boundary layer of the atmosphere above land (see schematic, Fig. 4-2). We assume that the specific humidity of this layer is determined by two processes: (i) Horizontal mixing with the ocean (e.g., via mean-wind advection, diurnal sea breeze) and (ii) vertical mixing with the free troposphere (e.g., via large-scale vertical motion, shallow and deep convection). In this formulation of the conceptual model, we do not explicitly consider the influence of land evapotranspiration on the boundary-layer specific humidity though we return to this issue in Section 4.3.

For this box model, the time evolution of the land boundary-layer specific humidity, q_L, can be written as follows:

$$\frac{dq_L}{dt} = \underbrace{\frac{1}{L}v_1}_{1/\tau_1}(q_O - q_L) + \underbrace{\frac{1}{h}v_2}_{1/\tau_2}(q_{FT} - q_L), \tag{4.2}$$

where L is a horizontal length scale representing the expanse of land influenced by horizontal mixing with the ocean, h is the depth of the boundary layer, v_1 and v_2 are horizontal and vertical mixing velocities, respectively, q_O is the specific humidity of the ocean layer, and q_{FT} is the specific humidity of the free troposphere (which is assumed to be the same over land and ocean). We define $\tau_1 = L/v_1$ and $\tau_2 = h/v_2$ as horizontal and vertical mixing timescales, respectively.

Writing the free-tropospheric humidity in terms of ocean boundary-layer humidity, i.e. $q_{FT} = \lambda q_O$, where λ is a constant, and taking the steady-state solution we find:

$$q_L = \frac{\lambda\tau_1 + \tau_2}{\tau_1 + \tau_2} q_O \equiv \gamma q_O, \tag{4.3}$$

where we have defined the parameter γ as the ratio of land to ocean specific humidities. If we assume that changes in γ are small, relative to changes in q_O, as climate changes

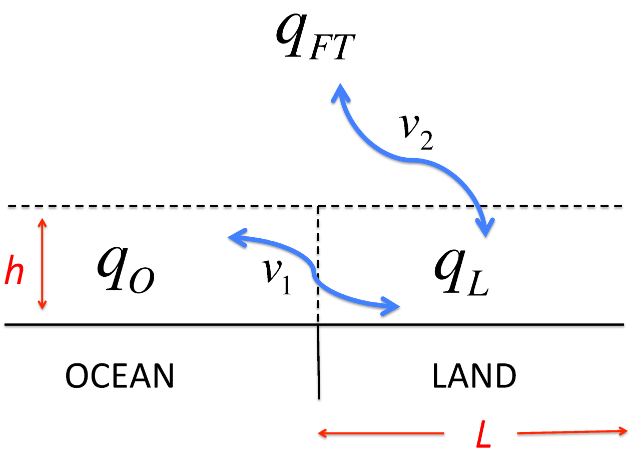

Figure 4-2: Schematic diagram of the conceptual box model for changes in land humidity, summarized by (4.4). The height of the boundary layer is h, L is a horizontal length scale, q_O and q_L are the ocean and land boundary-layer specific humidities, respectively, and q_{FT} is the free tropospheric specific humidity. Horizontal and vertical mixing velocities are denoted by v_1 and v_2, respectively.

then we can write:

$$\delta q_L \approx \gamma \delta q_O. \tag{4.4}$$

Our conceptual model suggests a simple hypothesis, expressed by (4.3) and (4.4), in which the ratio of land to ocean specific humidity remains constant as the climate changes. Calculating this ratio, γ, in the basic-state climate and then combining (4.4) with simulated changes in land temperature and ocean specific humidity, we can estimate the change in land relative humidity. Assuming (4.3) and (4.4) hold, it is clear that if land and ocean warm similarly then the relative humidity changes will also be similar. However, if land warms more than ocean, as expected under global warming, the land relative humidity will decrease for a constant ocean relative humidity. We now assess the validity of this box model using idealized general circulation model (GCM) simulations.

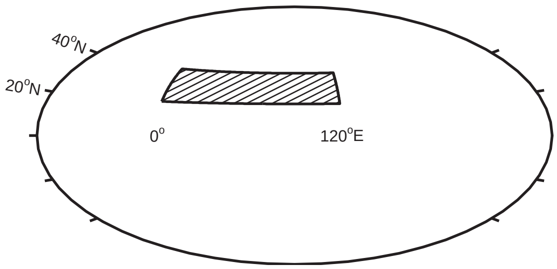

Figure 4-3: The idealized GCM simulations analyzed in this chapter have a subtropical continent covering 20°N to 40°N and 0°E to 120°E, with a slab ocean elsewhere.

4.2.2 Idealized GCM simulations

The conceptual model is applied to idealized GCM simulations over a wide range of climates. The GCM employed here is described in Chapter 2. The simulations we analyze have a subtropical continent spanning 20°N to 40°N and 0°E to 120°E, with a slab ocean elsewhere (Fig. 4-3). As in Chapter 2, we vary the climate over a wide range of global-mean surface temperatures (between 260K and 317K) by changing the longwave optical thickness, and we analyze nine simulations in total. The land hydrology is represented with a simple bucket model (Manabe, 1969) and all other surface properties are identical to those of the slab ocean.

When applying the conceptual model to relative humidity changes in these idealized simulations and later to changes in the CMIP5 simulations, for simplicity we assume that moisture is well-mixed in the boundary layer and so use the surface-air specific humidities to represent the entire boundary layer (in this case, surface-air quantities are taken to be those of the lowest atmospheric level in the GCM, the $\sigma = p/p_S = 0.989$ level). Land values are averaged over the entire subtropical continent (with area weighting), and the ocean averages are taken over neighboring ocean at the same latitudes, i.e. over 20°N to 40°N and 120°E to 360°E. We take the ocean averages over the area neighboring the land continent, in contrast to Chapter 2 where ocean averages in the control hemisphere were taken, because our conceptual model considers horizontal moisture transport from ocean to land. We calculate the γ parameter, i.e. the ratio of land to ocean specific humidities for each simulation (except the warmest) and then estimate δq_L between pairs of nearest-neighbor simu-

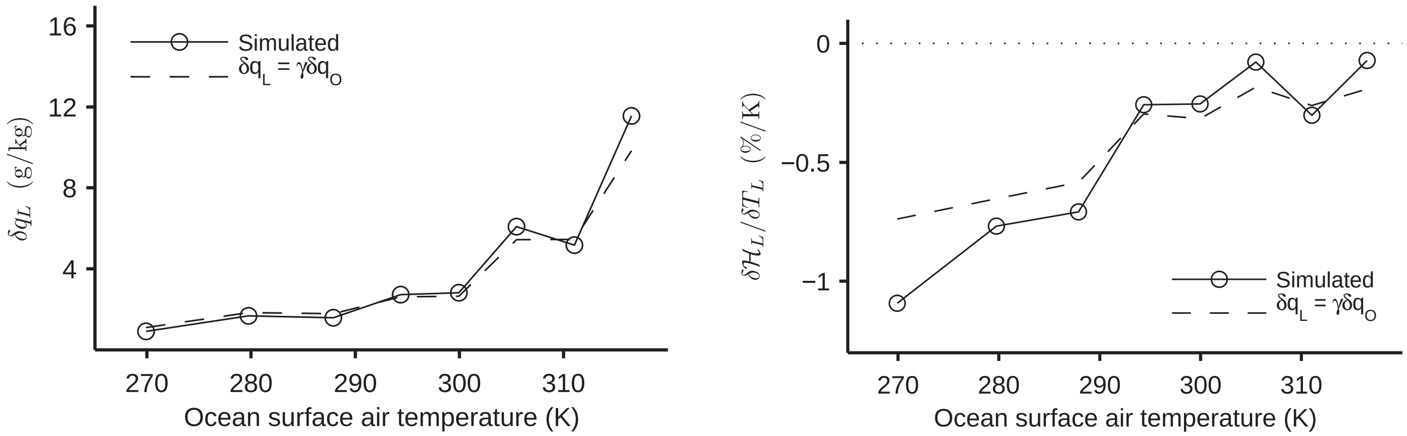

(a) Specific humidity changes over land

(b) Relative humidity changes over land

Figure 4-4: Changes in (a) surface-air land specific humidity and (b) surface-air land relative humidity (normalized by the land surface-air temperature change) between pairs of idealized GCM simulations with a subtropical continent. Solid lines denote the simulated changes and the dashed lines represent the estimated changes using the conceptual model (4.4).

lations as a function of γ and δq_O, where γ is assumed to be constant as the climate changes. The γ parameter has a mean value of 0.61 over the full range of simulations, with minimum and maximum values of 0.57 and 0.67, respectively. The estimates of changes in land specific humidity are then combined with simulated changes in the surface-air land temperature to obtain estimates of the changes in surface-air land pseudo-relative humidity, $\delta \mathcal{H}_L^{\text{pseudo}}$, which are quantitatively different to the changes in model relative humidity, $\delta \mathcal{H}_L$, for the idealized GCM and the CMIP5 models, particularly at high latitudes[1].

Land surface-air specific and relative humidity changes between the pairs of idealized GCM simulations, along with the estimates of these changes using (4.4), are plotted against the mid-point ocean temperature for each pair (Fig. 4-4). The changes in specific humidity, δq_L, generally increase as the climate warms (Fig. 4-4a) as we would expect given that absolute changes in specific humidity (at fixed relative humidity) increase with temperature following the Clausius-Clapeyron relation (e.g., Hartmann, 1994). The simulated specific humidity changes are well-captured by the conceptual model over the full range of climates, though the agreement deteriorates somewhat for the warmest simulations. The underestimation at high temperatures could be due to changes in the ratio of free tropospheric to surface-air ocean specific humidity, which in the conceptual model is assumed to remain constant under warming [due to enhanced warming aloft under climate change (e.g., Santer et al., 2005) we would expect a larger fractional increase in free-tropospheric specific humidity compared to boundary-layer specific humidity, in the absence of large relative humidity changes]. Estimates of the relative humidity changes are less accurate (Fig. 4-4b). For example, the relative humidity decreases in cold climates are underestimated, though the decreasing magnitude of the relative humidity changes as climate warms is captured.

---

[1] The conceptual model (4.4) predicts the changes in mean specific humidity which must be combined with the mean temperatures to estimate the relative humidity changes. However, because of the nonlinearity of the Clausius-Clapeyron relation, it is not possible to reproduce the GCM-generated relative humidity using these mean quantities and so we instead estimate a "pseudo-relative humidity" change and compare to the pseudo-relative humidity changes simulated by the models. We calculate the pseudo-relative humidity using the GCM's time-mean and spatial-mean specific humidities, temperatures, and pressures, i.e. $\mathcal{H}^{\text{pseudo}} = f(\overline{T}, \overline{p}, \overline{q})$ where the bars denote time and spatial averages. We analyze this quantity rather than the GCM-generated relative humidity, $\mathcal{H} = f(T, p, q)$.

Given the simplicity of the conceptual model, its ability to describe the behavior of land relative humidity in this idealized GCM is impressive. It suggests that our simple hypothesis of the ratio of land to ocean specific humidities staying constant under global warming is reasonable. However, the geometry and surface properties of Earth's land masses are more varied and complex than the idealized continent considered here. It is possible, for example, that changes in low-level onshore winds under warming could overwhelm the changes in ocean specific humidity and our simple model would fail to capture the land relative humidity changes. Therefore, to investigate our conceptual model more thoroughly, we turn to the full-complexity simulations from the CMIP5 archive.

4.2.3 CMIP5 simulations

We apply the conceptual model (4.4) to changes in land surface-air relative humidity between 30 year time averages in the historical (1976-2005) and RCP8.5 (2070-2099) simulations from the CMIP5 archive (Taylor et al., 2012). We analyze 19 models in total[2]. As for the idealized GCM analysis in Section 4.2.2, we assume moisture is well-mixed in the boundary layer and take surface-air specific humidity to be representative of the entire boundary layer (an analysis using the boundary-layer average specific humidity gives similar results). Changes in the surface-air specific humidity are estimated by first diagnosing the ratio of the land to ocean specific humidity at each latitude in the historical simulations, $\gamma = q_L/q_O$, using monthly- and zonal-mean land and ocean specific humidities (γ is undefined at latitudes where there is either no land or no ocean). By computing γ in this way, we are assuming that the horizontal exchange of moisture between land and ocean, described by the conceptual model, is taking place predominantly in the zonal direction. Using the diagnosed γ, and assuming it does not change as the climate warms following (4.4), changes in zonal-mean q_L are estimated as a function of changes in q_O (Fig. 4-5a).

The magnitude and latitudinal variations of the changes in zonal-mean q_L are reasonably well captured by the conceptual model, including the flattening of the meridional humidity gradient in the Northern Hemisphere midlatitudes. The magnitude of the changes is marginally underestimated at most latitudes which, as discussed in the case of the idealized GCM simulations, could be due to larger fractional increases in free-tropospheric specific humidity relative to surface-air humidity. Changes in the horizontal and vertical mixing timescales, τ_1 and τ_2, related to reduced convective mass fluxes out of the boundary layer in a warmer climate (e.g., Held and Soden, 2006), may also be important here.

Together with the simulated changes in monthly-mean surface-air land temperature, the estimated changes in specific humidity are used to estimate the land relative humidity changes. Due to the nonlinearity of the Clausius-Clapeyron relation and differences in how the various climate models compute saturation vapor presure, it is difficult to quantitatively reproduce the monthly-mean relative humidity outputted by

---

[2] The climate models considered in this section are: ACCESS1-0, ACCESS1-3, BCC-CSM1-1, BCC-CSM1-1-M, BNU-ESM, CanESM2, CNRM-CM5, CSIRO-Mk3-6-0, GFDL-CM3, GFDL-ESM2M, INMCM4, IPSL-CM5A-LR, IPSL-CM5A-MR, IPSL-CM5B-LR, MIROC-ESM, MIROC-ESM-CHEM, MIROC5, MRI-CGCM3, and NorESM1-M. The variables used in this chapter have the following names in the CMIP5 archive: Evaporation (*evspsbl*), surface-air specific humidity (*huss*), surface-air temperature (*tas*), and surface-air relative humidity (*hurs*).

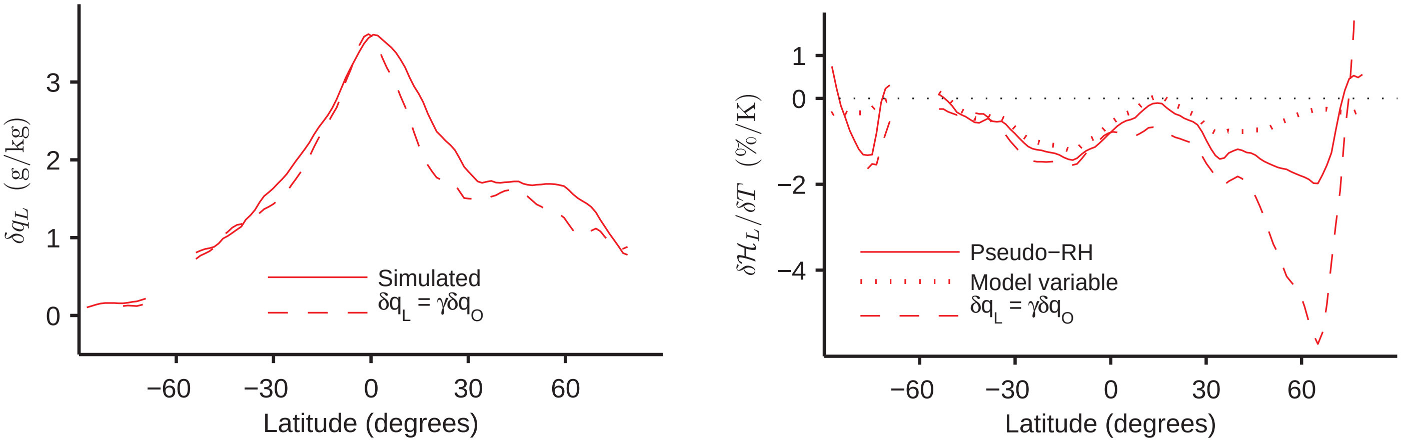

(a) Specific humidity changes over land

(b) Relative humidity changes over land

Figure 4-5: Multimodel-mean changes in zonally-averaged (a) surface-air land specific humidity and (b) surface-air land relative humidity (normalized by the global-mean surface-air temperature change) between the historical and RCP8.5 CMIP5 simulations. Solid lines denote the simulated changes (for the relative humidity changes, the solid line denotes the "pseudo-relative humidity" changes), and dashed lines represent the estimated changes using the conceptual model (4.4). For (b), the dotted line is the simulated relative humidity outputted by the models (named *hurs* in the CMIP5 archive).

climate models using monthly-mean temperatures and specific humidities (the use of zonal-mean quantities is also problematic). Therefore, we use the estimated monthly-mean specific humidity and temperature changes to compute estimated changes in "pseudo-relative humidity", where the pseudo-relative humidity is calculated as for the idealized GCM simualtions (described in Section 4.2.2 above). We then compare these estimates to the simulated pseudo-relative humidity changes obtained using the simulated specific humidity and temperature changes (Fig. 4-5b). Agreement between the pseudo- and model-outputted relative humidity changes over land is good at lower latitudes but not at higher latitudes (cf. dotted and solid lines in Fig. 4-5b), where the differing computations of saturation vapor pressure over ice in the various models becomes important. Whilst acknowledging these issues with calculating relative humidity, in the following discussions we will refer to "pseudo-relative humidity changes" as simply "relative humidity changes".

The simulated changes in land relative humidity are quite well described by the

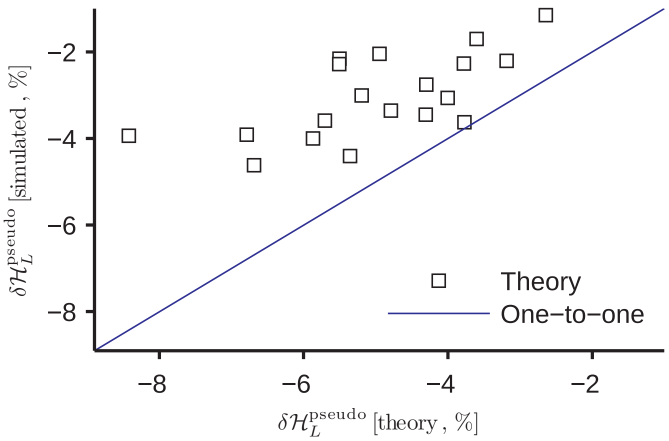

Figure 4-6: Simulated changes in surface-air land pseudo-relative humidity versus the estimates from the conceptual model (4.4) for each of the 19 CMIP5 models analyzed. Both quantities have been averaged over all land from 90°S to 90°N. The blue line is the one-to-one line and the correlation coefficient is $r = 0.66$.

conceptual model, particularly at lower latitudes (Fig. 4-5b). The estimated and simulated relative humidity changes in the various climate models are also correlated (Fig. 4-6), with the conceptual model explaining approximately 43% of the intermodel variance. Due to the general underestimation of the specific humidity increases by the conceptual model, the relative humidity decreases are overestimated, with a large discrepancy in the mid- to high-latitudes of the Northern Hemisphere. At these latitudes, there is more land than ocean and it is likely that changes in ocean specific humidity have less influence on land humidity in the continental interior. An equivalent way to express this is that the horizontal length scale, L, considered in our derivation of the conceptual model, is small at these latitudes compared to the scale of the continents. Changes in relative humidity in these inner continental regions may be more strongly influenced by local evapotranspiration changes, perhaps due to shifts in the iceline under global warming, an effect which is not considered in the conceptual model. In the next section we will develop an extended model for land relative humidity changes which depends explicitly on local evapotranspiration.

In this section we have analyzed changes in surface-air humidity, which we have assumed are representative of the entire boundary layer for which the conceptual model was derived. We have repeated our analysis using specific humidity averaged over the land boundary layer (where the top of the boundary layer is defined as the vertical level closest to 850hPa) and find results that are qualitatively similar to those obtained using surface-air humidity.

4.3 Extended model: Influence of evapotranspiration

Motivated by the hypothesis that land humidity and its changes are largely determined by moisture exchange with neighboring oceans rather than by local surface processes (e.g., Rowell and Jones, 2006), we have derived a conceptual model to understand changes in land relative humidity under global warming. This simple model qualitatively captures the behavior in vastly more complex GCMs. In our conceptual framework, the land specific humidity depends only on the ocean humidity, the ratio of free-tropospheric to ocean specific humidity, λ, and two mixing timescales, τ_1 and τ_2, describing the rates at which moisture is exchanged between the land and ocean boundary layers and with the free troposphere, respectively. The conceptual model has no explicit dependence on evapotranspiration, though an alternative derivation could assume a purely atmospheric control on evapotranspiration, i.e. $E_L = f(q_L)$, allowing the evapotranspiration dependence to be subsumed into the γ parameter. However, assuming an entirely atmospheric control on land evapotranspiration is unrealistic as changes in land surface properties, such as soil moisture or stomatal conductance, can change evapotranspiration in the absence of any changes in the overlying atmosphere. In particular, physiological forcing due to changes in stomatal conductance under elevated CO_2 conditions has been shown to reduce both evapotranspiration, by altering the surface exchange coefficient, and land relative humidity without changes in ocean humidity (Andrews et al., 2011). Changes in land-use could have similar effects (Jung et al., 2010). The conceptual model, summarized by (4.4), cannot capture these effects and so we now derive a variation of the model to examine the influence of evapotranspiration on relative humidity changes.

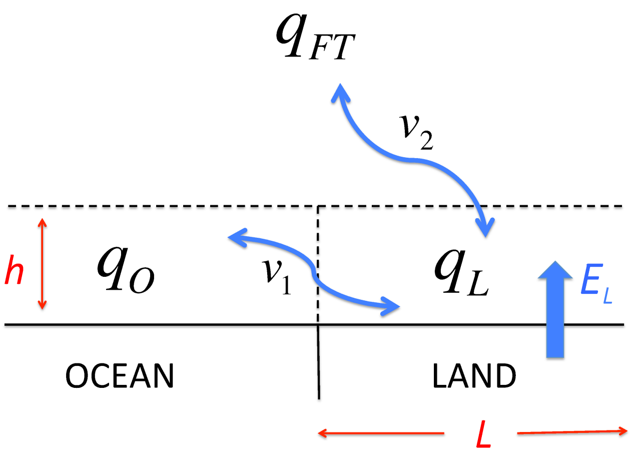

Figure 4-7: As in Figure 4-2, though now including land evapotranspiration, E_L, from the surface to the surface-air layer.

4.3.1 Derivation

The extended model is analogous to the original conceptual model though we now consider the moistening of the land boundary layer by evapotranspiration (see schematic, Fig. 4-7). The moisture balance of the boundary layer is:

$$\frac{dq_L}{dt} = \underbrace{\frac{1}{L}v_1}_{1/\tau_1}(q_O - q_L) + \underbrace{\frac{1}{h}v_2}_{1/\tau_2}(q_{FT} - q_L) + \frac{1}{\rho_a h}E_L, \tag{4.5}$$

where ρ_a is the density of air and E_L is the evapotranspiration from the land surface. Taking the steady-state solution, writing $q_{FT} = \lambda q_O$ as before, and rearranging we find:

$$q_L = \frac{\lambda\tau_1 + \tau_2}{\tau_1 + \tau_2}q_O + \frac{\tau_1\tau_2}{\rho_a h(\tau_1 + \tau_2)}E_L \equiv \gamma q_O + \epsilon E_L, \tag{4.6}$$

where we have defined $\epsilon = \tau_1\tau_2/[\rho_a h(\tau_1 + \tau_2)]$. If we assume once more that changes in the horizontal and vertical mixing timescales and in λ are negligible, and additionally that the height of the boundary layer is constant, we can write the extended model as follows:

$$\delta q_L \approx \gamma\delta q_O + \epsilon\delta E_L. \tag{4.7}$$

The extended model (4.7) has two terms contributing to changes in q_L: The familiar term arising from changes in q_O and a new land evapotranspiration term, $\epsilon \delta E_L$. We now return to the idealized and CMIP5 simulations to investigate the relative importance of each term in controlling changes in land relative humidity.

4.3.2 Application to simulations

We first examine the idealized GCM simulations with a subtropical continent (described in Section 4.2.2). In contrast to the original conceptual model (4.4), for which the single parameter γ was estimated in the basic-state simulations, the extended model (4.7) has 2 parameters to be computed, γ and ϵ. To estimate ϵ, the sensitivity of surface-air specific humidity to changes in land evapotranspiration at fixed q_O, we perform 2 additional idealized simulations with the same continental geometry as those discussed above. The additional simulations have the same longwave optical thickness ($\alpha = 1.0$, which corresponds to a climate similar to that of the present-day Earth, see Chapter 2 for details) but different, fixed evaporative fractions β, where $E_L = \beta E_0$ and E_0 is the potential evapotranspiration rate. Reducing β impedes evapotranspiration and is analogous to reducing soil moisture or lowering stomatal conductance. We use the simulations with different β values to estimate ϵ because q_O changes between these simulations are negligible and so $\delta q_L \approx \epsilon \delta E_L$. We perform two fixed-evaporative fraction simulations, with $\beta = 0.9$ and $\beta = 0.8$, and calculate ϵ using the q_L and E_L changes between the simulations, finding $\epsilon \approx 100\,\mathrm{kg}^{-1}\,\mathrm{m}^2\,\mathrm{s}$.

Returning to the simulations where climate is varied via the longwave optical thickness, and using ϵ as estimated from the fixed-β simulations, we compute the second parameter $\gamma = (q_L - \epsilon E_L)/q_O$ for each simulation (except the warmest). We then calculate δq_L between pairs of nearest-neighbor simulations as a function of γ, ϵ, δq_O, and δE_L, where γ and ϵ are assumed to be constant as the climate changes.

The simulated and estimated changes in surface-air land specific humidity, along with the contributions due to changes in ocean humidity and land evapotranspiration [computed using (4.7)], are shown in Figure 4-8a. Quantitatively, the extended model is not as accurate as the original conceptual model, generally underestimating the q_L

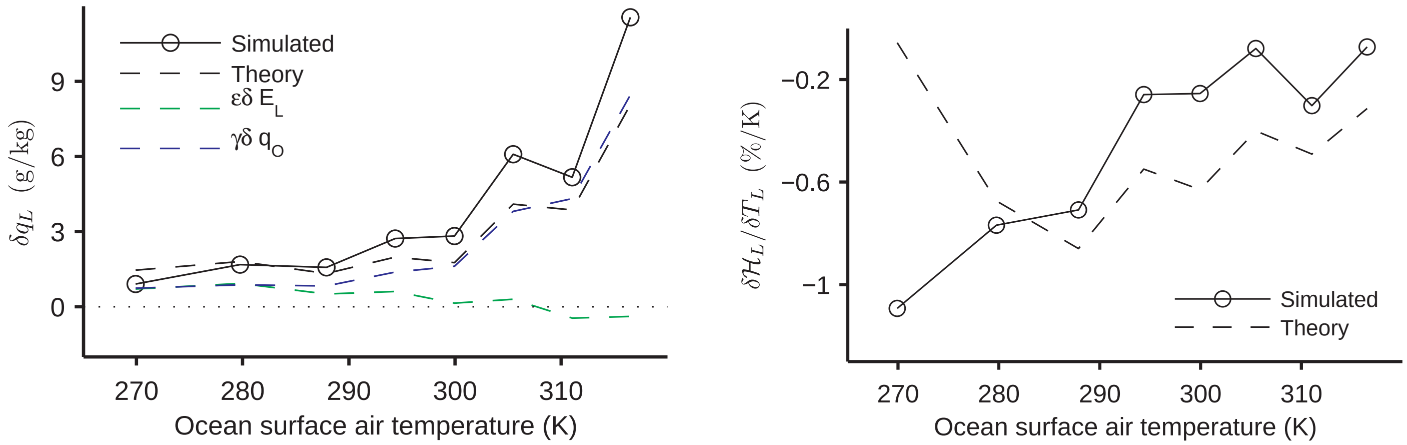

(a) Specific humidity changes over land

(b) Relative humidity changes over land

Figure 4-8: As in Figure 4-4, but here estimating the surface-air humidity changes using the extended model (4.7). The components of the estimated specific humidity changes due to ocean humidity changes ($\gamma\delta q_O$, blue dashed) and land evapotranspiration changes ($\epsilon\delta E_L$, green dashed) are also shown.

changes. The discrepancy is likely due to several effects, including variations in ϵ as the climate and soil moisture change (we use a single value of ϵ over the full range of climates). However, the qualitative behavior of δq_L as a function of temperature is captured by the extended model.

For the colder simulations, changes in q_O and E_L are roughly of equal importance, but the ocean humidity term dominates for temperatures above approximately 295K (Fig. 4-8a). The importance of the land evapotranspiration term at low temperatures is due to very large fractional increases in evapotranspiration between the first two pairs of simulations (17%/K and 7%/K, respectively). These large changes in E_L are related to greater increases in potential evaporation in colder climates because of the temperature dependence of the Clausius-Clapeyron relation (Scheff and Frierson, 2014). For the warmer simulations, fractional changes in E_L are much smaller ($\sim$2%/K) and closer in magnitude to those expected under present-day global warming (Stocker et al., 2013) and the changes in ocean specific humidity dominate the land humidity changes. The changes in simulated land relative humidity are not as well predicted by the extended model (Fig. 4-8b), partly due to the reasons mentioned above, for example different values of ϵ at low temperature. Nevertheless, our analysis and the simulations with specified evaporative fractions suggest a relatively weak influence of changes in land evapotranspiration on surface-air land humidity. We now investigate how land evapotranspiration changes under global warming contribute to relative humidity changes in the CMIP5 simulations.

The CMIP5 simulations and data we consider are as described in Section 4.2.3. As with the idealized GCM analysis, for the extended model (4.7) we need to estimate two parameters, γ and ϵ. However, there are no widely available CMIP5 runs analogous to the fixed-evaporative fraction simulations described above, and so we need to estimate the parameters using a different method. Using the intermodel scatter in ocean humidity and land evapotranspiration changes between the 19 CMIP5 models (changes are computed between the historical and RCP8.5 simulations, as before), we perform a multilinear regression to estimate γ and ϵ. For the regression, the land specific humidity change is the response variable and ocean specific humidity and land evapotranspiration changes are the predictor variables, i.e. $\delta q_L = \gamma \delta q_O + \epsilon \delta E_L$. The regression and the parameters, γ and ϵ, are computed at each latitude using zonally-averaged values of δq_O and δE_L. The magnitudes of γ and ϵ obtained using this regression are similar to the idealized GCM values. Given our method of estimating γ and ϵ, which requires knowledge of the changes in both ocean specific humidity and land evapotranspiration, the land specific humidity changes will be estimated exactly. Nevertheless, our purpose here is to understand the role of land evapotranspiration in relative humidity changes and in this context using a multilinear regression is appropriate.

At all latitudes, changes in surface-air land specific humidity are dominated by the $\gamma \delta q_O$ component (Fig. 4-9), emphasizing how the oceanic moisture source largely controls changes in land specific humidity. By construction, the extended model estimate matches the simulated multimodel-mean humidity response exactly; the intermodel scatter is captured to a similar extent as for the simple theory ($r = 0.67$, Fig. 4-10). The contribution due to land evapotranspiration changes, $\epsilon \delta E_L$, has a substantially smaller magnitude everywhere, though it is relatively more important in the Northern Hemisphere high latitudes. As discussed previously, there is a predominance of land

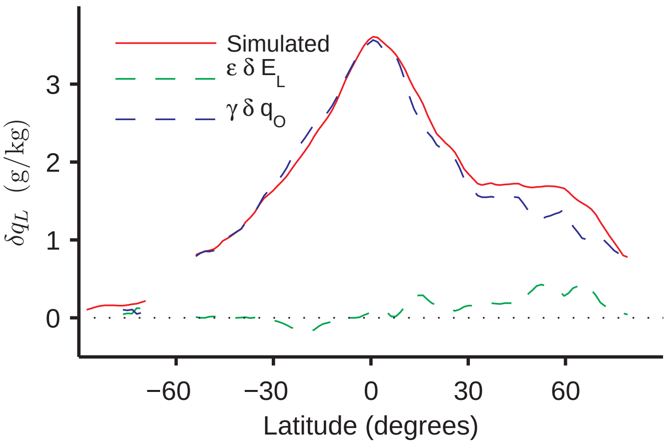

Figure 4-9: As in Figure 4-5a, but here estimating the multimodel-mean surface-air land specific humidity changes using the extended model (4.7). The components of the estimated specific humidity changes due to ocean humidity changes ($\gamma \delta q_O$, blue dashed) and land evapotranspiration changes ($\epsilon \delta E_L$, green dashed) are also shown. By construction, the simulated and estimated changes are exactly equal (solid red line). Unlike in Figure 4-5b, the changes in land relative humidity are not plotted as there is no straightforward way to partition the changes into ocean humidity and evapotranspiration components.

at these latitudes and so the oceanic influence in the continental interiors is likely to be reduced and changes in land evapotranspiration would potentially have a more important role in controlling the boundary layer humidity. Furthermore, land evapotranspiration increases at high latitudes are relatively large (Laîné et al., 2014), due to soil moistening and large increases in potential evaporation at colder temperatures (Scheff and Frierson, 2014). At lower latitudes the smaller increases in potential evaporation are often opposed by decreases in the surface exchange coefficient, due to soil drying and stomatal closure, resulting in small evapotranspiration changes. Thus, we would expect the influence of evapotranspiration on relative humidity changes to be larger at high latitudes (particularly in the Northern Hemisphere). Nevertheless, the role of evapotranspiration in determining land humidity changes is a second-order effect at all latitudes, supporting our simple hypothesis that the ratio of land to ocean specific humidities remains constant under climate change.

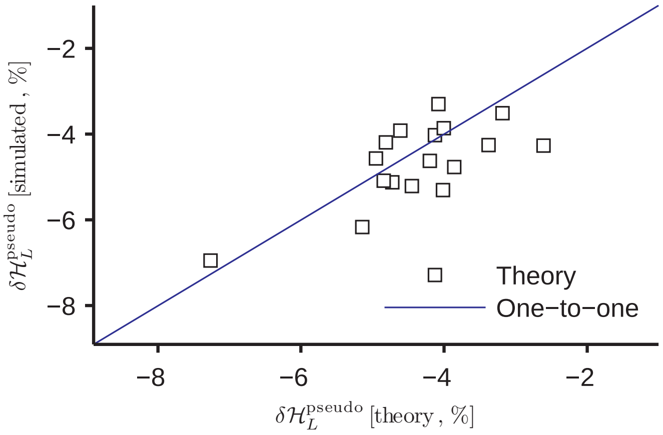

Figure 4-10: As in Figure 4-6, but here with simulated changes in surface-air land pseudo-relative humidity versus the estimates from the extended model (4.7). The correlation coefficient is $r = 0.67$.

4.4 Feedback between temperature and relative humidity changes

In this chapter, we have calculated changes in land relative humidity by estimating the specific humidity changes and then combining with the simulated temperature changes, which we have taken as given. As mentioned earlier and discussed in Chapters 2 and 3, however, there is a strong link between changes in temperature and relative humidity over land, and in practice both quantities change in tandem as the climate warms. A way to conceptualize the interaction of changes in temperature and relative humidity over land and ocean is using a feedback loop (Fig. 4-11): (i) In the basic-state climate, land is generally drier than ocean and so under warming, following the convective quasi-equilibrium theory of Byrne and O'Gorman (2013a,b), the land temperature increases more than the ocean temperature (even without a land relative humidity decrease). (ii) Following the conceptual model for δq_L derived above, this enhanced land warming leads to a land relative humidity drop, which in turn (iii) enhances the land warming further. This feedback loop cannot continue indefinitely, as continually increasing the land temperature and decreasing the relative humidity (all else constant) would continually increase the longwave, sensible, and latent heat fluxes from the land surface, eventually violating the surface energy and

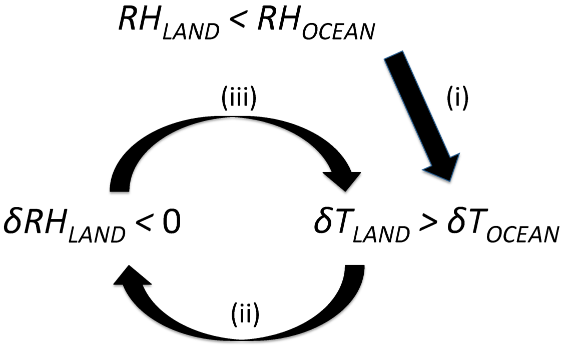

Figure 4-11: Schematic diagram describing the feedback between changes in temperature and relative humidity over land and ocean.

water balances.

4.5 Conclusions

We have introduced a conceptual model to understand the future response of surface-air land relative humidity to global warming. This follows Rowell and Jones (2006), O'Gorman and Muller (2010), and others, who suggested an oceanic control on land humidity changes. By considering the moisture balance of the land surface-air layer we derived a simple expression for changes in land specific humidity: $\delta q_L = \gamma \delta q_O$. This simple model suggests that as the climate changes, the ratio of land to ocean specific humidity stays approximately constant. Applying the conceptual model to idealized and CMIP5 simulations, and combining the estimated changes in specific humidity with the given land temperature changes, we have found that the model performs well and successfully captures the land relative humidity decreases to first order.

If evapotranspiration from the land surface is assumed to be entirely dependent on atmospheric humidity, then the influence of changes in evapotranspiration on land humidity can be accounted for simply by modifying the parameter γ in our conceptual model. However, evapotranspiration depends on a multitude of factors, including soil moisture and vegetation type, and changes in these surface properties have been shown to change land relative humidity independent of changes in ocean humidity. To understand how changes in evapotranspiration contribute to land relative humidity decreases under warming, we have derived an extended conceptual model which includes an additional term: $\delta q_L = \gamma \delta q_O + \epsilon \delta E_L$. Again using idealized and CMIP5 simulations, we have found that the $\epsilon \delta E_L$ term is generally negligible for realistic changes in land evapotranspiration and that changes in land humidity are primarily tied to the moisture import from the ocean. However, intermodel differences in the modeling of land surfaces and evapotranspiration, emphasized by the highly divergent projections of how soil moisture changes with warming, are likely to explain part of the intermodel scatter in the land relative humidity changes, if not the mean magnitude of the changes.

Future work could isolate the roles of changing land-surface properties (e.g., soil moisture, stomatal conductance) versus changes in potential evaporation in controlling land relative humidity, perhaps using additional idealized GCM simulations and/or a mechanistic analysis of changes in evapotranspiration in CMIP5 models, following Laîné et al. (2014). Finally, it would be interesting to assess the ability of the conceptual models discussed here to explain observed trends in land relative humidity, particularly the sharp decrease in land relative humidity between 2000 and 2008 (Simmons et al., 2010).

Chapter 5

The terrestrial water cycle under global warming

5.1 Introduction

The Earth's water cycle is expected to change substantially as the climate warms, impacting societies, economies and ecosystems throughout the world (Stocker et al., 2013; Field et al., 2014). However, despite increases in the resolution and sophistication of climate models, the water cycle response to global warming remains highly uncertain, particularly at the regional scale (e.g., Knutti and Sedláček, 2013). This uncertainty reflects a lack of understanding of the physical processes controlling the water cycle. As might be expected, observed and projected changes in the water cycle are markedly different over land and ocean regions (Roderick et al., 2014) because of different surface water availability. This chapter investigates the projected response of the water cycle to future global warming, with a focus on developing a simple theory for changes in precipitation minus evaporation ($P - E$) that applies over both land and ocean. Our aim is to improve our understanding of changes in the water cycle over land.

At the global scale, changes in the water cycle are strongly constrained by energy and water budgets. For example, in steady state, globally-averaged precipitation increases at approximately 2%/K and is tied to changes in the radiative cooling of

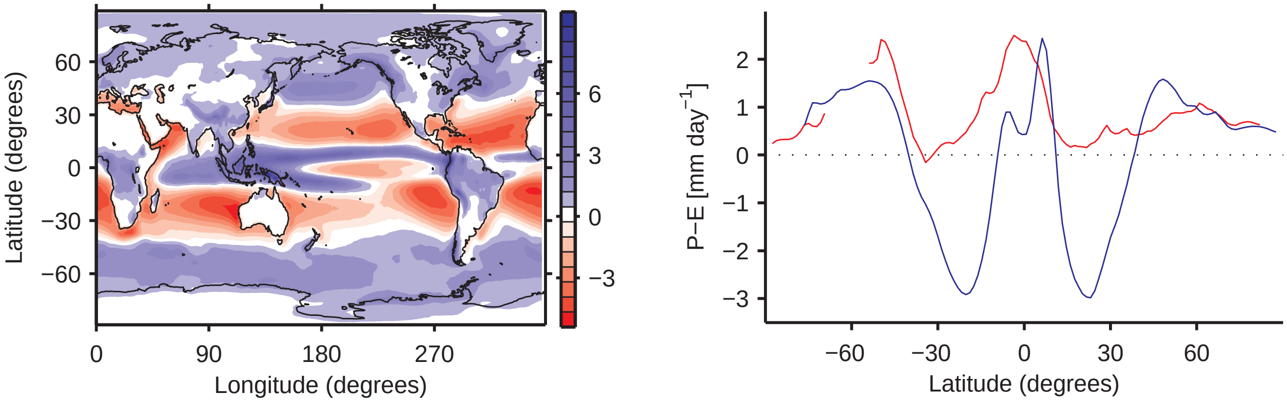

(a) Multimodel-mean $P - E$ (b) Zonal-mean $P - E$

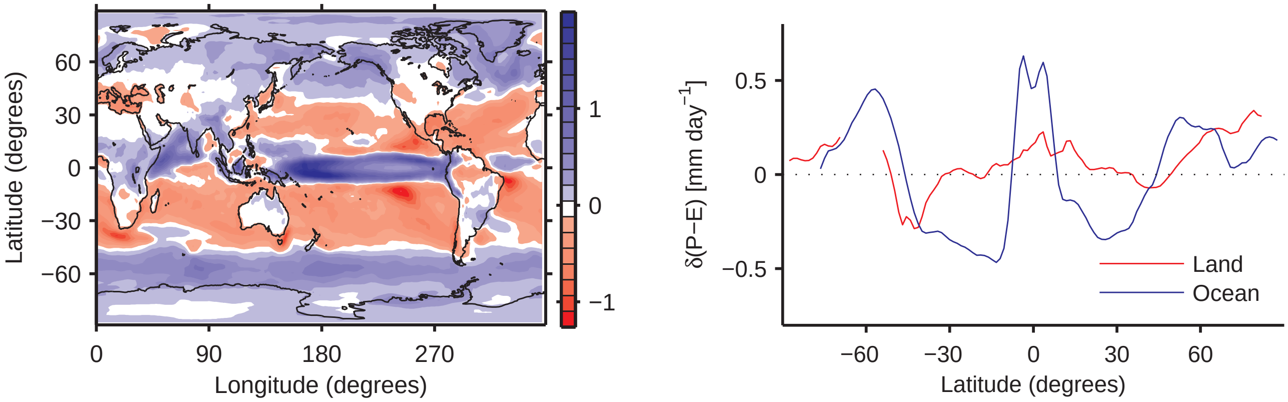

(c) Multimodel-mean $\delta(P - E)$ (d) Zonal-mean $\delta(P - E)$

Figure 5-1: [(a) and (b)] Multimodel-mean precipitation minus evaporation $(P - E)$ in the historical (1976-2005) simulations, and [(c) and (d)] multimodel-mean changes in $P - E$ between the historical (1976-2005) and RCP8.5 (2070-2099) simulations. For (b) and (d), the blue and red lines represent zonal averages over ocean and land regions, respectively. All quantities are expressed in units of millimeters per day.

the atmosphere (Allen and Ingram, 2002; Takahashi, 2009; O'Gorman et al., 2012). However, predicting how this radiative cooling will change with climate is non-trivial given uncertainties in cloud and aerosol processes, and so there remain differences in the response of global-mean precipitation amongst climate models (Hawkins and Sutton, 2011). Changes in precipitation must be balanced by changes in evaporation in order to obey global surface water balance, and so the radiative cooling constraint is one way to conceptually understand changes in evaporation.

Another key water cycle variable is the difference between precipitation and evaporation, $P - E$, which is directly related to the moisture budget of the atmosphere (e.g., Held and Soden, 2006). This is the water cycle metric which we shall focus on throughout this chapter. The strength of the water cycle is often quantified by $P - E$, which, when averaged over long time periods, is equal to the net freshwater flux into the surface. The salinity of the oceanic mixed-layer is closely tied to the local $P-E$, and over land $P-E$ is balanced by surface and sub-surface runoff and so it is an important quantity for agriculture, water management, and inland fisheries. Given that precipitation and evaporation are equal in the global- and time-mean, it is trivial to infer that changes in $P - E$ must globally average to zero under changes in climate. However, there is no such constraint on regional $P-E$ changes (or indeed on P or E locally), which may be positive, negative or zero depending on how the atmospheric circulation and humidity field respond to climate change (Seager et al., 2010). Understanding the regional response of the water cycle to climate change is a key task for contemporary climate science, given that it is at the regional scale and particularly over land where the impacts of climate change are most critical.

Before discussing its projected changes, it is useful to assess $P - E$ in simulations of the present-day climate (Figs. 5-1a and 5-1b): Over ocean, the climatological $P - E$ field varies strongly meridionally, with net precipitation ($P - E > 0$) in the tropics and extratropics, and net evaporation ($P - E < 0$) in the subtropics. The atmosphere exports moisture from the subtropics to lower and higher latutudes via the time-mean Hadley cells, and via stationary and transient eddies (Peixóto and Oort, 1984). Over land, $P - E$ has a similar latitudinal structure; net precipitation in the deep tropics and at higher latitudes. However, unlike the ocean, there is a limited amount of water that can be evaporated from a land surface. Thus, $P - E$ averaged over a drainage basin is constrained to be greater than or equal to zero in the time-mean. Land in the arid subtropics approaches the $P - E = 0$ limit, though in the global-mean over all land regions there is net runoff (i.e., a net atmospheric transport of water from ocean to land).

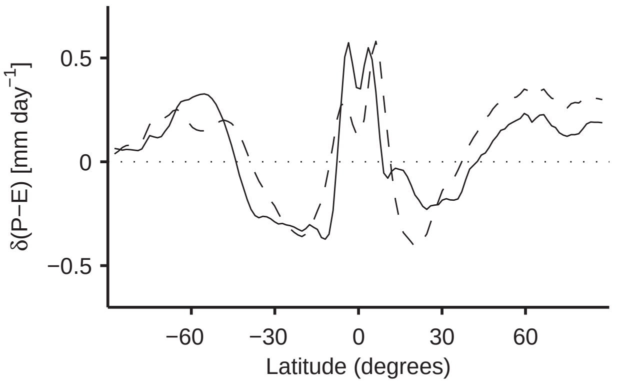

(a) Global

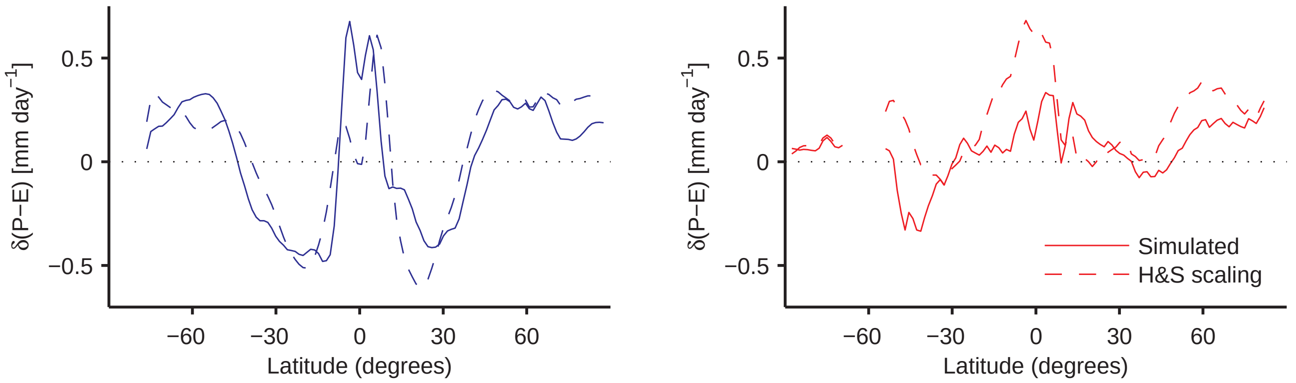

(b) Ocean

(c) Land

Figure 5-2: Multimodel-mean changes in zonal-mean $P-E$ averaged (a) globally, (b) over oceans, and (c) over land. Solid lines show the simulated changes and dashed lines are the estimates from the Held and Soden scaling (5.1). Here and in subsequent figures, "simulated" means $P-E$ changes calculated using the time-mean atmospheric moisture budget [see Eqn. (5.7)].

5.1.1 The "rich-get-richer" paradigm

In addition to the land-ocean contrast in the present day water cycle, observations indicate strikingly different responses of land and ocean $P - E$ to global warming over recent decades. Analysis of sea-surface salinity measurements from 1950-2000 shows an intensification of $8 \pm 5\%$/K of the oceanic water cycle (Durack et al., 2012), but there are no significant trends over land as estimated using streamflow data from 1948-2004 (Dai et al., 2009). Model simulations of future climate change also show a pronounced land-ocean contrast in the $P-E$ response, with smaller magitude changes over land in comparison to ocean regions at similar latitudes (Figs. 5-1c and 5-1d).

The ocean response to global warming has a latitudinal structure which strongly resembles the climatological $P-E$: Regions of positive $P-E$ tend to become wetter as the climate warms [$\delta(P-E) > 0$] and negative $P-E$ regions tend to become drier [$\delta(P-E) < 0$]. This "wet-get-wetter, dry-get-drier" response, also known as the "rich-get-richer" effect, is a simple consequence of increasing atmospheric water vapor transport in a warming climate, following the Clausius-Clapeyron relation (Mitchell et al., 1987; Chou and Neelin, 2004; Held and Soden, 2006) [it should be noted, however, that climate models underestimate the observed intensification of the water cycle over ocean by a factor of roughly 2 (Durack et al., 2012)]. This hypothesis of the water cycle intensifying under global warming was formalized by Held and Soden (2006), who derived the following expression for changes in $P-E$:

$$\delta(P-E) = \alpha\delta T_S(P-E), \tag{5.1}$$

where α is a temperature-dependent parameter, derived from the Clausius-Clapeyron relation and chosen by Held and Soden to be $\alpha = 7\,\%/\mathrm{K}$, and δT_S is the local surface-air temperature change. To derive (5.1), Held and Soden assumed: Negligible changes in the atmospheric circulation under climate change, negligible changes in relative humidity, more meridional structure in climatological $P-E$ than in δT_S, and that the vertically-integrated moisture flux scales with the lower-tropospheric moisture content. We will return to these assumptions later in our derivation of an extended scaling for $P-E$.

Under global warming, this simple thermodynamic scaling (5.1) predicts an enhancement of climatological $P-E$ at a rate of 7%/K. The scaling also qualitatively captures the projected response of zonal-mean $P-E$ in climate model simulations of global warming (Held and Soden, 2006, and Fig. 5-2a). However, when (5.1) is applied over land and ocean regions separately, its limitations become apparent.

Over ocean, the behavior is analogous to the global average, with the simple scaling capturing the simulated response qualitatively (Fig. 5-2b). Over land, the scaling fails to capture the projected $P-E$ changes (Roderick et al., 2014). The

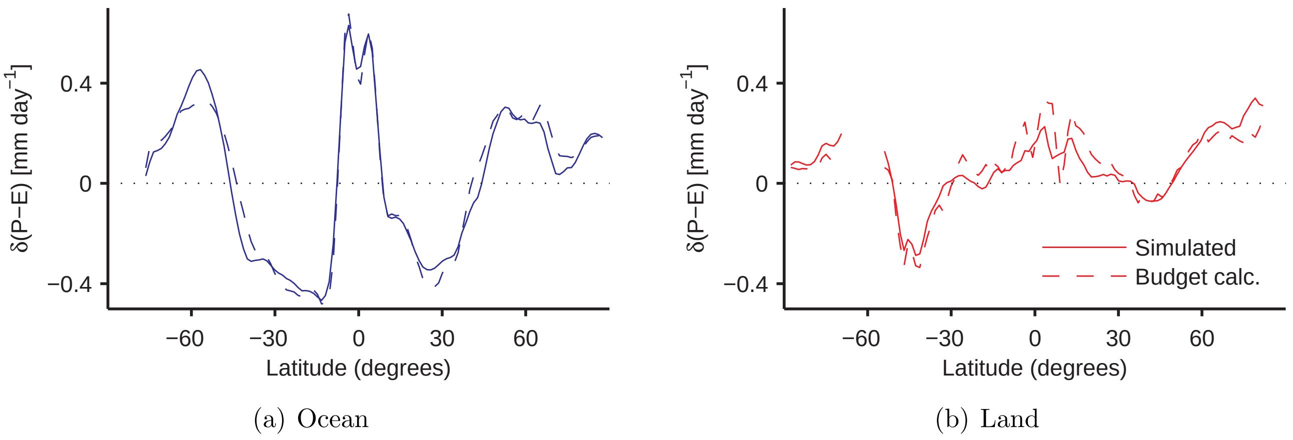

(a) Ocean (b) Land

Figure 5-3: Multimodel-mean simulated changes in zonal-mean $P - E$ averaged (a) over oceans and (b) over land (solid lines), along with $P - E$ changes as estimated from the atmospheric moisture budget [dashed lines, see Eqn. (5.7)].

scaling predicts a strong moistening over land at most latitudes (Fig. 5-2c). However, simulations show only a weak moistening at a rate substantially smaller than the 7%/K predicted by (5.1), and even show drying in regions such as southwestern North America (Seager and Vecchi, 2010) and the Mediterranean (Seager et al., 2014a). A recent observational analysis has further shown that the "rich-get-richer" scaling does not explain trends in the terrestrial water cycle over recent decades (Greve et al., 2014).

Studies of regional climate change have suggested a variety of physical processes, not accounted for in the simple scaling, which may influence $P - E$ changes in various land regions. Changes in the atmospheric circulation and spatial temperature gradients under warming have been shown to be important drying mechanisms in certain continental regions (Seager et al., 2010, 2014a,b); relative humidity reductions decrease land precipitation in the tropics (Chadwick et al., 2013); a poleward shift of the storm tracks under warming tends to dry regions on the subtropical edge of the midlatitudes (Scheff and Frierson, 2012) and moisten regions on the poleward edge. However, the systematic discrepancy between the thermodynamic scaling and the model projections over land, with climate models simulating global-mean $P - E$ changes over land that are substantially smaller than 7%/K, suggests there may be fundamental mechanisms retarding the response of the terrestrial water cycle to global warming. These mechanisms could be missed when studying regional changes in isolation.

5.1.2 Outline of chapter

In this chapter we use CMIP5 simulations to analyze changes in $P - E$ over all land regions with the objective of isolating the processes that cause a muted response relative to the simple thermodynamic scaling. Analysis of simulations allows for a detailed atmospheric moisture budget decomposition and subsequent identification of mechanisms leading to changes in $P - E$. Performing a similar analysis with observations would be difficult because reliable long-term and spatially homogeneous precipitation and evaporation measurements are often lacking (e.g., Adler et al., 2001; Trenberth et al., 2011), particularly over land (Kalma et al., 2008).

The questions we will address are as follows: Why does the "rich-get-richer" mechanism hold to a lesser extent over land than ocean? In particular, which physical processes, neglected in the derivation of the simple scaling (5.1), are important over land? Can an extended scaling be derived which captures the response over both land and ocean? We begin by describing the simulation data used and the details of the moisture budget decomposition (Section 5.2), before discussing the contrasting changes in $P - E$ over land and ocean in the simulations and identifying the physical processes leading to the changes (Section 5.3). We then derive and apply an extended scaling for $P - E$ changes over land, similar to that used by Boos (2012), and outline the mechanisms which robustly dry the land relative to the simpler scaling (Section 5.4). Finally, we summarize our results and give an outlook for future work (Section 5.6).

5.2 Data and Methods

We analyze simulated changes in $P - E$ from ten CMIP5 models[1]. The climate change we consider is the difference between 30-year time averages in the historical simulations (1976-2005) and the RCP8.5 simulations (2070-2099). For each simulation, we use the r1i1p1 ensemble member (Taylor et al., 2012). The models analyzed represent those for which all the data required for the atmospheric moisture budget decomposition were publicly available at the time of analysis.

We perform a decomposition of the atmospheric moisture budget in order to identify the mechanisms leading to changes in $P - E$ under global warming. Our method of decomposition is similar to that of Seager et al. (2010). In the time-mean, the tendency of the moisture content of the atmosphere can be neglected, and the convergence of the horizontal moisture flux in the atmosphere is balanced by the net water flux into the surface:

$$P - E = -\nabla \cdot \mathbf{F} = -\nabla \cdot [\mathbf{u}q], \tag{5.2}$$

where $\mathbf{F}$ is the mass-weighted, vertically-integrated, horizontal atmospheric moisture flux, $\mathbf{u} = (u, v)$ is the horizontal wind vector, q is the specific humidity, and $[\cdot] \equiv (1/g) \int_0^{p_S} (\cdot) dp$ represents a mass-weighted, vertical integral over the depth of the atmosphere (g is the gravitational acceleration, and p_S is the surface pressure). Following (5.2), time-mean changes in $P - E$ are equal to the changes in the moisture flux convergence:

$$\delta(P - E) = -\nabla \cdot \delta([\mathbf{u}q]). \tag{5.3}$$

Defining climatological monthly means with overbars $\overline{(\cdot)}$ and departures from climatological monthly means with primes $(\cdot)'$, e.g. $\mathbf{u} = \overline{\mathbf{u}} + \mathbf{u}'$, we can divide $P - E$ and its changes into a component due to changes in the monthly-mean winds and humidity, and a component due to changes in transient eddies:

---

[1] The models used are: BCC-CSM1-1, BCC-CSM1-1-M, BNU-ESM, CNRM-CM5, IPSL-CM5A-LR, MIROC5, MIROC-ESM, MIROC-ESM-CHEM, MRI-CGCM3, MRI-ESM1.

$$P - E = -\nabla \cdot [(\overline{\mathbf{u}} + \mathbf{u}')(\overline{q} + q')] \tag{5.4}$$

$$\Rightarrow \overline{P - E} = -\nabla \cdot [\overline{\mathbf{u}}\overline{q}] - \nabla \cdot [\overline{\mathbf{u}'q'}] \tag{5.5}$$

$$\Rightarrow \delta(\overline{P - E}) = -\nabla \cdot \delta([\overline{\mathbf{u}}\overline{q}]) - \nabla \cdot \delta([\overline{\mathbf{u}'q'}]). \tag{5.6}$$

Following Seager et al. (2010), we can futher divide the mean component of $\delta(\overline{P - E})$ into a mean thermodynamic part, δMTh, involving changes in mean specific humidity with fixed mean winds, and a mean dynamic part, $\delta MDyn$, representing the contribution from changes in mean winds with a fixed humidity field. The moisture convergence by transient eddies, $\delta Eddy$, is a covariance term and so it is not straightforward to divide it into thermodynamic and dynamic components [though Wu et al. (2011) have attempted such a decomposition for the moist static energy flux using mixing length theory]. There is also a nonlinear term, δNL, involving the product of changes in the mean wind and humidity fields:

$$\delta(\overline{P - E}) = \underbrace{-\nabla \cdot [\overline{\mathbf{u}}\delta(\overline{q})]}_{\delta MTh} \underbrace{-\nabla \cdot [\delta(\overline{\mathbf{u}})\overline{q}]}_{\delta MDyn} \underbrace{-\nabla \cdot \delta([\overline{\mathbf{u}'q'}])}_{\delta Eddy} \underbrace{-\nabla \cdot [\delta(\overline{\mathbf{u}})\delta(\overline{q})]}_{\delta NL}. \tag{5.7}$$

For convenience, from now on we drop the overbars when referring to time-mean $P - E$ or its changes. Unlike Seager et al. (2010), who found the nonlinear term to have negligible magnitude (see their Fig. 12), it turns out to be a substantial contributor to the $P - E$ changes here, particularly over land, and is thus retained in our analysis. The more substantial changes in climate considered here may explain the larger magnitude of our nonlinear term [the RCP8.5 scenario leads to a global-mean temperature increase of roughly 4°C by the end of this century, versus less than 3°C of warming in the SRESA1B scenario analyzed by Seager et al. (2010)].

To calculate the mean thermodynamic, dynamic, and nonlinear components of (5.7) we use monthly-mean air and surface-air winds and specific humidities. The transient eddy term is calculated explicitly using daily data[2]. The vertical integral of a given field through the atmosphere is evaluated by linearly interpolating to estimate the field's values at the midpoints between the model's pressure levels, multiplying by the pressure difference between the levels, and then summing over all pressure levels (we use the surface-air layer as an extra level for the vertical integral). The divergences are calculated by taking derivatives of spline interpolations of the given field in the zonal and meridional directions. The calculation of $\delta(P-E)$ from the moisture budget [right side of (5.7)] matches the simulated $\delta(P-E)$ [left side of (5.7)] to a very good approximation over oceans (Fig. 5-3a). Over land (Fig. 5-3b), the budget is somewhat less accurate, which is likely due to difficulties in calculating divergences in regions of topography, and also due to our discretization method being different to that of each individual model, as noted by Seager et al. (2010).

---

[2] For reference, the variables used in this chapter have the following names in the CMIP5 archive:

5.3 Contributions to $\delta(P-E)$: A moisture budget decomposition

The first step towards understanding the simulated changes in $P-E$ over land under global warming is to perform the atmospheric moisture budget decomposition described by (5.7). We calculate the mean thermodynamic, mean dynamic, transient eddy, and nonlinear contributions at each model gridpoint before zonally averaging over land and ocean separately. By comparing land to ocean in this way, the processes leading to the different behaviors of the water cycle can be clearly identified.

5.3.1 Ocean components

The four components of changes in ocean $P-E$ are plotted individually in Figure 5-4. Many features of the total simulated $P-E$ response to warming are contained in the mean thermodynamic term (Fig. 5-4a): Enhanced $P-E$ in the Intertropical Convergence Zone (ITCZ), drying of the subtropics, and some moistening of the

---

Precipitation (*pr*), evaporation (*evspsbl*), air and surface-air eastward wind (*ua* and *uas*, respectively), air and surface-air northward wind (*va* and *vas*, respectively), air and surface-air specific humidity (*hus* and *huss*, respectively), surface-air temperature (*tas*), surface-air relative humidity (*hurs*), and atmosphere water vapor content (*prw*).

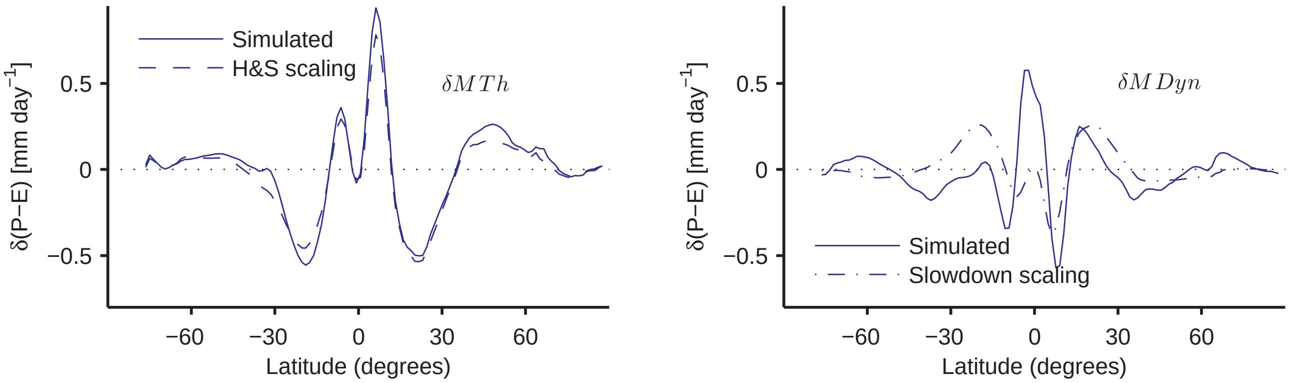

(a) Mean thermodynamic component (b) Mean dynamic component

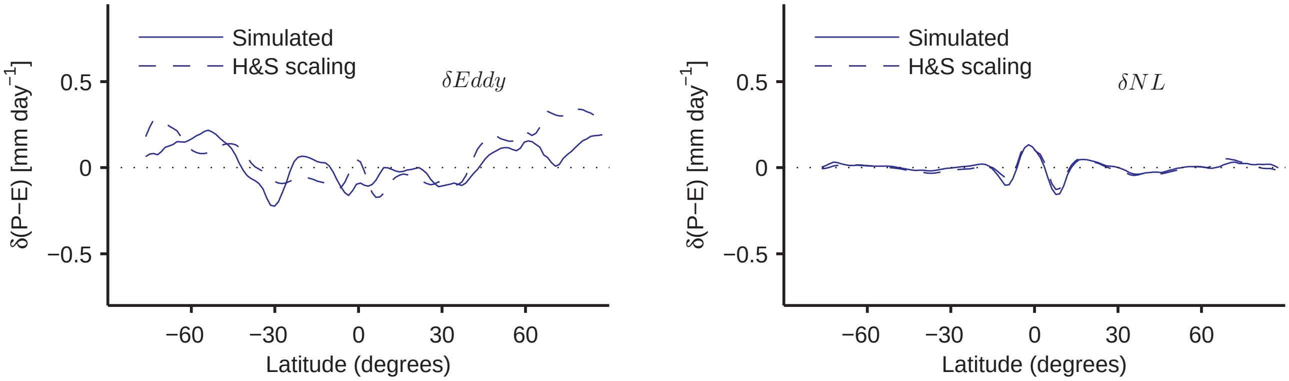

(c) Transient eddy component (d) Nonlinear component

Figure 5-4: Contributions to changes in ocean $P - E$ from (a) the mean thermodynamic component, (b) the mean dynamic component, (c) the transient eddy component, and (d) the nonlinear component [the various terms are defined by Eqn. (5.7)]. Solid lines denote the simulated changes, dashed lines are the estimates from the Held and Soden scaling [Eqns. (5.1) and (5.9)], and the dashed-dotted line is the "slowdown scaling" as defined by (5.8).

midlatitudes (particularly in the Northern Hemisphere). The mean dynamic term is also important, especially at lower latitudes (Fig. 5-4b). A southward shift of the ITCZ is evident, as found previously in simulations of historical (Hwang et al., 2013) and future warming (Seager et al., 2010; Frierson and Hwang, 2012). There is also a general slowdown of the tropical circulation (Vecchi and Soden, 2007), which tends to dry regions of climatological moisture convergence and moisten regions of moisture divergence, counteracting to some degree the thermodynamic "rich-get-richer" effect. The mean dynamic term also shows drying on the midlatitude edge of the subtropics due to a poleward expansion of the Hadley cell under global warming (Lu et al., 2007;

Scheff and Frierson, 2012).

To qualitatively estimate the extent to which the mean dynamic component is a slowdown of the mean circulation versus a latitudinal shift, we scale the basic-state mean component of $P - E$ by negative 10% and compare to the simulated $\delta MDyn$ component (Fig. 5.3b):

$$(\delta MDyn)_{\mathrm{Slowdown}} \equiv (-0.1) \times (-\nabla \cdot [\overline{\mathbf{u}}\overline{q}]). \tag{5.8}$$

Scaling by 10% is somewhat arbitrary[3]; we simply want to check if $\delta MDyn$ can be approximated as a scaled version of the basic-state mean component of $P - E$. This "slowdown scaling" (5.8) does capture part of the structure of $\delta MDyn$, including the moistening of the Northern Hemisphere subtropics and drying of the northern branch of the ITCZ (Fig. 5-4b). However, other features of $\delta MDyn$, such as the strong moistening directly on the equator, cannot be explained as a simple slowdown but rather involve a latitudinal shift (likely in addition to a slowdown).

The transient eddy contribution to ocean $\delta(P - E)$ is small near the equator, becoming more important further poleward (Fig. 5-4c) as one would expect given the moisture transport by transient eddies peaks in midlatitudes (e.g., Peixóto and Oort, 1984). The latitudinal structure of $\delta Eddy$ is also as expected, with enhanced drying of the subtropics and moistening of higher latitudes under warming (i.e., increased moisture transport by a fixed circulation). A poleward shift of the eddies and their moisture transport is difficult to identify clearly in Figure 5-4c, but it has been noted in previous studies (Yin, 2005; Seager et al., 2010).

To gain further insight into the processes leading to changes in ocean $P - E$, we apply the Held and Soden scaling (5.1) to the mean thermodynamic and transient eddy terms individually (the scaling is thermodynamic and so cannot be applied to the mean dynamic component). Our motivation is that the $\delta MTh = -\nabla \cdot [\overline{\mathbf{u}}\delta(\overline{q})]$ term incorporates all simulated changes in the mean specific humidity field under warming, including changes in saturation specific humidity, relative humidity, horizontal temperature gradients, and in the vertical structure of humidity. The latter three effects are not included in the Held and Soden scaling yet we would like to know their influence on the simulated $P - E$ changes. To test this, we estimate δMTh by applying the Held and Soden scaling to just the mean component of the basic-state ocean $P - E$, i.e. $(\delta MTh)_{H\&S} \equiv -\alpha\delta T_S \nabla \cdot [\overline{\mathbf{u}}\overline{q}]$. Comparing the solid and dashed lines in Figure 5-4a, we find that this simple estimate matches the simulated δMTh at all latitudes, showing that changes in relative humidity, horizontal temperature gradients, and in the vertical structure of humidity have little influence on $P - E$ over ocean. Expressed another way, the thermodynamic changes in ocean $P - E$ can be entirely captured by scaling the climatological mean component with surface-air temperature at the Clausius-Clapeyron rate of 7%/K.

---

[3] Held and Soden (2006) reasoned that given specific humidity increases at approximately 7%/K under warming but precipitation increases only at 2%/K, a circulation slowdown of 5%/K is required in order for the atmospheric water budget to be satisfied (assuming a precipitation model of $P = Mq$, where M is a vertical mass flux). In this framework, our hypothesized 10% reduction in circulation strength would correspond to a global-mean temperature change of 2K (though the temperature change in the RCP8.5 simulations considered here is more like 4°C).

We also estimate the transient eddy component using the Held and Soden scaling, i.e. $(\delta Eddy)_{H\&S} \equiv -\alpha\delta T_S \nabla \cdot [\overline{\mathbf{u}'q'}]$. As noted previously, the transient eddy term includes contributions from both changes in the eddy dynamics and changes in the humidity statistics, and so we would not expect a purely thermodynamic scaling to explain the simulated changes precisely. Nevertheless, the simple scaling gives a reasonable approximation to the simulated $\delta Eddy$ (Fig. 5-4c), predicting the gross latitudinal structure (e.g., subtropical drying, high-latitude moistening). However, it is unable to capture features such as the poleward shift of the storm tracks which are important for regional climate change impacts. Note that the poleward bias of the Held and Soden scaling relative to the simulated $\delta Eddy$ is evidence of this poleward shift; see the solid and dashed lines in Figure 5-4c.

The nonlinear term, δNL, is entirely negligible outside the tropics but near the equator it has a similar moistening/drying structure to the mean dynamic component (i.e., moistening on the equator and drying just off the equator), albeit with a substantially smaller magnitude. Again applying the Held and Soden scaling, δNL

can be approximated as:

$$\delta NL = -\nabla \cdot [\delta(\overline{\mathbf{u}})\delta(\overline{q})] \approx -\alpha \delta T_S \nabla \cdot [\delta(\overline{\mathbf{u}})\overline{q}] = \alpha \delta T_S \times \delta MDyn. \tag{5.9}$$

Testing (5.9) versus the simulated nonlinear component, we find that it is an excellent approximation over ocean (Fig. 5-4d), showing that the nonlinear component of $\delta(P-E)$ is simply a scaled-down version of the mean dynamic component (this scaling of the nonlinear component has not been demonstrated previously, to our knowledge).

5.3.2 Land components

Despite the simplicity of the Held and Soden scaling (only the climatological $P-E$ field and the local surface-air temperature changes are required), it is remarkably successful at estimating the basic structure and magnitude of $\delta(P-E)$ over ocean. Over land, however, where a mechanistic understanding of the response of the water cycle is arguably more critical, the simple scaling fails to capture important features, such as a projected drying over North America (Seager and Vecchi, 2010) and southern Europe (Seager et al., 2014a), and also robustly overestimates the land moistening at almost every latitude (Fig. 5-2c).

To account for these discrepancies between the simple scaling and simulated response over land, and to guide our development of a more useful scaling for land $P-E$, we examine the components of the moisture budget decomposition over land (Fig. 5-5). The mean thermodynamic component is qualitatively similar to that over ocean, with moistening of the tropics and drying of the subtropics (Fig. 5-5a), although the response is more hemispherically asymmetric than over ocean. The mean dynamic term is more hemispherically symmetric than over the ocean, with tropical drying and subtropical moistening that appears to be the result of both a weakening and a latitudinal shift of the mean circulation (Fig. 5-5b). As over ocean, the transient eddy component tends to enhance moisture transports from the subtropics to higher latitudes and generally has a small magnitude (Fig. 5-5c), though the South-

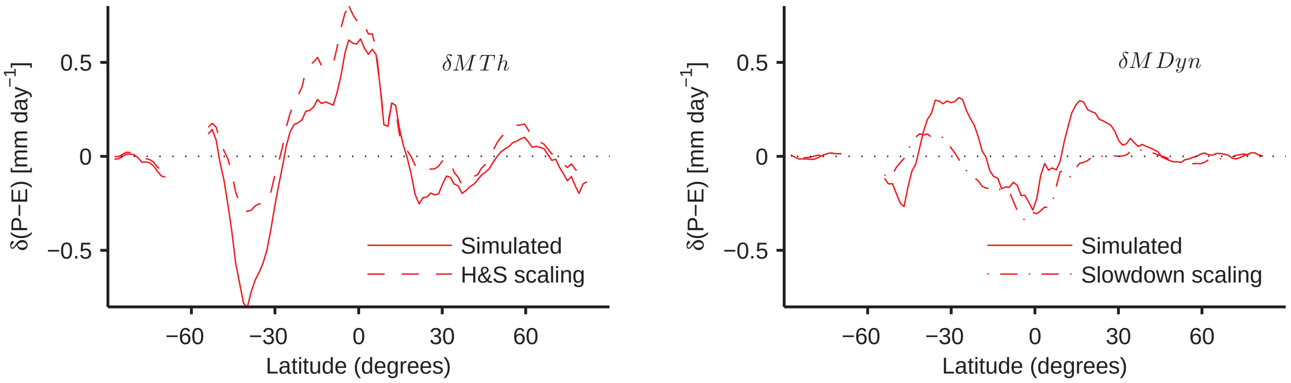

(a) Mean thermodynamic component (b) Mean dynamic component

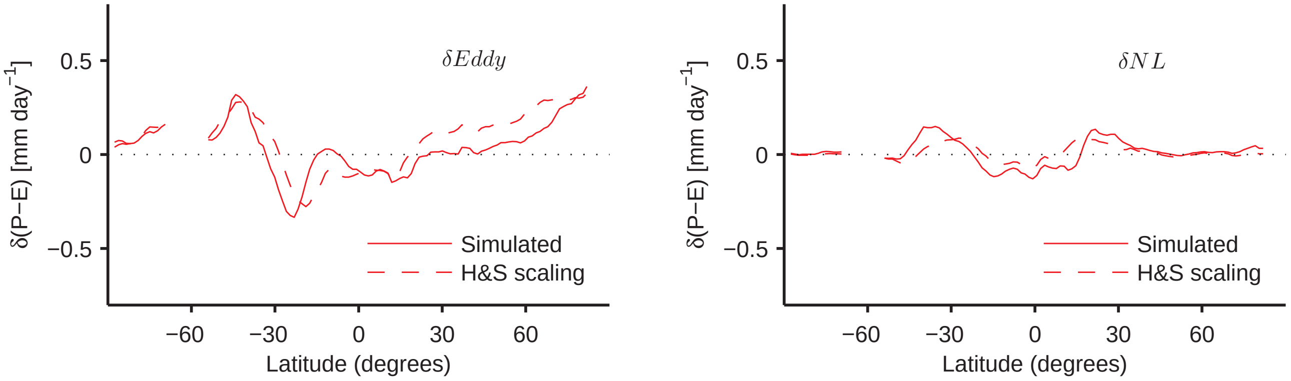

(c) Transient eddy component (d) Nonlinear component

Figure 5-5: As in Figure 5-4, but for the land components.

ern Hemisphere subtropics and northern high latitudes are exceptions. Also, as over ocean, comparing the Held and Soden estimate of the transient eddy term with the simulated response (cf. solid and dashed lines in Fig. 5-5c) a poleward shift in the eddies is evident. Applying the Held and Soden scaling of the nonlinear component (5.9) to land, we find it approximates the simulated term qualitatively (Fig. 5-5d).

For the mean thermodynamic component we see that, unlike for the ocean, the Held and Soden scaling cannot accurately capture the simulated response (Fig. 5-5a). In regions where the simulated δMTh is moistening the land (e.g., the tropics), the scaling overestimates the moistening, and where there is drying the scaling underestimates the magnitude of that drying. The lack of agreement between the simple scaling and simulations suggests that changes in either relative humidity, horizontal temperature gradients, or the vertical humidity structure are important for the

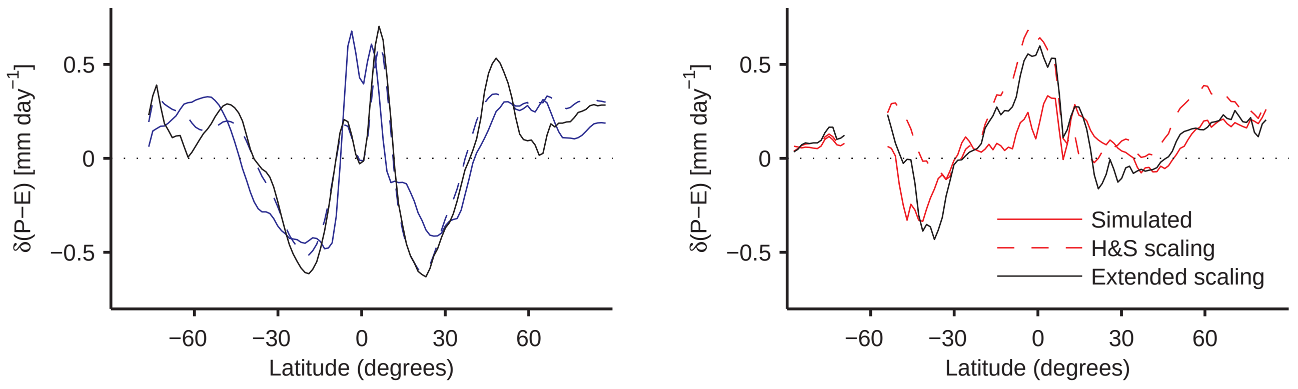

(a) Ocean (b) Land

Figure 5-6: As in Figure 5-2, but including the estimates of changes in $P - E$ using the extended scaling (5.11) (black solid lines).

δMTh response over land but not ocean (this will be discussed in more detail in Section 5.4). For the transient eddy contribution, the simple scaling also overestimates the moistening at many latitudes, for example throughout the Northern Hemisphere midlatitudes (Fig. 5-5c). Although the estimates of δMTh and $\delta Eddy$ by the Held and Soden scaling qualitatively resemble the simulated components, for the full $P - E$ response the scaling robustly overestimates the land moistening and does not capture projected drying (Fig. 5-2c).

The “rich-get-richer” paradigm is commonly invoked to describe projected changes in the water cycle under global warming, both in the climate science community and to more general audiences. Yet, as demonstrated here and elsewhere (Roderick et al., 2014), the paradigm is not valid for land regions. To address this, we now derive an extended version of the Held and Soden scaling to more accurately capture the simulated water cycle projections over land and to improve our mechanistic understanding of changes in the terrestrial water cycle.

5.4 An extended scaling for $\delta(P-E)$ over land

5.4.1 Derivation

As with the original Held and Soden scaling, the starting point for the derivation of the extended scaling is the atmospheric moisture budget: In steady state, changes in atmospheric moisture convergence are balanced by changes in $P-E$, i.e. $\delta(P-E) = -\nabla \cdot \delta\mathbf{F}$. Before deriving the extended scaling, we quickly review the simple scaling.

Held and Soden assumed that changes in the vertically-integrated moisture flux, $\mathbf{F}$, under global warming are dominated by changes in lower-tropospheric moisture (rather than by changes in winds), i.e. $\delta\mathbf{F}/\mathbf{F} \approx \delta e/e \approx \delta q/q$, where e and q are the lower-tropospheric vapor pressure and specific humidity, respectively[4]. Assuming fixed relative humidity, using the Clausius-Clapeyron expression for saturation vapor pressure and the surface-air temperature change as representative of the change over the lower troposphere for simplicity, the above relation becomes $\delta\mathbf{F}/\mathbf{F} \approx \alpha(T)\delta T_S$, where $\alpha(T) = L/RT^2$ is a parameter that depends on temperature and which Held and Soden chose to be 7%/K (L is the latent heat of vaporization and R is the gas constant). Substituting this estimate for $\delta\mathbf{F}$ into the steady-state atmospheric moisture balance equation, we find:

$$\delta(P-E) \approx -\nabla \cdot (\alpha\delta T_S\mathbf{F}) \approx -\alpha\delta T_S\nabla \cdot \mathbf{F} = \alpha\delta T_S(P-E). \tag{5.10}$$

The final step in deriving the simple scaling is made by taking $\alpha\delta T_S$ outside the divergence operator in (5.10) above, implicitly assuming that the zonal and meridional structure of $P-E$ dominates that of $\alpha\delta T_S$. We shall now show that this final approximation is a poor one over land, as is the neglect of relative humidity changes, and that changes in horizontal near-surface temperature and relative humidity gradients must be accounted for in order to estimate changes in land $P-E$.

---

[4] Held and Soden considered fractional changes in vapor pressure for the derivation of their scaling. However, given that specific humidity rather than vapor pressure is archived by the CMIP5 models, and that fractional changes in vapor pressure and specific humidity are equal to a good approximation (e.g., Tsonis, 2002), we shall consider specific humidity rather than vapor pressure for the rest of this chapter.

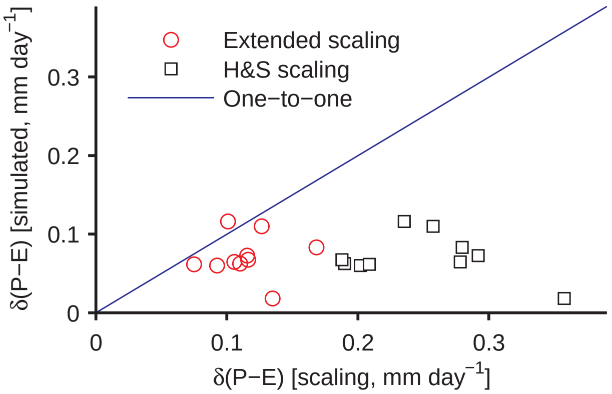

Figure 5-7: Simulated changes in global-mean land $P-E$ (i.e., mean runoff changes) versus the estimates from the Held and Soden scaling (black squares) and from the extended scaling (red circles). The blue line is the one-to-one line. The correlation coefficient for the simulated changes and the Held and Soden scaling is -0.31, and is 0.02 for the simulated changes and the extended scaling.

Under global warming, as discussed in Chapter 4, relative humidity is projected to decrease over land (O'Gorman and Muller, 2010; Laîné et al., 2014) but increase over ocean (Boer, 1993; Held and Soden, 2000). Furthermore, a pronounced spatial structure of surface temperature change is expected due to both polar amplification (Holland and Bitz, 2003) and the land-ocean warming contrast (Chapters 2 and 3).

To assess the influence of these robust features of global warming on $P-E$ changes over land, we relax the assumptions of (i) negligible changes in horizontal temperature gradients and (ii) fixed relative humidity that form part of the Held and Soden scaling. However, we continue to assume a fixed circulation, that the column-integrated moisture flux scales with the near-surface specific humidity, and that $\alpha = 7\,\%/\mathrm{K}$ is a constant. Boos (2012) derived a similar scaling which includes changes in temperature gradients but not in relative humidity. In essence, this revised set of assumptions amounts to assuming that the atmospheric *moisture flux* scales with surface-air specific humidity whereas in contrast, the Held and Soden scaling assumes that the *moisture flux divergence* scales with the surface-air specific humidity at constant relative humidity. With changes in relative humidity now retained, fractional changes in the horizontal moisture flux are now approximated as $\delta\mathbf{F}/\mathbf{F} \approx \delta q_S^*/q_S^* + \delta\mathcal{H}_S/\mathcal{H}_S$, where q_S^* is the surface-air saturation specific humidity and $\mathcal{H}_S$ is the surface-air relative humidity (we have approximated the relative humidity to be the ratio of the specific humidity to the saturation specific humidity). Following Held and Soden (2006), we write $\delta q_S^*/q_S^* = \alpha\delta T_S$ and substitute our expression for $\delta\mathbf{F}$ into $\delta(P-E) = -\nabla\cdot\delta\mathbf{F}$ to obtain the extended scaling:

$$\begin{aligned}\delta(P-E) &\approx -\nabla\cdot[(\alpha\delta T_S)\mathbf{F} + (\delta\mathcal{H}_S/\mathcal{H}_S)\mathbf{F}] \\ &= \underbrace{\alpha\delta T_S(P-E)}_{\text{Held and Soden scaling}} + \\ &\underbrace{(\delta\mathcal{H}_S/\mathcal{H}_S)(P-E) - \alpha\mathbf{F}\cdot\nabla\delta T_S - \mathbf{F}\cdot\nabla(\delta\mathcal{H}_S/\mathcal{H}_S)}_{\text{additional terms}}.\end{aligned} \tag{5.11}$$

Retaining changes in relative humidity and in horizontal gradients adds three additional terms compared to the Held and Soden scaling: A term related to local relative humidity changes $[(\delta\mathcal{H}_S/\mathcal{H}_S)(P-E)]$, and terms due to changing horizontal gradients in temperature and relative humidity $[-\alpha\mathbf{F}\cdot\nabla\delta T_S$ and $-\mathbf{F}\cdot\nabla\delta(\mathcal{H}_S/\mathcal{H}_S)$, respectively]. Although often neglected in studies of $P-E$ projections under global warming, the temperature gradient term has been found to be important in simulated $P-E$ changes between the present-day and the Last Glacial Maximum, particularly in the extratropics in the vicinity of ice sheets (Boos, 2012). We shall now apply this extended scaling to the CMIP5 global warming simulations.

5.4.2 Application of extended scaling

Using monthly-mean quantities (and a moisture flux $\mathbf{F}$ calculated from daily-mean winds and specific humidity), the extended scaling (5.11) is tested versus the simulated changes in $P-E$. Over ocean in the zonal-mean, the additional terms make little difference (Figs. 5-6a), and the estimates of the extended scaling are indistinguishable from those of the Held and Soden scaling at most latitudes. Over land, however, the extended scaling substantially improves the agreement with simulations (Fig. 5-6b): The magnitude of the moistening at many latitudes is captured, including over the Northern Hemisphere midlatitudes, as is the drying of the Southern Hemisphere subtropics. The Held and Soden scaling tends to over-moisten the land under warming, but accounting for changes in relative humidity and in horizontal temperature and relative humidity gradients brings the estimates much closer to the simulated changes. The extended scaling does not predict as much moistening of the tropics as the Held and Soden scaling, though it still overestimates the $P - E$ response substantially in this region, primarily because of mean circulation changes (see Figs. 5-5b and 5-5d) which are not accounted for in the extended scaling. Global-mean changes in land $P - E$ (equivalent to changes in runoff) are also better estimated by the extended scaling (Fig. 5-7). Relative to the Held and Soden scaling, the estimates of the mean runoff changes are much closer to the simulations. We note that the additional terms in the extended scaling dry the land relative to the simpler scaling (though neither scaling captures the intermodel scatter).

The skill of the extended scaling in capturing regional features of the simulated $P - E$ response is assessed using latitude-longitude plots (Figs. 5-8 and 5-9). As expected, due to limited evaporation over land which constrains climatological $P - E \gtrsim 0$ in the time-mean, the Held and Soden scaling predicts that all land becomes wetter under warming (Fig. 5-8b). The simulations, however, show regions of both moistening and drying (Fig. 5-8a) and the land response is not captured by the Held and Soden scaling even qualitatively. The extended scaling is more successful (Fig. 5-8c), accounting for interesting features of the simulated response including drying over parts of North America and the southern part of South America, and the broad and weak drying of southern Europe and Central Asia. Not all features of the simulations are captured, and the extended scaling overestimates the drying and moistening signals in various regions (e.g., North Africa). Nevertheless the extended scaling represents an important step towards understanding and improving projections of regional water cycle changes over land. Over ocean, the predictions from the Held and Soden and extended scalings are more similar (Figs. 5-9b and 5-9c), though the extended scaling may be useful for understanding water cycle changes in the North Atlantic, where large spatial gradients in the surface temperature response to global warming are projected (e.g., Drijfhout et al., 2012).

We now assess the contributions of the individual terms in the extended scaling,

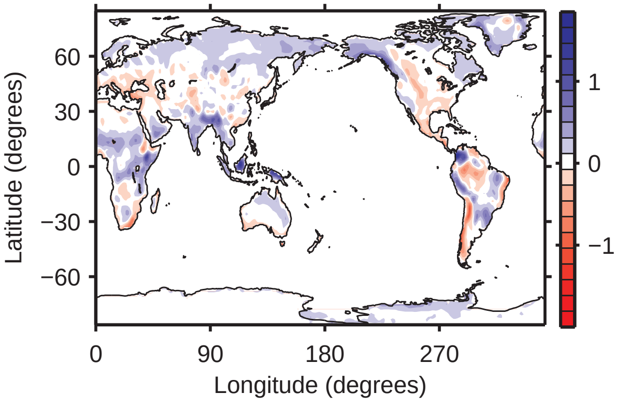

Latitude (degrees)
60
30
0
−30
−60
0
90
180
270
Longitude (degrees)
1
0
−1

(a) Simulated

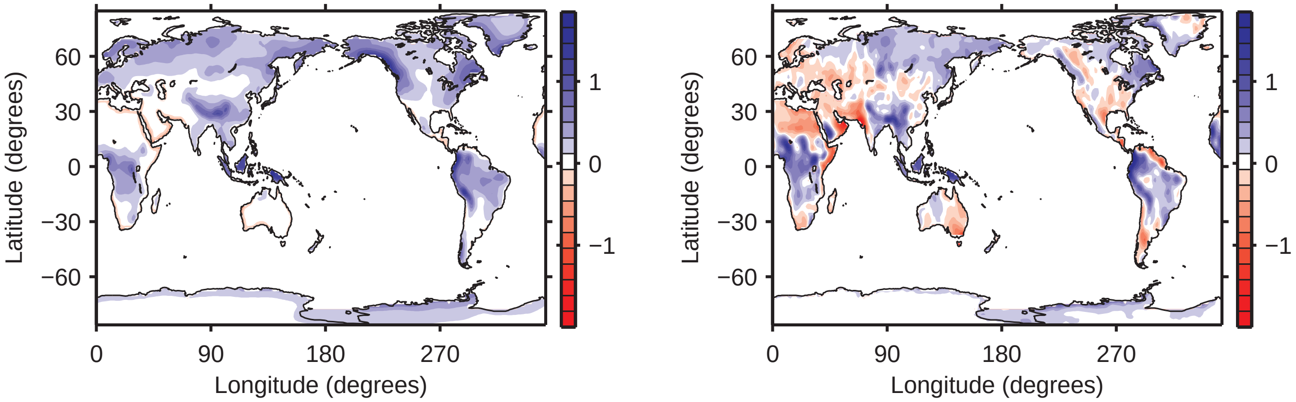

Latitude (degrees)
60
30
0
−30
−60
0
90
180
270
Longitude (degrees)
1
0
−1
Latitude (degrees)
60
30
0
−30
−60
0
90
180
270
Longitude (degrees)
1
0
−1

(b) Held and Soden scaling

(c) Extended scaling

Figure 5-8: (a) Multimodel-mean simulated changes in $P - E$ between the historical and RCP8.5 simulations and the changes estimated using (b) the Held and Soden scaling and (c) the extended scaling. Only the changes over land are shown. The units are millimeters per day, and each plot has been smoothed using a low-pass 1-2-1 filter.

and describe the physical mechanism by which changes in temperature and relative humidity gradients under global warming lead to drying tendencies over land.

5.4.3 Physical interpretation

The four components of the extended scaling, zonally-averaged over land, are shown in Figure 5-10. The first term [$\alpha\delta T_S(P - E)$, Fig. 5-10a] is the Held and Soden scaling and has a familiar structure, namely moistening at almost all latitudes. The second term in the extended scaling, [$(\delta\mathcal{H}_S/\mathcal{H}_S)(P-E)$, Fig. 5-10b], arises from local changes in relative humidity and is entirely negligible at all latitudes. Land relative

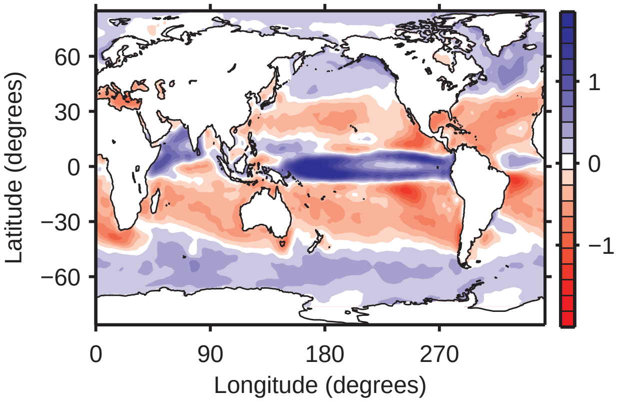

Latitude (degrees)
60
30
0
−30
−60
0
90
180
270
Longitude (degrees)
1
0
−1

(a) Simulated

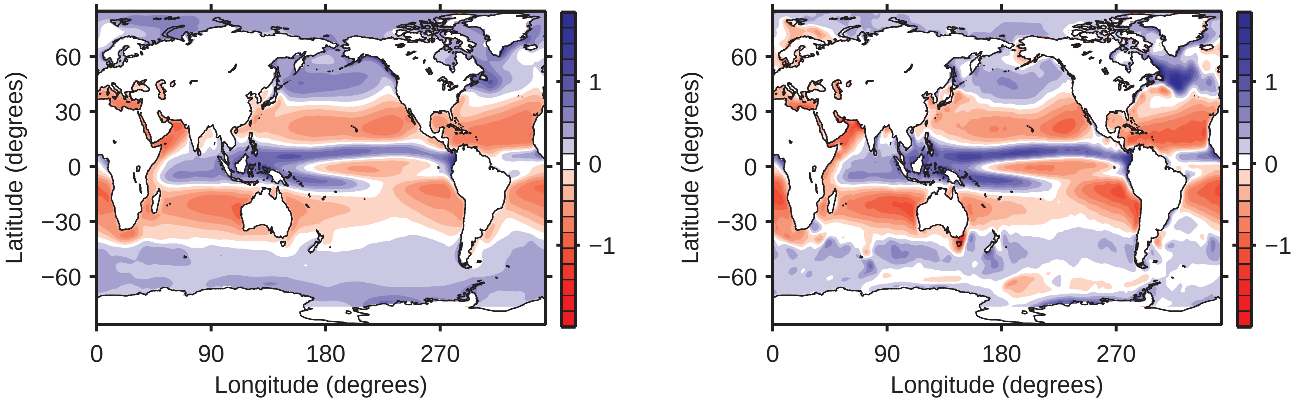

Latitude (degrees)
60
30
0
−30
−60
0
90
180
270
Longitude (degrees)
1
0
−1
Latitude (degrees)
60
30
0
−30
−60
0
90
180
270
Longitude (degrees)
1
0
−1

(b) Held and Soden scaling

(c) Extended scaling

Figure 5-9: As in Figure 5-8, but here showing only the changes over ocean regions.

humidity is expected to decrease substantially as the climate warms (Fig. 4-1b), particularly in the subtropics. However, due to (i) climatological $P - E$ over land tending to be close to zero in these arid subtropical regions (Fig. 5-1b) and (ii) an anti-correlation over the seasonal cycle between land relative humidity changes and climatological $P-E$, the impact of these local relative humidity decreases on changes in $P - E$ is small. The final terms are dot products of the basic-state moisture flux with changes in horizontal specific humidity gradients due to temperature changes [$-\alpha\mathbf{F} \cdot \nabla\delta T_S$, Fig. 5-10c] and due to relative humidity changes [$-\mathbf{F} \cdot \nabla(\delta\mathcal{H}_S/\mathcal{H}_S)$, Fig. 5-10d], respectively. Unlike over ocean, where the gradient terms are generally negligible except for a narrow region in the midlatitudes (Fig. 5-11), both gradient terms have substantial magnitudes over land, and it is clear that changes in humidity gradients should be taken into account when considering changes in the terrestrial

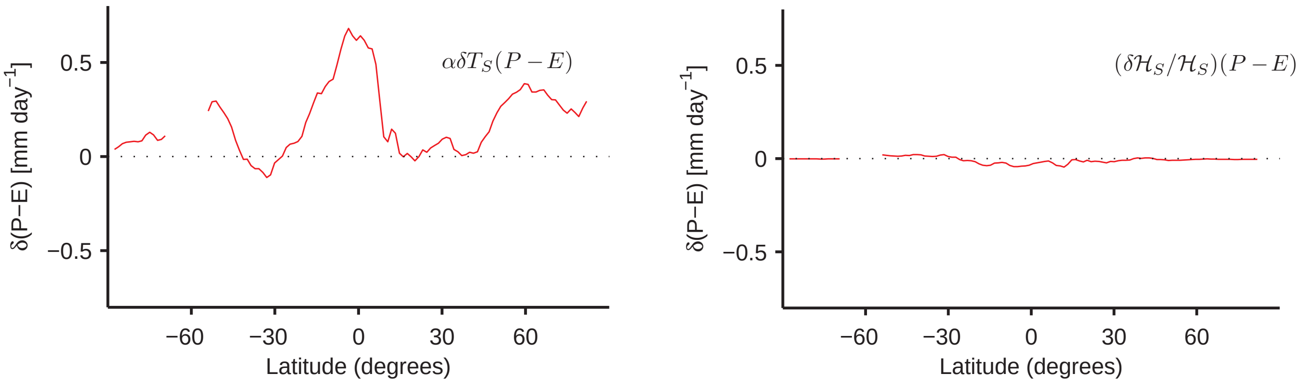

(a) Local temperature term

(b) Local relative humidity term

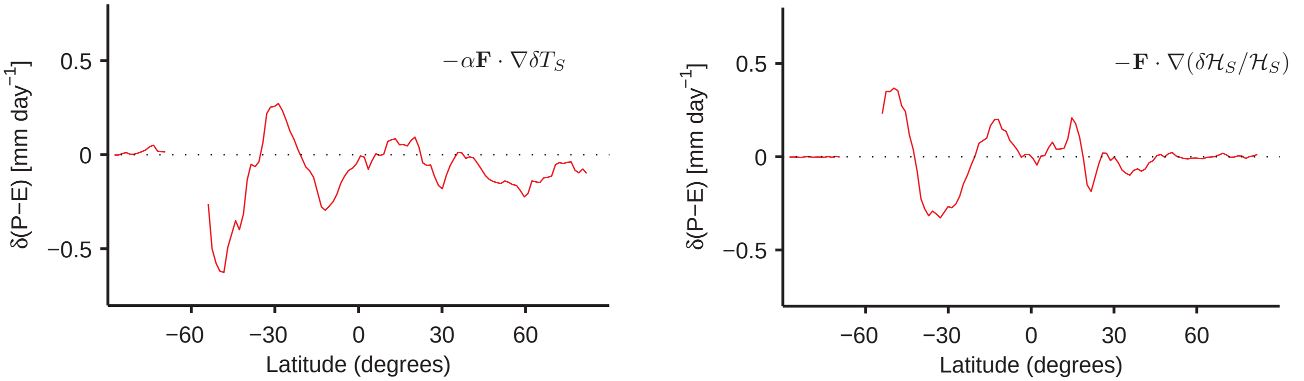

(c) Temperature gradient term

(d) Relative humidity gradient term

Figure 5-10: The various terms in the extended scaling for $P - E$ over land, defined by (5.11). In each case the multimodel mean is plotted.

water cycle. The temperature and relative humidity gradients terms tend to cancel one another to some extent, particularly in the Southern Hemisphere, which is not surprising as temperature and relative humidity changes over land are strongly anti-correlated due to dynamical constraints (as discussed in Chapters 2 and 3).

The relative importance of changes in zonal versus meridional gradients can be seen in Figure 5-12. For both the temperature gradient (Fig. 5-12a) and relative humidity gradient (Fig. 5-12b) terms, the zonal component dominates the response (though the meridional component is not entirely negligible). For the temperature component, the zonal gradients produce drying almost uniformly, but the relative humidity component has latitudes of both drying and moistening. Despite large gradients in meridional temperature changes associated with polar amplification, Figure

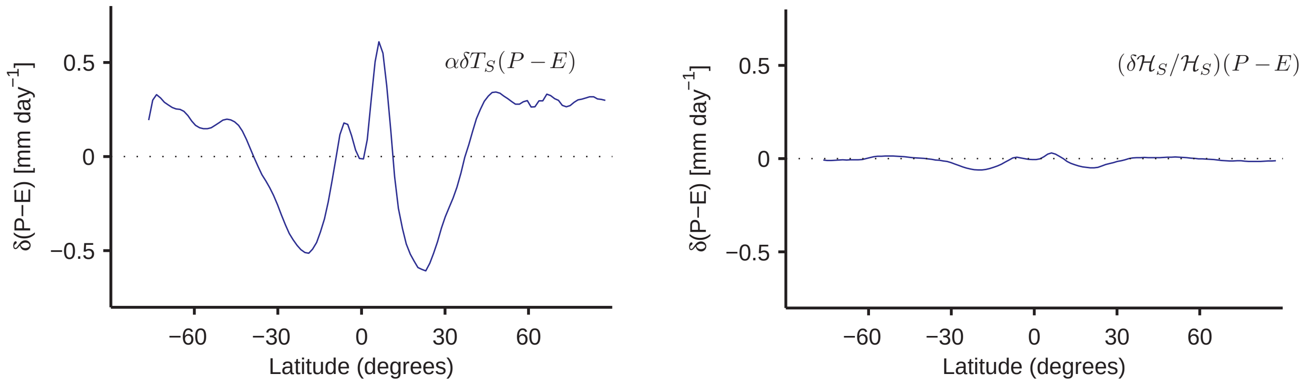

(a) Local temperature term

(b) Local relative humidity term

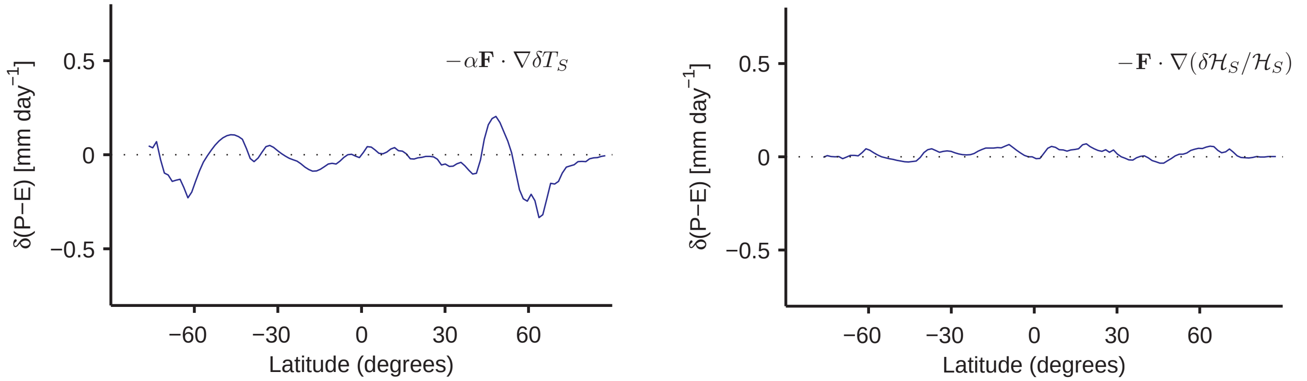

(c) Temperature gradient term

(d) Relative humidity gradient term

Figure 5-11: As in Figure 5-10, but for ocean regions.

5-12 suggests that it is changes in zonal humidity gradients (e.g., due to the land-ocean warming contrast) that are important for water cycle changes over land.

To understand how these flux-gradient terms lead to changes in $P-E$, we consider two distinct mechanisms that result in drying in the zonal mean (we focus here on the zonal temperature gradient term, though the mechanisms for meridional and relative humidity gradients are analogous):

1. For the first mechanism, depicted schematically in Figure 5-13a, we imagine a climatological westerly moisture flux (e.g., in midlatitudes), convergent over the land continent ($\nabla\cdot\mathbf{F} < 0$). We further imagine a surface-air temperature change profile in longitude which exhibits enhanced warming over land relative to ocean, as expected under global warming, and which has east-west symmetry across the land continent (i.e., maximum warming in the middle of the continent, decaying

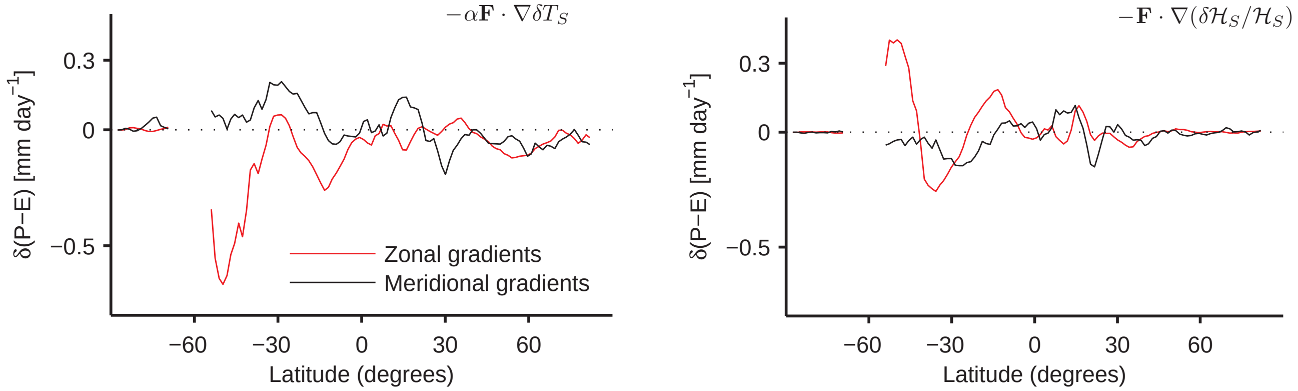

(a) Zonal and meridional components of temperature gradient term

(b) Zonal and meridional components of relative humidity gradient term

Figure 5-12: The multimodel-mean zonal (red) and meridional (black) components of the (a) temperature and (b) relative humidity gradient terms in the extended scaling (5.11).

towards the east and west coastlines). The precise shape of the warming profile is not important for this mechanism, rather it simply requires the gradient of the temperature changes to integrate to zero across the continent (i.e., δT_S must have the same value at the east and west coastlines). In the schematic, the gradient vector of the temperature changes points to the east over the western portion of the continent (in the same direction as the moisture flux), giving a drying according to (5.11), and points to the west on the eastern side, giving a moistening there. We are considering a convergent basic-state moisture flux, and so the magnitude of that flux is larger over the western side of the continent than over the eastern side, therefore the drying tendency is of a larger magnitude than the moistening tendency. Thus, zonally-averaged over the continent, a convergent moisture flux and enhanced warming over land versus ocean that is symmetric across the continent (or simply warming that has the same magnitude on both coastlines) will give a net continental drying. We refer to this as the "symmetric warming" mechanism.

2. For the second drying mechanism, we consider a non-divergent climatological moisture flux and an *asymmetric* warming profile over the continent, with enhanced warming on the leeward side compared to the windward side (Fig. 5-

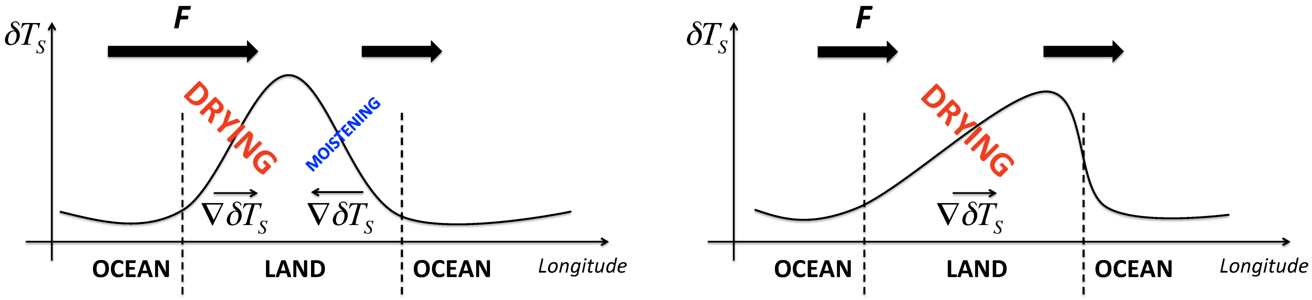
δT_S
F
DRYING
MOISTENING
$\overrightarrow{\nabla \delta T_S}$
$\overleftarrow{\nabla \delta T_S}$
OCEAN
LAND
OCEAN
Longitude
δT_S
F
DRYING
$\overrightarrow{\nabla \delta T_S}$
OCEAN
LAND
OCEAN
Longitude

(a) Symmetric land warming

(b) Asymmetric land warming

Figure 5-13: Schematic diagrams of the two mechanisms by which changes in horizontal temperature gradients can dry the land. The heavy black arrows represent a climatological zonal atmospheric moisture flux and the curves are idealized profiles of surface-air temperature changes versus longitude.

13b). In this scenario, the gradient vector of the temperature changes is in the same direction as the flux over most of the continent, producing a net drying of the land. This mechanism does not require a convergent moisture over land in the basic state, but rather requires that the temperature change over land is larger on the leeward coastline. This is the “asymmetric warming” mechanism.

We now attempt to quantify the relative roles of a symmetric land-ocean warming contrast (mechanism 1) versus asymmetric continental warming (mechanism 2) in the simulated response of land $P - E$ (Fig. 5-14). We decompose the simulated $-\alpha \mathbf{F} \cdot \nabla \delta T_S$ term into a sum of contributions due to each mechanism:

$$-\alpha \left\{ F_x \frac{\partial \delta T_S}{\partial x} \right\} = \underbrace{-\alpha \{F_x\} \left\{ \frac{\partial \delta T_S}{\partial x} \right\}}_{\text{asymmetric}} \underbrace{-\alpha \left\{ F_x^* \left[\frac{\partial \delta T_S}{\partial x} \right]^* \right\}}_{\text{symmetric}}, \tag{5.12}$$

where $\{\cdot\}$ denotes the zonal mean across a continent, $(\cdot)^*$ denotes the departure from the zonal mean across the continent, and x is the zonal direction (we have used Cartesian coordinates here for simplicity). If the warming at both coastlines is equal, the asymmetric term is zero; if the moisture flux is homogeneous across the continent, the symmetric term is zero.

Interestingly, we find that the asymmetric warming effect dominates in the extratropics, but it is close to zero in the tropics/subtropics where the symmetric warming

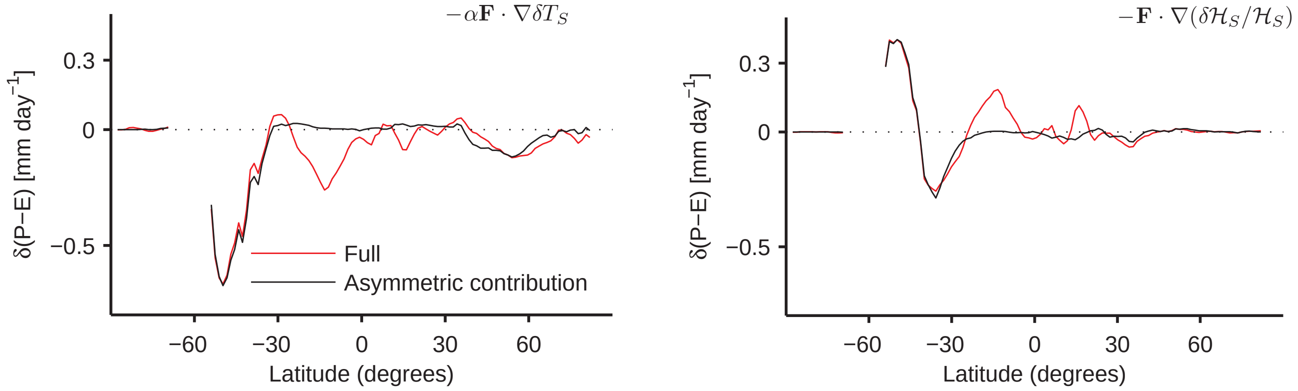

(a) Temperature gradient term

(b) Relative humidity gradient term

Figure 5-14: The contributions to the zonal (a) temperature and (b) relative humidity gradient terms due to east-west asymmetries in surface-air temperature and relative humidity changes, respectively (black), as calculated from (5.12). Red lines show the full zonal temperature and relative humidity gradient terms.

effect is more important (Fig. 5-14a). Similar behavior is found for the relative humidity gradient term, with asymmetric relative humidity changes over continents dominating the response in the Southern Hemisphere midlatitudes but not at lower latitudes (Fig. 5-14b). The reasons for this contrasting behavior between low and high latitudes are not entirely clear, though it is likely due to stronger mean zonal winds (larger non-divergent moisture flux compared to the divergent flux) and more east-west asymmetry in δT_S at midlatitudes, with both effects emphasizing mechanism 2 in those regions.

5.4.4 Specific humidity formulation

We have formulated the extended scaling (5.11) in terms of changes in surface-air temperature and relative humidity. However, as expected from our analyses in Chapters 2, 3 and 4, there is cancellation between the temperature and relative humidity gradient contributions to the extended scaling (cf. Figs. 5-10c and 5-10d) due to the anti-correlation of these changes over land. To account for this cancellation and assess the net contribution of changes in horizontal specific humidity gradients to $\delta(P-E)$, we derive an alternative form of the extended scaling for $P-E$ in terms

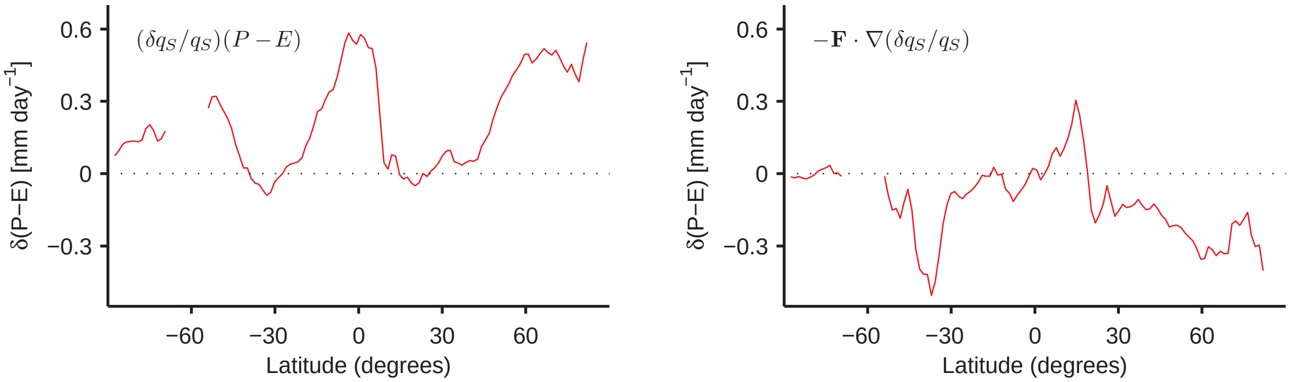

(a) Local specific humidity changes

(b) Specific humidity gradient changes

Figure 5-15: The contributions to the specific humidity formulation of the extended scaling for $P-E$ over land, defined by (5.13). In each case the multimodel mean is plotted.

of the surface-air specific humidity changes:

$$\begin{aligned}\delta(P-E) &\approx -\nabla\cdot[(\delta q_S/q_S)\mathbf{F}] \\ &= (\delta q_S/q_S)(P-E) - \mathbf{F}\cdot\nabla(\delta q_S/q_S).\end{aligned} \tag{5.13}$$

The contribution to $\delta(P-E)$ from local specific humidity changes, $(\delta q_S/q_S)(P-E)$, is very similar to the Held and Soden scaling though here includes a small correction due to local relative humidity changes over land (Fig. 5-15a). The specific humidity gradient term, $-\mathbf{F}\cdot\nabla(\delta q_S/q_S)$, includes changes in both temperature and relative humidity gradients and is a drying term at most latitudes (Fig. 5-15b).

The conceptual model for changes in land humidity derived in Chapter 4, which compares spatially-averaged changes in land and ocean humidities, suggests equal fractional changes in boundary-layer specific humidity over land and ocean but is not directly applicable to gradients over land continents. However, if we apply it to individual grid boxes over land, then it would say that fractional changes in specific humidity do not vary spatially over land, implying no net contribution from the gradient term in (5.13) to $P-E$ changes. However, as is clear from Figure 5-15b, changes in surface-air specific humidity gradients contribute substantially to $P-E$ changes at many latitudes, confirming that fractional changes in specific humidity do

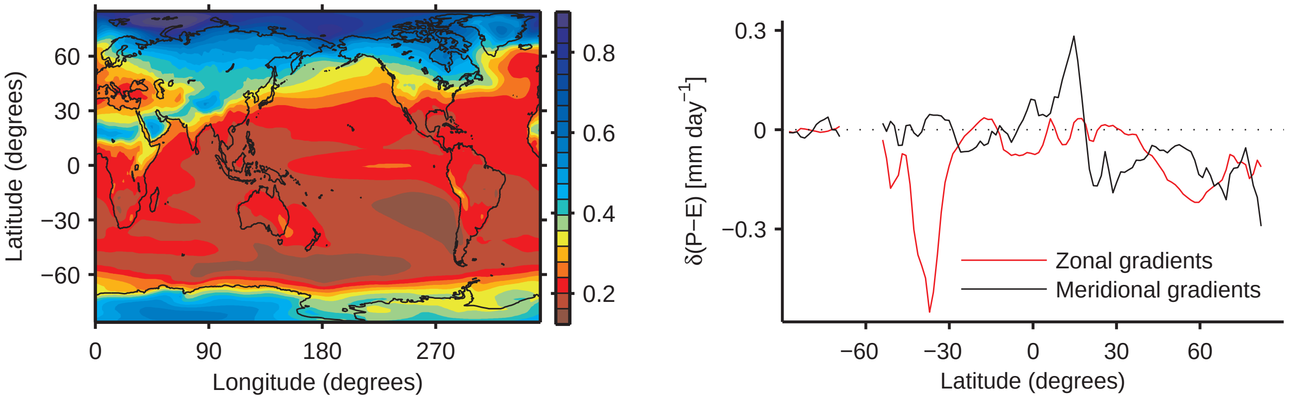

(a) $\delta q_S/q_S$: Gridpoint values

(b) $-\mathbf{F}\cdot\nabla(\delta q_S/q_S)$: Zonal and meridional components

Figure 5-16: (a) Multimodel-mean fractional changes in surface-air specific humidity, $\delta q_S/q_S$, between the historical (1976-2005) and RCP8.5 (2070-2099) simulations, and (b) the multimodel-mean zonal (red) and meridional (black) components of the specific humidity gradient term in the scaling (5.13).

vary spatially over continents. Thus, the conceptual model for land relative humidity changes cannot be applied to individual locations over land, rather it is valid only when averaged in longitude or over a large region.

The drying over land due to fractional changes in specific humidity gradients results from the symmetric and asymmetric mechanisms described in Section 5.4.3, where these mechanisms are now interpreted in terms of changes in specific humidity gradients rather than changes in temperature gradients. For example, larger fractional increases in specific humidity over the eastern sides of the continents in the Northern Hemisphere midlatitudes (Figs. 5-16a and 5-16b) leads to drying via the asymmetric mechanism (changes in meridional gradients are also important in this region). The broad drying in the Southern Hemisphere also results from changes in zonal specific humidity gradients (Fig. 5-16b). In contrast, the moistening in the Northern Hemisphere tropics (Figs. 5-15b and 5-16b) is largely due to a meridional gradient in $\delta q_S/q_S$ over Africa (Figs. 5-16a and 5-16b) which is directed poleward, opposing the equatorward moisture flux by the Hadley cell and moistening that region. The reason for the asymmetric response of $\delta q_S/q_S$ across continents is not clear and requires further investigation (potentially including an extended analysis of the conceptual model for humidity changes in Chapter 4).

5.5 Modifications to the extended scaling

We have derived and tested an extended version of the Held and Soden scaling for $P - E$ in order to better understand simulated changes in the water cycle over land. We now briefly describe two modifications to this scaling which help to improve our understanding of the processes contributing to terrestrial water cycle changes, but do not alter the extended scaling's estimates qualitatively.

5.5.1 Column water vapor analysis

In our analysis of the hydrological cycle we have assumed that the vertically-integrated atmospheric moisture flux scales with the surface-air humidity. We might expect this to be a reasonable assumption for mean overturning circulations, such as the Hadley and Walker cells, for which the moisture transport is dominated by the near-surface branch of the circulation (Peixóto and Oort, 1984). Transient eddies, in contrast, transport moisture near the surface but also transport substantial amounts up to 500hPa. Given the strong vertical structure of temperature changes under global warming, with δT generally increasing with height following a moist adiabat (e.g., Santer et al., 2005), along with changes in relative humidity that are non-uniform with height (Sherwood et al., 2010) and the temperature dependence of the Clausius-Clapeyron parameter, α, which we have set to 7%/K throughout this chapter, we would not necessarily expect the transient eddy moisture flux to accurately scale with the near-surface specific humidity, even in the absence of dynamical changes in the eddy field.

To investigate the validity of scaling the moisture flux with the surface-air humidity, we repeat our scaling analysis but now assuming that the moisture flux scales with column-integrated water vapor, CWV, i.e. $\delta\mathbf{F}/\mathbf{F} \approx \delta CWV/CWV$. Following Boos (2012), we express fractional changes in CWV with changing surface-air temperature as:

$$\delta CWV/CWV \equiv \alpha^{*} \delta T_S, \tag{5.14}$$

where α^{*} is a parameter mapping changes in column water vapor to changes in surface-air temperature (with the vertical structure of temperature and relative humidity changes determining the magnitude of α^*). We calculate α^* using the simulated CWV, δCWV, and δT_S. Writing $\delta \mathbf{F} = \alpha^* \delta T_S \mathbf{F}$ and substituting this expression into $\delta(P - E) = -\nabla \cdot \delta \mathbf{F}$ as before, we obtain the following scaling for $\delta(P - E)$:

$$\delta(P - E) \approx \alpha^* \delta T_S (P - E) - \mathbf{F} \cdot \nabla(\alpha^* \delta T_S). \tag{5.15}$$

Note that unlike the Boos (2012) scaling, in (5.15) we retain the horizontal dependence of α^*.

We now use (5.15) to estimate the mean thermodynamic and transient eddy components of $\delta(P - E)$ over land and compare this CWV scaling to our original scaling based on surface-air humidity changes (Fig. 5-17). For both components over land and ocean, the new scaling (5.15) based on CWV is very similar to that based on surface-air specific humidity (5.11). For the mean thermodynamic component, the CWV scaling is marginally less accurate than the q_S scaling (Figs. 5-17a and 5-17c), reflecting the observation that the majority of moisture transport by mean circulations takes place close to the surface. Perhaps unexpectedly, the agreement of the CWV scaling with simulated changes in the transient eddy component is no better than the q_S scaling (Figs. 5-17b and 5-17d), despite substantial eddy moisture transport above the boundary layer. In the absence of relative humidity changes, we would expect scaling by q_s to underestimate fractional changes in vertical-mean eddy transport, because of the larger δT and larger α aloft. The similarity of the two scalings may be a result of competing changes in temperature and relative humidity in the troposphere; although δT typically increases with height, global warming simulations show reductions in relative humidity over large parts of the troposphere (Sherwood et al., 2010) and so the fractional changes in specific humidity may be relatively constant with height under warming.

That the scalings based on CWV and on q_S give similar results is encouraging, as it suggests that changes in the vertical humidity structure under warming are not particularly important for $P - E$, and that a good approximation to changes in the

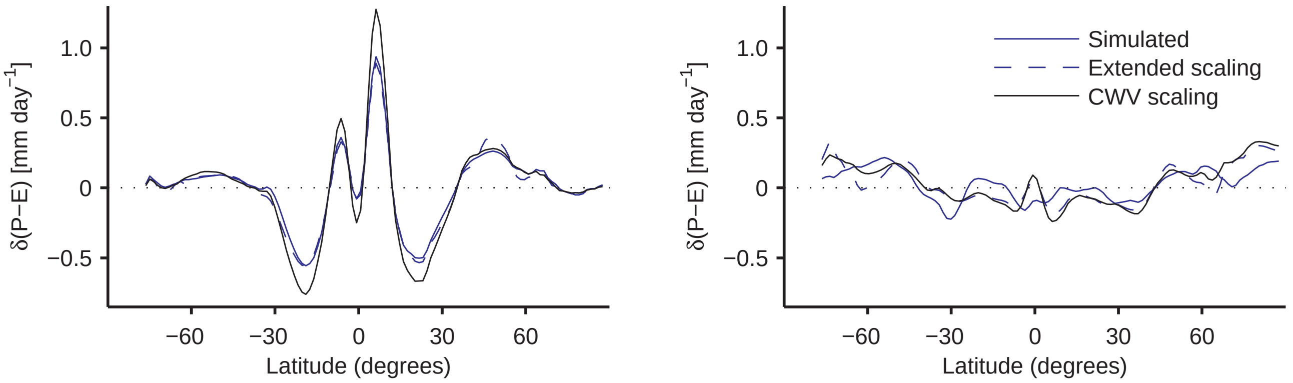

(a) Ocean, mean thermodynamic component

(b) Ocean, transient eddy component

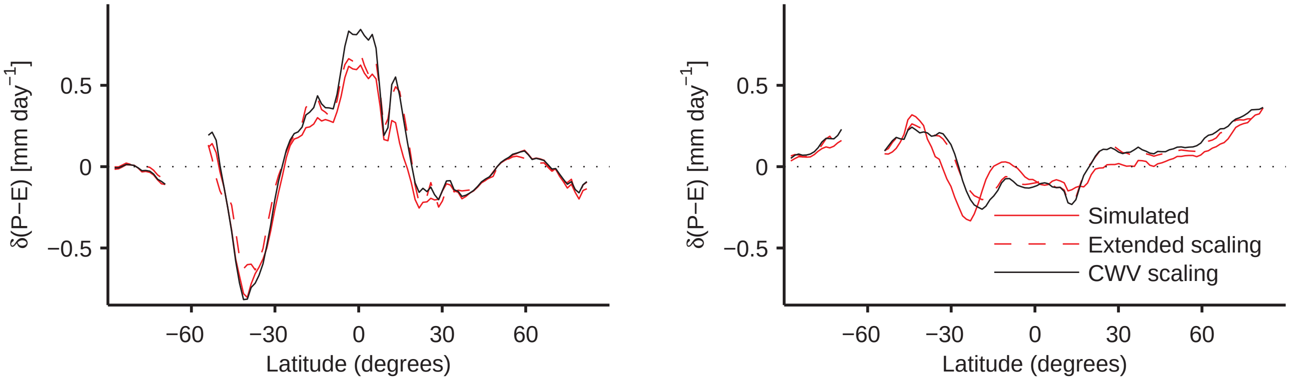

(c) Land, mean thermodynamic component

(d) Land, transient eddy component

Figure 5-17: Comparison of the multimodel-mean simulated (blue and red solid lines) changes in the [(a) and (c)] mean thermodynamic and [(b) and (d)] transient eddy components of $P - E$ with the extended scaling estimates (blue and red dashed lines) and with estimates from the column water vapor scaling (black solid lines), over [(a) and (c)] ocean and [(b) and (d)] land. The extended and column water vapor scalings are defined by (5.11) and (5.15), respectively.

water cycle over land and ocean can be obtained by solely understanding changes in near-surface humidity.

5.5.2 Diffusive moisture transport by transient eddies

In deriving the extended scaling for $P - E$ changes over land, we assumed that the horizontal moisture flux by both the mean circulation and by the transient eddies scales directly with the surface-air specific humidity. However, the moisture flux by transient eddies is often modeled conceptually and in energy balance models as a simple diffusive process (e.g., O'Gorman and Schneider, 2006). If we assume that the eddies transport moisture diffusively down the mean surface-air humidity gradient, we can write the transient eddy contribution to $P - E$ as follows:

$$(P - E)_{eddy} = -\nabla \cdot \mathbf{F}_{eddy} \equiv \nabla \cdot \mathcal{D} \nabla q_S, \tag{5.16}$$

where $\mathcal{D}$ is the diffusivity and $\mathbf{F}_{eddy}$ is the component of the moisture flux due to transient eddies alone. Writing $\delta q_S / q_S = \alpha \delta T_S + \delta \mathcal{H}_S / \mathcal{H}_S$ as before, changes in $(P - E)_{eddy}$ can be expressed as:

$$\delta(P - E)_{eddy} \approx \nabla \cdot \mathcal{D} \nabla [q_S(\alpha \delta T_S + \delta \mathcal{H}_S / \mathcal{H}_S)], \tag{5.17}$$

where changes in the eddy diffusivity under warming have been neglected. If we further neglect the spatial structure of diffusivity, assume that $\alpha = 7\%/\mathrm{K}$ everywhere [as assumed in the Held and Soden (2006) and extended scalings], and drop terms containing the Laplacian of temperature or relative humidity changes [i.e. terms with $\nabla^2 \delta T_S$ or $\nabla^2(\delta \mathcal{H}_S / \mathcal{H}_S)$], then (5.17) becomes:

$$\begin{aligned} \delta(P - E)_{eddy} &\approx \alpha \delta T_S (P - E)_{eddy} + \\ &(\delta \mathcal{H}_S / \mathcal{H}_S)(P - E)_{eddy} - 2\alpha \mathbf{F}_{eddy} \cdot \nabla \delta T_S - 2\mathbf{F}_{eddy} \cdot \nabla(\delta \mathcal{H}_S / \mathcal{H}_S). \end{aligned} \tag{5.18}$$

This diffusive scaling for the contribution of transient eddies to $P - E$ changes is similar to the eddy part of the extended Held and Soden scaling (5.11), but it has twice the contribution from the temperature and relative humidity gradient terms because we are now assuming that the eddy flux acts diffusively.

Applying the diffusive scaling to the simulated $\delta(P - E)$ over land and ocean (Fig. 5-18), we find that the agreement with the simulations is very similar to that of the extended scaling (5.11) at most latitudes. In the Northern Hemisphere mid- and high-latitudes, however, the scalings diverge somewhat, and the agreement of the diffusive scaling with simulations deteriorates over ocean (Fig. 5-18a) but improves over land

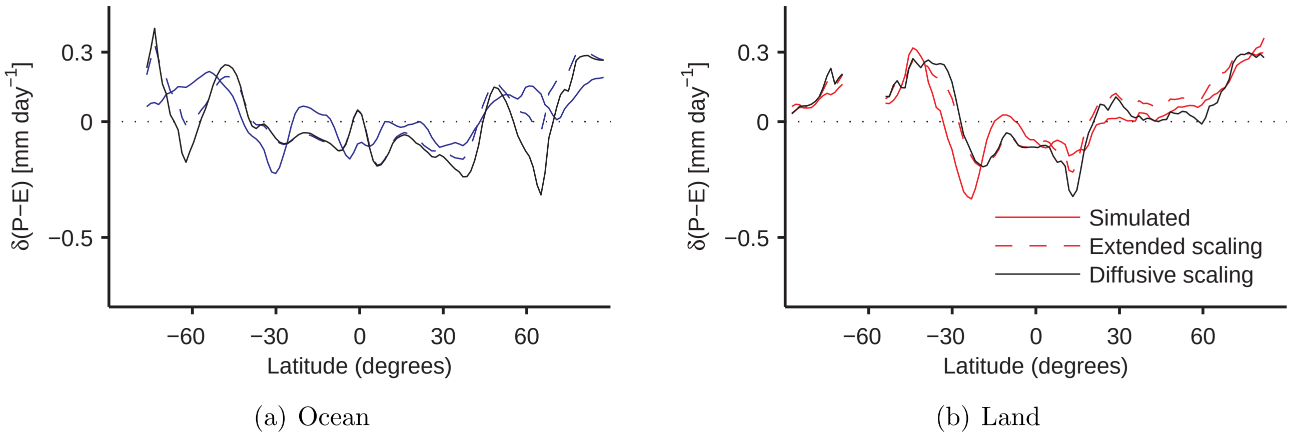

(a) Ocean

(b) Land

Figure 5-18: Multimodel-mean simulated (blue and red solid lines) transient eddy component of $P - E$ changes along with the extended scaling estimates (dashed lines) and the estimates from the diffusive scaling (black solid lines), over (a) ocean and (b) land. The extended and diffusive scalings are defined by (5.11) and (5.18), respectively.

(Fig. 5-18b). This suggests that changes in diffusivity under warming, or spatial variations in the diffusivity (both of which are neglected in the derivation above), are more important over ocean than over land, or that scaling the diffusive flux with the gradient in q_S is more appropriate over land. However, further work is needed to fully understand the differences between the extended and diffusive scalings.

5.6 Conclusions

We have investigated water cycle changes in CMIP5 simulations and found, as for observed water cycle changes over recent decades, that the magnitude and latitudinal structure of future changes in $P - E$ are expected to be very different over land and ocean. The ocean response to global warming can be understood, at least qualitatively, as an enhancement of climatological $P - E$. This behavior results from increased atmospheric moisture transport in a warmer climate following the Clausius-Clapeyron relation. In agreement with previous studies, we have demonstrated that this “rich-get-richer” response (known here as the Held and Soden scaling) does not apply over land, where it substantially overestimates the simulated moistening under global warming and does not capture regions of drying. Various mechanisms, such as mean circulation changes and changes in horizontal temperature and relative humidity gradients, have been shown to be important for the $P - E$ response over various land regions. However, a clear understanding of the robust and systematic discrepancy between the simple scaling and the simulations has been elusive.

Modifying the Held and Soden scaling, and assuming that the atmospheric moisture flux rather than the moisture flux divergence scales with low-level humidity under warming (and, in addition, relaxing the assumption of fixed relative humidity), we have derived an extended scaling for $P-E$. The extended scaling includes additional terms due to local changes in relative humidity (this effect turns out to be negligible everywhere) and changes in horizontal surface-air temperature and relative humidity gradients. A similar scaling was used by Boos (2012) to investigate changes in the hydrological cycle between present day and the LGM, but here we include changes in relative humidity gradients, use surface-air quantities, and focus on changes over land under global warming. This extended scaling, which like the Held and Soden scaling assumes fixed mean and transient eddy circulations and neglects changes in the vertical distribution of water in the atmosphere, substantially improves estimates of changes in land $P - E$ globally, in the zonal-mean, and regionally. In particular, the projected drying of southern South America, North America, and Europe is captured by the extended scaling. In contrast, the extended scaling estimates of changes in ocean $P - E$ are almost identical to those of the Held and Soden scaling. The additional terms in the extended scaling, in particular the temperature and relative humidity gradient terms, have large magnitudes over land and near coastlines and give a net drying relative to the Held and Soden scaling, bringing the estimates of global-mean changes in land $P - E$ much closer to the simulated changes. This net drying is primarily due to changes in zonal temperature gradients, arising from both the land-ocean warming contrast and east-west asymmetries in continental warming. The temperature gradient term gives systematic continental drying at low latitudes because of climatological moisture fluxes that are convergent over the continents (i.e., $P - E > 0$) and surface temperature changes that are larger in the continental interior. At higher latitudes, the drying results from strong prevailing winds and larger temperature increases on the leeward sides of continents.

The extended scaling, for the first time, provides a relatively simple way to understand first-order changes in the water cycle over land under global warming. The scaling is attractive because, like the Held and Soden scaling, it does not require explicit knowledge of changes in circulation or in the vertical humidity structure under warming. Only changes in the surface-air specific humidity field are needed in order to explain much of the response of $P - E$ over land. However, not all regional-scale features of the response can be explained with the extended scaling, and although the scaling gives a reasonable estimate of the global- and multimodel-mean changes over land, the intermodel scatter is not explained. Changes in the mean circulation under warming are non-negligible over land, particularly at lower latitudes, and so a more advanced scaling to quantitatively understand $P - E$ changes must include a theory for these circulation changes. Changes in temperature gradients over and near land regions under global warming are strong, and the mean dynamic contribution to the $P - E$ changes could potentially be related to these gradient changes via thermal wind balance. Additionally, it would be interesting to use the extended scaling to investigate periods of notable terrestrial drying over the historical period and in paleoclimate records.

Chapter 6

Concluding remarks

6.1 Summary of key points

The goal of this thesis was to further our understanding of land-ocean contrasts under climate change. In this concluding chapter, we review the key results and suggest possible avenues for future research.

First, we investigated the land-ocean warming contrast whereby land surface temperatures increase more than ocean temperatures as the climate warms (Chapters 2 & 3). Building on work by Joshi et al. (2008), a convective quasi-equilibrium (CQE) theory was developed relating the surface warming contrast at low latitudes to differing changes in lapse rates over land and ocean. The theory is summarized by stating the equivalent potential temperature is the same over land and ocean: $\theta_{e,\mathrm{L}} = \theta_{e,\mathrm{O}}$. Inverting this nonlinear equation numerically allows for quantitative estimates of changes in land temperature as a function of changes in ocean temperature and in the land and ocean relative humidities. Applied to idealized GCM simulations over a wide range of climates, the theory performed well, accurately estimating the magnitude of the warming contrast in the tropics and its dependence climate. A variation of the CQE theory, which assumes *equal changes* in equivalent potential temperature over land and ocean, was applied to full-complexity CMIP5 simulations. The alternative theory captured the magnitude of the multimodel-median tropical warming contrast and explained approximately 45% of the intermodel variance. The spread in simulated warming contrasts amongst the various CMIP5 models is largely due to differences in the response of land relative humidity to warming. Land relative humidity changes account for roughly half of the magnitude of the tropical warming contrast; the other half is due to changes in ocean relative humidity and land-ocean temperature and relative humidity contrasts in the basic-state climate. The significance of this work is that, for the first time, the land-ocean warming contrast can be estimated quantitatively using a theory based upon well-established principles of tropical atmospheric dynamics.

The CQE theory for the land-ocean warming contrast takes the land relative humidity changes as an input, and these changes themselves are not well understood. Both idealized and CMIP5 simulations show robust increases in global-mean ocean relative humidity as the climate warms but decreases over land. Surface energy balance arguments have been used to understand the modest increases in ocean relative humidity, but these arguments are difficult to apply to the more complex land surfaces. Unlike ocean, changes in land evapotranspiration are not strongly controlled by changes in the relative humidity of the near-surface layer but are also related to changes in soil moisture, land-use, stomatal conductance, and the surface-air temperature disequilibrium. Motivated by Rowell and Jones (2006), O'Gorman and Muller (2010) and others, who hypothesized that changes in near-surface land humidity are related to the moisture imported from the ocean, we derived a conceptual model for changes in land humidity (Chapter 4). Considering the moisture balance of the surface-air layer over land, the model represents only horizontal moisture transport with the ocean and vertical exchange with the free troposphere. The prediction of the conceptual model is that the ratio of land to ocean surface-air specific humidity remains approximately constant as the climate changes. Applying the conceptual model to idealized and CMIP5 simulations, it was found to capture the decreases in land relative humidity to first order. An extended model, explicitly including the dependence of the land humidity on evapotranspiration, was also derived. The influence of evapotranspiration changes on the land humidity was found to be small relative to the oceanic influence. The ability of the simple conceptual model to capture the simulated land relative humidity decreases is impressive given its simplicity, and this suggests that changes in land surface properties under warming do not strongly influence the multimodel-mean and zonal-mean response. However, within large continents, where the influence of moisture advection from the ocean is weak, changes in soil moisture and/or stomatal conductance could have a larger impact. Also in cold climates and at high latitudes, where changes in evapotranspiration may be large due to enhanced potential evaporation and increased soil moisture, the land humidity may be more strongly controlled by local surface conditions than by remote ocean humidity. This suggests that for regional predictions of the land relative humidity response and for the intermodel scatter, details of how the various models simulate vegetation and land surface hydrology are likely to be important.

Finally, we investigated terrestrial water cycle changes in CMIP5 simulations (Chapter 5), looking specifically at precipitation minus evaporation ($P - E$). Projected $P - E$ changes over ocean can be qualitatively described using a simple thermodynamic scaling (Held and Soden, 2006). However, the scaling does not capture the changes over land which are generally smaller than those over ocean. An extended scaling for $P - E$ was derived, analogous to that of Held and Soden but accounting for changes in relative humidity and in horizontal temperature gradients. This extended scaling was found to approximate the simulated changes in land $P - E$ in the zonal- and global-mean reasonably accurately. Interesting features of the regional $P - E$ response, such as the projected drying of the southwestern United States, were also captured to some extent. However, effects such as spatial shifts and a slowdown of the mean atmospheric circulation lead to discrepancies between the extended scaling and the simulations, particularly in the tropics. The extended scaling highlights the important role of changes in horizontal temperature and relative humidity gradients, particularly near coastlines as a result of land-ocean contrasts in temperature and relative humidity changes, in controlling changes in the terrestrial water cycle under global warming. The simplicity of the extended scaling is attractive, as it only requires knowledge of changes in the surface-air specific humidity field in order to explain much of the response of $P - E$ over land. The zonal-mean changes in surface-air land temperature and relative humidity can be understood using relatively simple arguments, as discussed in Chapters 2–4. We showed, however, that it is often the spatial structure of the humidity changes across continents that is important for the zonal-mean $P-E$ response, i.e. the "symmetric" and "asymmetric" warming mechanisms described in Section 5.4.3. Thus, a full theory for projected changes in $P-E$ over land will need to account not only for changes in atmospheric dynamics but also for the regional structure of the surface-air specific humidity changes (though these processes could potentially be linked via thermal wind balance, as mentioned in Chapter 5).

6.2 Outlook

At various points during this thesis, we have suggested paths for future research. Below, we collate these ideas, sketch out some additional ones, and provide a short personal outlook for the field of terrestrial climate change.

The tropical land-ocean warming contrast in simulations is well-described by the CQE theory, but what about the warming contrast at higher latitudes? Neither convective quasi-equilibrium nor the weak temperature gradient approximation are expected to be valid poleward of the tropics in the time-mean. Not surprisingly, our CQE theory is less successful in the extratropics. As discussed in Chapter 2, theories for the extratropical thermal stratification do exist and could potentially be used to develop a theory for the warming contrast, analogous to the CQE theory, that is appropriate at higher latitudes. Using the effective static stability theory of O'Gorman (2011), a modified theory for the extratropical warming contrast can be obtained by multiplying the warming contrast predicted by the CQE theory by a factor of 0.6. This modified theory is found to work well in the idealized GCM (Fig. 2-11b) though it has not yet been tested in more realistic models and this would be an interesting way to extend the work in this thesis. Water vapor-radiation feedbacks (Dommenget and Flöter, 2011) and albedo changes, in addition to stratification effects, may be important for the warming contrast at higher latitudes and the influence of such processes could be investigated with idealized GCM simulations.

We have focussed exclusively on the warming contrast averaged over long time periods, but land-ocean contrasts also exist on interannual timescales (Tyrrell et al., 2014), excited by modes of internal climate variability such as the El Niño-Southern Oscillation (ENSO). The structure of the ENSO forcing is very different to the radiative forcing under global warming, which is more spatially uniform, and heat capacity effects could also become important for the warming contrast on shorter timescales. Thus, it would be interesting to compare the magnitudes and spatial structures of the warming contrasts under global warming and in interannual variability, and to investigate whether the CQE theory is applicable on shorter timescales with non-uniform spatial forcing. Again, this question could be approached initially using idealized GCM simulations, perhaps with a tropical land continent and an imposed equatorial ocean heat flux convergence representing a simplified El Niño, before examining the behavior in CMIP5 simulations and observations.

In our analyses of various land-ocean contrasts (temperature, relative humidity, water cycle), we have mostly restricted ourselves to simple theories and simulations. The results would be even more compelling if our theories for the warming contrast and land relative humidity and $P - E$ changes were found to explain trends in the observational record. For example, can the conceptual box model for land relative humidity changes explain the sharp drop in relative humidity between 2000 and 2008 (Simmons et al., 2010)? Using the extended thermodynamic scaling, can trends in land $P - E$ (calculated from river discharge data or atmospheric moisture fluxes) be reconciled with observed changes in surface humidity patterns? Atmospheric reanalyses have substantial water cycle biases (Trenberth et al., 2011) and so, at the present time, are unsuitable for studying such questions (even for the warming contrast, reliable near-surface relative humidity data are required to evaluate the CQE theory). Due to data coverage and reliability issues, particularly in the tropics, using direct observations to test our theories is also challenging. However, progress could be made by analyzing the existing observations and comparing to historical CMIP5 simulations (as for the warming contrast in Section 3.4) or using a combination of available observations with the more reliable components of atmospheric reanalyses to test our theories, and both techniques should be attempted in future work.

Another potential extension of this thesis would be to investigate the roles of land surface temperature and relative humidity in monsoon circulations. As mentioned briefly in Chapter 2, the upward branches of monsoon circulations are co-located with boundary-layer maxima in either equivalent potential temperature or potential temperature (Emanuel, 1995; Privé and Plumb, 2007; Nie et al., 2010). Consequently, changes in the surface temperature and relative humidity over land are certain to impact the position and dynamics of the various monsoons of the world. A detailed analysis of the monsoon circulations generated in the idealized GCM simulations described in Chapters 2 & 4, and their dependence on land temperature and humidity, could improve our understanding of the role of land surface conditions in controlling monsoons. The insights gained from the idealized simulations could then be used to guide our interpretation of disparate changes in monsoons under climate change in more complex models.

In this thesis we have almost exclusively discussed historical and future global warming, but our theories for land-ocean contrasts are also applicable to paleoclimate questions. For example, could the anomalously arid conditions over North America during the Medieval Warm Period (Cook et al., 2004) be partly explained by variations in temperature and relative humidity gradients, following our extended scaling for $P - E$ changes? Increases in zonal moisture advection contributed to the onset of the East African Humid Period (Tierney et al., 2011); could the extended scaling also help to interpret this abrupt climate shift? These questions could be investigated using lake level, temperature and humidity paleoclimate data from those eras, perhaps in conjunction with Paleoclimate Modelling Intercomparison Project (PMIP) simulations, such as those of the last millennium (known as the *past1000* simulations in the CMIP5 archive). The CQE theory for the land-ocean warming contrast, which relates temperatures and relative humidities over land and ocean in the tropics, could also be a useful tool for paleoclimate research. It could, for instance, be used to reconcile paleotemperature proxies with estimates of tropical snowline heights from the Last Glacial Maximum (e.g., Greene et al., 2002), or to infer estimates of relative humidity in regions where only temperature data are available. Pursuing questions of this nature in paleoclimatology would be a fascinating way of broadening the impact and application of the ideas developed in this thesis.

Numerous questions related to the response of land and the water cycle to climate change remain unresolved. Of particular interest currently, and a topic closely related to our discussions in Chapter 5, is the role of changing surface temperatures versus the direct, radiative effect of increasing CO_2 in controlling dynamical precipitation change (Chadwick et al., 2013; Bony et al., 2013; Chadwick et al., 2014). A consensus on this issue has not yet emerged, though our results highlight the importance of both changing temperature gradients and changing circulations (especially in the tropics) for terrestrial $P-E$ on long timescales. It is not clear from our analysis, however, the extent to which the simulated circulation changes are a direct response to increasing CO_2. Using the atmospheric moisture budget analysis, it would be interesting to compare the mechanisms determining terrestrial $P-E$ changes on long timescales with those operating on shorter timescales immediately following an abrupt CO_2 quadrupling, say [following Bony et al. (2013); Chadwick et al. (2014)]. If the changes on both timescales were found to be similar it would suggest that $P-E$ over land is largely independent of changes in SST, narrowing the focus for improving water cycle projections over land.

More generally, our simple theories have proved successful at describing the large-scale behavior over land under climate change at least in models, but challenges remain in predicting the regional response and the intermodel scatter. Changes in regional land temperature and relative humidity are largely controlled by the changes over ocean, but locally the response also depends on soil moisture and vegetation, which complex models struggle to simulate well. Models also have difficulty reproducing the observed diurnal cycle of convection over land (e.g., Schlemmer et al., 2011), with implications for the simulation of the time-mean terrestrial climate (Cronin et al., 2014). Clearly the representations of surface hydrology, convection and a plethora of other processes in climate models need to be improved to enable more reliable projections of regional climate change. These model improvements will require higher spatial resolution and increased mechanistic understanding, both difficult tasks that will be ongoing for many years. However, as I hope this thesis has demonstrated, research with a combination of simplified and complex models can still be insightful, not by making accurate forecasts of future climate change but by highlighting what processes are and are not important for the climate phenomenon at hand and thus furthering our scientific understanding of the climate system.

Bibliography

Adler, R. F., C. Kidd, G. Petty, M. Morissey, and H. M. Goodman, 2001: Intercomparison of global precipitation products: The third Precipitation Intercomparison Project (PIP-3). *Bull. Amer. Meteor. Soc.*, **82**, 1377–1396.

Alexeev, V. A., P. L. Langen, and J. R. Bates, 2005: Polar amplification of surface warming on an aquaplanet in "ghost forcing" experiments without sea ice feedbacks. *Climate Dyn.*, **24**, 655–666.

Allen, M. R. and W. J. Ingram, 2002: Constraints on future changes in climate and the hydrologic cycle. *Nature*, **419**, 224–232.

Andrews, T., M. Doutriaux-Boucher, O. Boucher, and P. M. Forster, 2011: A regional and global analysis of carbon dioxide physiological forcing and its impact on climate. *Climate Dyn.*, **36**, 783–792.

Arakawa, A. and W. H. Schubert, 1974: Interaction of a cumulus cloud ensemble with the large-scale environment, Part I. *J. Atmos. Sci*, **31**, 674–701.

Bayr, T. and D. Dommenget, 2013: The tropospheric land–sea warming contrast as the driver of tropical sea level pressure changes. *J. Climate*, **26**, 1387–1402.

Bengtsson, L., S. Hagemann, and K. I. Hodges, 2004: Can climate trends be calculated from reanalysis data? *J. Geophys. Res.*, **109 (D11)**.

Boer, G. J., 1993: Climate change and the regulation of the surface moisture and energy budgets. *Climate Dyn.*, **8**, 225–239.

Boer, G. J., 2011: The ratio of land to ocean temperature change under global warming. *Climate Dyn.*, **37**, 2253–2270.

Bolton, D., 1980: The computation of equivalent potential temperature. *Mon. Wea. Rev.*, **108**, 1046–1053.

Bony, S., G. Bellon, D. Klocke, S. Sherwood, S. Fermepin, and S. Denvil, 2013: Robust direct effect of carbon dioxide on tropical circulation and regional precipitation. *Nat. Geosci.*, **6**, 447–451.

Bony, S., et al., 2006: How well do we understand and evaluate climate change feedback processes? *J. Climate*, **19**, 3445–3482.

Boos, W. R., 2012: Thermodynamic scaling of the hydrological cycle of the last glacial maximum. *J. Climate*, **25**, 992–1006.

Brohan, P., J. J. Kennedy, I. Harris, S. F. B. Tett, and P. D. Jones, 2006: Uncertainty estimates in regional and global observed temeprature changes: A new dataset from 1850. *J. Geophys. Res.*, **111 (D12)**.

Byrne, M. P. and P. A. O'Gorman, 2013a: Land-ocean warming contrast over a wide range of climates: Convective quasi-equilibrium theory and idealized simulations. *J. Climate*, **26**, 4000–4016.

Byrne, M. P. and P. A. O'Gorman, 2013b: Link between land-ocean warming contrast and surface relative humidities in simulations with coupled climate models. *Geophys. Res. Lett.*, **40**, 5223–5227.

Cao, L., G. Bala, K. Caldeira, R. Nemani, and G. Ban-Weiss, 2010: Importance of carbon dioxide physiological forcing to future climate change. *Proc. Natl. Acad. Sci.*, **107**, 9513–9518.

Chadwick, R., I. Boutle, and G. Martin, 2013: Spatial patterns of precipitation change in CMIP5: Why the rich do not get richer in the tropics. *J. Climate*, **26**, 3803–3822.

Chadwick, R., P. Good, T. Andrews, and G. Martin, 2014: Surface warming patterns drive tropical rainfall pattern responses to CO_2 forcing on all timescales. *Geophys. Res. Lett.*, **41**, 610–615.

Chou, C. and J. D. Neelin, 2004: Mechanisms of global warming impacts on regional tropical precipitation. *J. Climate*, **17**, 2688–2701.

Compo, G. P. and P. D. Sardeshmukh, 2008: Oceanic influences on recent continental warming. *Climate Dyn.*, **32**, 333–342.

Compo, G. P., et al., 2011: The twentieth century reanalysis project. *Q. J. R. Meteorol. Soc.*, **137**, 1–28.

Cook, E. R., C. A. Woodhouse, C. M. Eakin, D. M. Meko, and D. W. Stahle, 2004: Long-term aridity changes in the western United States. *Science*, **306**, 1015–1018.

Cowtan, K. and R. G. Way, 2014: Coverage bias in the HadCRUT4 temperature series and its impact on recent temperature trends. *Q. J. R. Meteorol. Soc.*, doi: 10.1002/qj.2297.

Cronin, T. W., 2013: A sensitivity theory for the equilibrium boundary layer over land. *J. Adv. Model. Earth Syst.*, **5**, 764–784.

Cronin, T. W., K. A. Emanuel, and P. Molnar, 2014: Island precipitation enhancement and the diurnal cycle in radiative-convective equilibrium. *Q. J. R. Meteorol. Soc.*, doi:10.1002/qj.2443.

Dai, A., 2006: Recent climatology, variability, and trends in global surface humidity. *J. Climate*, **19**, 3589–3606.

Dai, A., T. Qian, K. E. Trenberth, and J. D. Milliman, 2009: Changes in continental freshwater discharge from 1948 to 2004. *J. Climate*, **22**, 2773–2792.

Dessler, A. E. and S. M. Davis, 2010: Trends in tropospheric humidity from reanalysis systems. *J. Geophys. Res.*, **115 (D19)**.

Dommenget, D., 2009: The ocean's role in continental climate variability and change. *J. Climate*, **22**, 4939–4952.

Dommenget, D. and J. Flöter, 2011: Conceptual understanding of climate change with a globally resolved energy balance model. *Climate Dyn.*, **37**, 2143–2165.

Dong, B., J. M. Gregory, and R. T. Sutton, 2009: Understanding land-sea warming contrast in response to increasing greenhouse gases. Part I: Transient adjustment. *J. Climate*, **22**, 3079–3097.

Doutriaux-Boucher, M., M. J. Webb, J. M. Gregory, and O. Boucher, 2009: Carbon dioxide induced stomatal closure increases radiative forcing via a rapid reduction in low cloud. *Geophys. Res. Lett.*, **36**, L02703.

Drijfhout, S., G. J. Van Oldenborgh, and A. Cimatoribus, 2012: Is a decline of AMOC causing the warming hole above the North Atlantic in observed and modeled warming patterns? *J. Climate*, **25**, 8373–8379.

Drost, F., D. Karoly, and K. Braganza, 2012: Communicating global climate change using simple indices: An update. *Climate Dyn.*, **39**, 989–999.

Durack, P. J., S. E. Wijffels, and R. J. Matear, 2012: Ocean salinities reveal strong global water cycle intensification during 1950 to 2000. *Science*, **336**, 455–458.

Emanuel, K. A., 1995: On thermally direct circulations in moist atmospheres. *J. Atmos. Sci.*, **52**, 1529–1536.

Emanuel, K. A., 2007: Quasi-equilibrium dynamics of the tropical atmosphere. *The Global Circulation of the Atmosphere*, T. Schneider and A. H. Sobel, Eds., Princeton Univ. Press, 186–218.

Fasullo, J. T., 2010: Robust land-ocean contrasts in energy and water cycle feedbacks. *J. Climate*, **23**, 4677–4693.

Field, C. B., V. Barros, D. J. Dokken, et al., 2014: Climate change 2014: Impacts, Adaptation, and Vulnerability. Volume I: Global and sectoral aspects. Contribution of working group II to the fifth assessment report of the Intergovernmental Panel on Climate Change. Cambridge University Press.

Fischer, E. M. and R. Knutti, 2013: Robust projections of combined humidity and temperature extremes. *Nat. Climate Change*, **3**, 126–130.

Frierson, D. M. W., 2007: The dynamics of idealized convection schemes and their effect on the zonally averaged tropical circulation. *J. Atmos. Sci.*, **64**, 1959–1976.

Frierson, D. M. W., 2008: Midlatitude static stability in simple and comprehensive general circulation models. *J. Atmos. Sci.*, **65**, 1049–1062.

Frierson, D. M. W. and N. A. Davis, 2011: The seasonal cycle of midlatitude static stability over land and ocean in global reanalyses. *Geophys. Res. Lett.*, **38**, L13803.

Frierson, D. M. W., I. M. Held, and P. Zurita-Gotor, 2006: A gray-radiation aquaplanet moist GCM. Part I: Static stability and eddy scale. *J. Atmos. Sci.*, **63**, 2548–2566.

Frierson, D. M. W. and Y.-T. Hwang, 2012: Extratropical influence on ITCZ shifts in slab ocean simulations of global warming. *J. Climate*, **25**, 720–733.

Fu, Q. and S. Feng, 2014: Responses of terrestrial aridity to global warming. *J. Geophys. Res.*, doi:10.1002/2014JD021608.

Greene, A. M., R. Seager, and W. S. Broecker, 2002: Tropical snowline depression at the last glacial maximum: Comparison with proxy records using a single-cell tropical climate model. *J. Geophys. Res.*, **107 (D8)**.

Greve, P., B. Orlowsky, B. Mueller, J. Sheffield, M. Reichstein, and S. I. Seneviratne, 2014: Global assessment of trends in wetting and drying over land. *Nat. Geosci.*, doi:10.1038/ngeo2247.

Hall, A., 2004: The role of surface albedo feedback in climate. *J. Climate*, **17**, 1550–1568.

Hansen, J., R. Ruedy, M. Sato, and K. Lo, 2010: Global surface temperature change. *Rev. Geophys.*, **48**.

Hartmann, D. L., 1994: *Global Physical Climatology.* Academic Press, 411 pp.

Hawkins, E. and R. Sutton, 2011: The potential to narrow uncertainty in projections of regional precipitation change. *Climate Dyn.*, **37**, 407–418.

Held, I. M., 2014: Relative humidity over the oceans. Isaac Held's Blog, available at http://www.gfdl.noaa.gov/blog/isaac-held/2014/06/26/47-relative-humidity-over-the-oceans/.

Held, I. M. and B. J. Soden, 2000: Water vapor feedback and global warming. *Annu. Rev. Energy Environ.*, **25**, 441–475.

Held, I. M. and B. J. Soden, 2006: Robust responses of the hydrological cycle to global warming. *J. Climate*, **19**, 5686–5699.

Holland, M. M. and C. M. Bitz, 2003: Polar amplification of climate change in coupled models. *Climate Dyn.*, **21**, 221–232.

Holton, J. R., 2004: *An Introduction to Dynamic Meteorology.* 4th ed., Elsevier Academic Press, 535 pp.

Huntingford, C. and P. M. Cox, 2000: An analogue model to derive additional climate change scenarios from existing GCM simulations. *Climate Dyn.*, **16**, 575–586.

Hwang, Y.-T., D. M. W. Frierson, and S. M. Kang, 2013: Anthropogenic sulfate aerosol and the southward shift of tropical precipitation in the late 20th century. *Geophys. Res. Lett.*, **40**, 2845–2850.

Izumi, K., P. J. Bartlein, and S. P. Harrison, 2014: Energy-balance mechanisms underlying consistent large-scale temperature responses in warm and cold climates. *Climate Dyn.*, doi:10.1007/s00382-014-2189-2.

Joshi, M. M. and J. M. Gregory, 2008: Dependence of the land-sea contrast in surface climate response on the nature of the forcing. *Geophys. Res. Lett.*, **35**, L24802.

Joshi, M. M., J. M. Gregory, M. J. Webb, D. M. H. Sexton, and T. C. Johns, 2008: Mechanisms for the land/sea warming contrast exhibited by simulations of climate change. *Climate Dyn.*, **30**, 455–465.

Joshi, M. M., F. H. Lambert, and M. J. Webb, 2013: An explanation for the difference between twentieth and twenty-first century land-sea warming ratio in climate models. *Climate Dyn.*, **41**, 1853–1869.

Juckes, M. N., 2000: The static stability of the midlatitude troposphere: The relevance of moisture. *J. Atmos. Sci.*, **57**, 3050–3057.

Jung, M., et al., 2010: Recent decline in the global land evapotranspiration trend due to limited moisture supply. *Nature*, **467**, 951–954.

Kalma, J. D., T. R. McVicar, and M. F. McCabe, 2008: Estimating land surface evaporation: A review of methods using remotely sensed surface temperature data. *Surv. Geophys.*, **29**, 421–469.

Knutti, R. and J. Sedláček, 2013: Robustness and uncertainties in the new CMIP5 climate model projections. *Nat. Climate Change*, **3**, 369–373.

Laîné, A., H. Nakamura, K. Nishii, and T. Miyasaka, 2014: A diagnostic study of future evaporation changes projected in cmip5 climate models. *Climate Dyn*, **42**, 2745–2761.

Lambert, F. H. and J. C. H. Chiang, 2007: Control of land-ocean temperature contrast by ocean heat uptake. *Geophys. Res. Lett.*, **34**, L13704.

Lambert, F. H., M. J. Webb, and M. M. Joshi, 2011: The relationship between land-ocean surface temperature contrast and radiative forcing. *J. Climate*, **24**, 3239–3256.

Lu, J., G. A. Vecchi, and T. Reichler, 2007: Expansion of the Hadley cell under global warming. *Geophys. Res. Lett.*, **34 (6)**.

Manabe, S., 1969: Climate and the ocean circulation. *Mon. Wea. Rev.*, **97**, 739–774.

Manabe, S., R. J. Stouffer, M. J. Spelman, and K. Bryan, 1991: Transient responses of a coupled ocean-atmosphere model to gradual changes of atmospheric CO_2. Part I: Annual mean response. *J. Climate*, **4**, 785–818.

Meehl, G. A., C. Covey, T. Delworth, M. Latif, B. McAvaney, J. F. B. Mitchell, R. J. Stouffer, and K. E. Taylor, 2007: The WCRP CMIP3 multi-model dataset: A new era in climate change research. *Bull. Amer. Meteor. Soc.*, **88**, 1383–1394.

Merlis, T. M. and T. Schneider, 2010: Atmospheric dynamics of earth-like tidally locked aquaplanets. *J. Adv. Model. Earth Syst.*, **2 (4)**.

Mitchell, J. F. B., C. A. Wilson, and W. M. Cunnington, 1987: On CO_2 climate sensitivity and model dependence of results. *Q. J. R. Meteorol. Soc.*, **113**, 293–322.

Molnar, P. and K. A. Emanuel, 1999: Temperature profiles in radiative-convective equilibrium above surfaces at different heights. *J. Geophys. Res.*, **104**, 24 265–24 271.

Nie, J., W. Boos, and Z. Kuang, 2010: Observational evaluation of a convective quasi-equilibrium view of monsoons. *J. Climate*, **23**, 4416–4428.

O'Gorman, P. A., 2011: The effective static stability experienced by eddies in a moist atmosphere. *J. Atmos. Sci.*, **68**, 75–90.

O'Gorman, P. A., R. P. Allan, M. P. Byrne, and M. Previdi, 2012: Energetic constraints on precipitation under climate change. *Surv. Geophys.*, **33**, 585–608.

O'Gorman, P. A. and C. J. Muller, 2010: How closely do changes in surface and column water vapor follow Clausius-Clapeyron scaling in climate-change simulations? *Environ. Res. Lett.*, **5 (2)**, 025207.

O'Gorman, P. A. and T. Schneider, 2006: Stochastic models for the kinematics of moisture transport and condensation in homogeneous turbulent flows. *J. Atmos. Sci.*, **63**, 2992–3005.

O'Gorman, P. A. and T. Schneider, 2008a: Energy of midlatitude transient eddies in idealized simulations of changed climates. *J. Climate*, **21**, 3815–3832.

O'Gorman, P. A. and T. Schneider, 2008b: The hydrological cycle over a wide range of climates simulated with an idealized GCM. *J. Climate*, **21**, 5797–5806.

Peixóto, J. P. and A. H. Oort, 1984: Physics of Climate. *Reviews of Modern Physics*, **56**.

Pierrehumbert, R. T., 1995: Thermostats, radiator fins, and the local runaway greenhouse. *J. Atmos. Sci.*, **52**, 1784–1806.

Privé, N. C. and R. A. Plumb, 2007: Monsoon dynamics with interactive forcing. Part I: Axisymmetric studies. *J. Atmos. Sci.*, **64**, 1417–1430.

Roderick, M. L., F. Sun, W. H. Lim, and G. D. Farquhar, 2014: A general framework for understanding the response of the water cycle to global warming over land and ocean. *Hydr. Earth Syst. Sci.*, **18**, 1575–1589.

Rohde, R., et al., 2013: A new estimate of the average earth surface land temperature spanning 1753 to 2011. *Geoinform. Geostat: An Overview*, doi: 10.4172/gigs.1000101.

Rowell, D. P. and R. G. Jones, 2006: Causes and uncertainty of future summer drying over Europe. *Climate Dyn.*, **27**, 281–299.

Santer, B. D., et al., 2005: Amplification of surface temperature trends and variability in the tropical atmosphere. *Science*, **309**, 1551–1556.

Scheff, J. and D. Frierson, 2012: Twenty-first-century multimodel subtropical precipitation declines are mostly midlatitude shifts. *J. Climate*, **25**, 4330–4347.

Scheff, J. and D. M. W. Frierson, 2014: Scaling potential evapotranspiration with greenhouse warming. *J. Climate*, **27**, 1539–1558.

Schlemmer, L., C. Hohenegger, J. Schmidli, C. S. Bretherton, and C. Schär, 2011: An idealized cloud-resolving framework for the study of midlatitude diurnal convection over land. *J. Atmos. Sci.*, **68**, 1041–1057.

Schneider, T. and P. A. O'Gorman, 2008: Moist convection and the thermal stratification of the extratropical troposphere. *J. Atmos. Sci.*, **65**, 3571–3583.

Schneider, T., P. A. O'Gorman, and X. J. Levine, 2010: Water vapor and the dynamics of climate changes. *Rev. Geophys.*, **48**, RG3001.

Seager, R., H. Liu, N. Henderson, I. Simpson, C. Kelley, T. Shaw, Y. Kushnir, and M. Ting, 2014a: Causes of increasing aridification of the mediterranean region in response to rising greenhouse gases. *J. Climate*, **27**, 4655–4676.

Seager, R., N. Naik, and G. A. Vecchi, 2010: Thermodynamic and dynamic mechanisms for large-scale changes in the hydrological cycle in response to global warming. *J. Climate*, **23**, 4651–4668.

Seager, R. and G. A. Vecchi, 2010: Greenhouse warming and the 21st century hydroclimate of southwestern North America. *Proc. Natl. Acad. Sci.*, **107**, 21 277–21 282.

Seager, R., et al., 2014b: Dynamical and thermodynamical causes of large-scale changes in the hydrological cycle over North America in response to global warming. *J. Climate*, doi:10.1175/JCLI-D-14-00153.1.

Seneviratne, S. I., T. Corti, E. L. Davin, M. Hirschi, E. B. Jaeger, I. Lehner, B. Orlowsky, and A. J. Teuling, 2010: Investigating soil moisture-climate interactions in a changing climate: A review. *Earth-Sci. Rev.*, **99**, 125–161.

Sherwood, S. C. and Q. Fu, 2014: A drier future? *Science*, **343**, 737–739.

Sherwood, S. C. and M. Huber, 2010: An adaptability limit to climate change due to heat stress. *Proc. Natl. Acad. Sci.*, **107**, 9552–9555.

Sherwood, S. C., W. Ingram, Y. Tsushima, M. Satoh, M. Roberts, P. L. Vidale, and P. A. O'Gorman, 2010: Relative humidity changes in a warmer climate. *J. Geophys. Res.*, **115 (D9)**.

Simmons, A. J., K. M. Willett, P. D. Jones, P. W. Thorne, and D. P. Dee, 2010: Low-frequency variations in surface atmospheric humidity, temperature, and precipitation: Inferences from reanalyses and monthly gridded observational data sets. *J. Geophys. Res.*, **115 (D1)**.

Smith, T. M., R. W. Reynolds, T. C. Peterson, and J. Lawrimore, 2008: Improvements to NOAA's historical merged land-ocean surface temperature analysis (1880-2006). *J. Climate*, **21**, 2283–2296.

Sobel, A. H. and C. S. Bretherton, 2000: Modeling tropical precipitation in a single column. *J. Climate*, **13**, 4378–4392.

Stevens, B. and S. Bony, 2013: What are climate models missing? *Science*, **340**, 1053–1054.

Stocker, T. F., et al., 2013: Climate change 2013: The physical science basis. Contribution of working group I to the fifth assessment report of the Intergovernmental Panel on Climate Change. Cambridge University Press.

Sutton, R. T., B. Dong, and J. M. Gregory, 2007: Land/sea warming ratio in response to climate change: IPCC AR4 model results and comparison with observations. *Geophys. Res. Lett.*, **34**, L02701.

Takahashi, K., 2009: Radiative constraints on the hydrological cycle in an idealized radiative-convective equilibrium model. *J. Atmos. Sci.*, **66**, 77–91.

Taylor, K. E., R. J. Stouffer, and G. A. Meehl, 2012: An overview of CMIP5 and the experiment design. *Bull. Amer. Meteor. Soc.*, **93**, 485–498.

Tierney, J. E., S. C. Lewis, B. I. Cook, A. N. LeGrande, and G. A. Schmidt, 2011: Model, proxy and isotopic perspectives on the East African Humid Period. *Earth Planet. Sci. Lett.*, **307**, 103–112.

Trenberth, K. E., J. T. Fasullo, and J. Mackaro, 2011: Atmospheric moisture transports from ocean to land and global energy flows in reanalyses. *J. Climate*, **24 (18)**, 4907–4924.

Troen, I. B. and L. Mahrt, 1986: A simple model of the atmospheric boundary layer; sensitivity to surface evaporation. *Bound.-Layer Meteor.*, **37**, 129–148.

Tsonis, A. A., 2002: *An introduction to atmospheric thermodynamics.* Cambridge University Press.

Tyrrell, N. L., D. Dommenget, C. Frauen, S. Wales, and M. Rezny, 2014: The influence of global sea surface temperature variability on the large-scale land surface temperature. *Climate Dyn.*, doi:10.1007/s00382-014-2332-0.

Vecchi, G. A. and B. J. Soden, 2007: Global warming and the weakening of the tropical circulation. *J. Climate*, **20**, 4316–4340.

Willett, K. W., P. D. Jones, N. P. Gillett, and P. W. Thorne, 2008: Recent changes in surface humidity: Development of the HadCRUH dataset. *J. Climate*, **21**, 5364–5383.

Wu, Y., M. Ting, R. Seager, H.-P. Huang, and M. A. Cane, 2011: Changes in storm tracks and energy transports in a warmer climate simulated by the GFDL CM2.1 model. *Climate Dyn.*, **37**, 53–72.

Yin, J. H., 2005: A consistent poleward shift of the storm tracks in simulations of 21st century climate. *Geophys. Res. Lett.*, **32 (18)**.